ABSTRACT

Title of Dissertation: **NOVEL TECHNOLOGIES AND APPLICATIONS FOR FLUORESCENT LAMINAR OPTICAL TOMOGRAPHY**

Qinggong Tang, Doctor of Philosophy, 2017

Dissertation Directed By: Associate Professor, Yu Chen,
Fischell Department of Bioengineering

Laminar optical tomography (LOT) is a mesoscopic three-dimensional (3D) optical imaging technique that can achieve both a resolution of 100-200 μm and a penetration depth of 2-3 mm based either on absorption or fluorescence contrast. Fluorescence laminar optical tomography (FLOT) can also provide large field-of-view (FOV) and high acquisition speed. All of these advantages make FLOT suitable for 3D depth-resolved imaging in tissue engineering, neuroscience, and oncology. In this study, by incorporating the high-dynamic-range (HDR) method widely used in digital cameras, we presented the HDR-FLOT. HDR-FLOT can moderate the limited dynamic range of the charge-coupled device-based system in FLOT and thus increase penetration depth and improve the ability to image fluorescent samples with a large concentration difference. For functional mapping of brain activities, we applied FLOT to record 3D neural activities evoked in the whisker system of mice by deflection of a single whisker *in vivo*. We utilized FLOT to investigate the cell viability, migration, and

bone mineralization within bone tissue engineering scaffolds in situ, which allows depth-resolved molecular characterization of engineered tissues in 3D. Moreover, we investigated the feasibility of the multi-modal optical imaging approach including high-resolution optical coherence tomography (OCT) and high-sensitivity FLOT for structural and molecular imaging of colon tumors, which has demonstrated more accurate diagnosis with 88.23% (82.35%) for sensitivity (specificity) compared to either modality alone. We further applied the multi-modal imaging system to monitor the drug distribution and therapeutic effects during and after Photo-immunotherapy (PIT) in situ and *in vivo*, which is a novel low-side-effect targeted cancer therapy. A minimally-invasive two-channel fluorescence fiber bundle imaging system and a two-photon microscopy system combined with a micro-prism were also developed to verify the results.

NOVEL TECHNOLOGIES AND APPLICATIONS FOR FLUORESCENT LAMINAR OPTICAL TOMOGRAPHY

by

Qinggong Tang

Dissertation submitted to the Faculty of the Graduate School of the
University of Maryland, College Park, in partial fulfillment
of the requirements for the degree of
Doctor of Philosophy
2017

Advisory Committee:
Associate Professor Yu Chen, Chair
Assistant Professor Giuliano Scarcelli
Associate Professor Ian White
Professor John Fisher
Professor Thomas E. Murphy, Dean's Representative

Acknowledgements

I would first and foremost like to express my deepest gratitude to Dr. Yu Chen for his guidance and patience during my five-year study. Thank you for steadily guiding me through so many research projects and helping me develop professionally. During my time in UMD, Dr. Chen has not only taught me how to solve problems scientifically, but also has given me a logical mind to bring up questions. Thanks for providing so many outstanding resources, through which I have gained lots of experience in managing time and communicating with collaborators. Dr. Chen is very nice and always ready to respond to your questions. Whenever I am confused or frustrated with my research, he is always there to help and encourage me. He also cares about students' future development. He always supports me in attending academic conferences and all the occasions that I have had chances to know more people and learn more about the cutting-edge researchs. I believe his persistence and dedication in achieving the highest level of excellence will always inspire me in my future career.

I also would like to thank all the outstanding collaborators in my research. I would like to thank Dr. John Fisher from the Fischell Department of Bioengineering and Dr. John Caccamese from University of Maryland School of Dentistry. When I just started the tissue engineering project, I had very little experience. Drs. John Fisher and John Caccamese gave me a lot of encouragement, and explained the background to me with patience. Thanks to Mrs. Charlotte Piard for providing all the tissue engineering samples and all the helpful discussions. I would like to thank Dr. Reha S. Erzurumlu and Dr. Vassiliy Tsytsarev from University of Maryland School

of Medicine. Dr. Reha is a very wise and nice professor. He helped me go over my research slides page by page and explained all the biological backgrounds with great patience. I worked with Dr. Vassiliy for more than four years almost from the first month I came to USA. He always has a lot of novel ideas to share and introduced me to many other great researchers in all research areas. I would also like to thank Dr. Hisataka Kobayashi and Dr. Tadanobu Nagaya from National Cancer Institute. Thanks for providing the excellent Photoimmunotherapy (PIT) and animal models for testing our imaging devices *in vivo*. Thanks for the active discussions and insightful suggestions which keep the research in the direction of progress.

I would like to acknowledge my great lab-mates, Drs. Hengchang Guo, Jianting Wang, Hsing-wen Wang, Chao-Wei Chen, Udayakumar Kanniyappan, Hyounguk Jang, Zhengyang Ding, Hui Li, Zhifang Li and Chia-pin Liang, for their companionship and mentorship. The lunchtime chats with all of you are unforgettable memories. Thanks all for sharing your experiences and all the brain storms. Thanks Hengchang for teaching me the TPM imaging system and the animal experience. Thanks Jianting for starting the work of colon cancer and your hospitality. Thanks Hsing-wen for guidance on the laparoscope project, which is my first research project in UMD. Thanks Chao-wei for paving the way for aFLOT, all the trainings and for the preliminary works on tissue engineering and functional brain imaging. Thanks Uday for the help on the breast cancer project. Thanks Hyounguk for characterizing the aFLOT system and the helpful discussion. Thanks Zhenyang for showing me how to be an efficient researcher and the knowledge on Polarization-sensitive Optical Coherence Tomography (PS-OCT). Thanks Hui for teaching me how to think about

questions in a comprehensive way. Thanks Zhifang and Lily Jin for the help on the colon cancer project and helpful discussions. Special thanks to Chia-pin Liang, in the 2-year overlap, you guided me on the OCT needle project step by step and taught me how to talk to collaborators. I cannot forget all the late nights and weekends we worked together and also of course all the happy time we spent in the gym playing badminton and racquetball. You are like a big brother to me and guide me in both my research and life. Thanks Mr. Bohan Wang for the fancy ideas and Yi Liu for helping on the HDR-FLOT project. Also thanks to the undergraduates in the lab for their efforts and help. I would like to acknowledge Mr. Yalun Wu, Aaron Frank, Jonathan Lin, Kai Nan, Hannah Horng and Rao Zhang for your time and hard works.

Finally, many thanks to my family and girlfriend, your unconditional support and love always motivate me to move forward and pursue my dreams. Without you, I would not be so faithful and none of this would have been possible.

Table of Contents

List of Figures

Chapter 7

Chapter 8

Chapter 1: Introduction*

1.1 Motivation

1.1.1 Brain functional imaging

Neurons are the most essential units in the nervous system. In order to understand how the brain perceives the external world, it is necessary to observe neuronal functions in the brain during perception [1]. Localization of neural activities, in other words, functional brain mapping, is one of the fundamental tasks for many generations of neuroscientists within the last hundred years [2]. Furthermore, mapping the activity patterns of the neural circuits can reveal cellular and molecular mechanisms of the wiring of the brain and further help us learn more about brain disease processes and the effects of treatments [3].

Optical methods have been very useful in monitoring neural responses in brain, since they can offer several advantages [4]. Various optical imaging methods based on either reflectance, absorption or fluorescence have been demonstrated in functional brain mapping [5]. Intrinsic Optical Signal (IOS) imaging[6, 7], Diffuse Optical Imaging

* Part of the contents in this chapter is modified and reproduced from "Tang, Q. et al. Mesoscopic Fluorescence Tomography for Imaging Bone Engineered Tissues. *Under review*.", "Tang, Q. et al., Real-time monitoring of microdistribution of antibody-photon absorber conjugates during photoimmunotherapy in vivo, *Journal of Controlled Release*, 260(154-163), 28 August 2017." and "Tang, Q. et al. Depth-resolved imaging of colon tumor using optical coherence tomography and fluorescence laminar optical tomography. Biomed. *Opt. Express* **7**, 5218-5232 (2016) " with permission.

(DOI) [8-10], Optical Coherence Tomography (OCT) [11-15], Photoacoustic Tomography (PAT) [16], as well as Multiphoton Microscopy (MPM) [17, 18], provide tools for neuroscientists to observe the anatomy of the living brain noninvasively, and to monitor brain functions *in vivo*. However, limited resolution (DOI), relatively low contrast (OCT), shallow penetration depth (IOS), or low data acquisition speed (MPM and PAT) have limited their applications in imaging 3D neural activities to some extent, since it needs both high temporal and spatial resolutions to visualize the neural response [19,20]. The major challenge for optical imaging is to overcome the effects of light scattering, which limits both the penetration depth and imaging resolution we can achieve [21].

1.1.2 Bone tissue engineering

Each year, there are nearly 15 million bone fractures [22] and 1 million bone grafting procedures worldwide [23]. There is a significant clinical need for engineered bone graft substitutes that can quickly, effectively, and safely repair large segmental bone defects [23]. Bone tissue engineering scaffolds serve as vehicles for the delivery of progenitor cell populations or support structures for surrounding tissue ingrowth. Scaffold properties often determine the success in an engineered tissue and must be designed for a specific application. In many outcomes, key parameters allow for improved cell migration, proliferation and vascularization. To improve tissue regeneration and integration, a scaffold should mimic surrounding tissue morphology, structure, and function. This environment should promote cellular interactions and signaling, and as a result, differentiation.

One challenge in bone tissue engineering is to comprehensively observe and quantify the distribution and migration of seeded cells throughout the bulky scaffold. Bone tissue engineering could benefit from a precise and noninvasive imaging method to follow cell activity. Such an imaging technology could provide useful information on the interplay of scaffold designs, cells, and chemical/environmental cues to optimize the development of bone grafts. Optical imaging is a promising approach to non-destructively quantify both scaffold architecture and cell distribution at high resolution. Fluorescence confocal microscopy (FCM) can visualize cells and molecules via a wide variety of fluorescence probes and is a powerful technique for molecular imaging. However, FCM has a limited imaging depth of ~100 μm [24]. In addition, two-photon microscopy (TPM) has been used to image engineered tissues[24], but is also associated with a limited penetration depth of ~500 μm [25, 26]. The current state-of-the-art method for quantifying 3D cell distribution involves FCM imaging of cryo-sectioned scaffolds and digital 3D image recompiling. Although robust, this approach is destructive and time-consuming, and may become a concern in longitudinal inspection of massive amount of samples.

1.1.3 Tumor detection and therapy monitoring

Early detection of neoplastic changes remains a critical challenge in clinical cancer diagnosis and treatment. Many cancers arise from epithelial layers such as those of the gastrointestinal (GI) tract. White-light endoscopy guided excisional biopsy and histopathology is currently the gold standard for GI cancer diagnosis. However, it suffers from high false negative rates due to sampling errors [27-30]. Furthermore, a significant portion of patients after endoscopic ablative therapeutic

treatment showed the presence of metaplasia or dysplasia buried underneath the neo-epithelium [31-35], which is associated with the risk of cancer development [30, 36-39]. Current standard endoscopic technology is unable to detect those subsurface lesions. Therefore, there is a critical need for developing new diagnostic tools which can assess tissue architectural and molecular information across the mucosal depth for improved detection of subsurface cancer, and evaluate the invasion depth of a lesion [40].

The efficacy of cancer therapy depends on its ability to deliver drugs to tumors [41]. Real-time monitoring of theranostic agent distribution and its therapeutic effects, including cellular necrosis within the tumor microenvironment, will be critical for further understanding the drug mechanism and optimizing the effectiveness of treatment. The current approach for monitoring drug fluorescence is macroscopic fluorescence reflectance imaging, which lacks the resolution and depth information to show the distribution of molecules *in situ* [42]. Histological analysis reveals intratumor drug distribution is inhomogeneous. However, it is invasive and terminal. Real-time change of the microdistribution of drug molecules in different locations within the tumor after treatment has not been studied *in vivo*.

1.2 Background

Optical imaging technologies promise to provide real-time, high-resolution imaging of tissue morphology and function *in vivo* with resolution at or near that of histopathology, therefore, it has been significantly utilized in biomedical researches and application. In this section several mesoscopic imaging techniques will be introduced.

1.2.1 Optical coherence tomography (OCT)

Optical coherence tomography (OCT) is an established biomedical imaging technology for subsurface imaging of tissues with high resolution (<10 μm) and 1-2 mm penetration depth [43-46], which is comparable to the size of standard pinch biopsy and histology. OCT can generate high-resolution, cross-sectional images of tissue morphology *in situ* and in real time. OCT is an optical analog of ultrasound except that it utilizes near infrared light rather than sound [47-51]. Since OCT does not utilize ionizing radiation, and no special preparation of the patient is required prior to obtaining the imaging, it is gaining traction within the medical community. OCT can be mainly classified into two types: time domain OCT (TD-OCT) and Fourier-domain OCT (FD-OCT), and the latter type can offer better sensitivity and faster imaging speed [52-54]. Besides the differences in tissue scattering properties, OCT can also utilize other contrast mechanisms and provide supplementary information in addition to intensity variation. There are three main OCT extensions for functional imaging: Doppler OCT [55-57], speckle variance OCT [58 59 60], and polarization-sensitive OCT (PS-OCT) [61 62 63] .

OCT can be interfaced with fiber-optic catheters and endoscopes to image inside the body [45, 64-66]. Endoscopic OCT has been demonstrated in the human gastrointestinal (GI) tract [67-70] to detect Barrett's esophagus (BE) [71, 72] and dysplasia [73, 74]. OCT's high depth-resolution and appropriate penetration depth make it an attractive technology for detecting subsurface abnormalities in the mucosal and submucosal layers. Visualization of cross-sectional mucosal and submucosal features is a key advantage of OCT imaging when compared to standard endoscopy.

1.2.2 High-speed CCD camera based VSDi

Voltage-sensitive dye imaging (VSDi) has been quite useful in imaging activities of the neural networks in the brain [5]. VSDi is based on fluorophore molecules that bind to the neural membrane and convert changes in transmembrane voltage into the fluorescence of the emitted light [5]. VSDi creates an opportunity to monitor neural

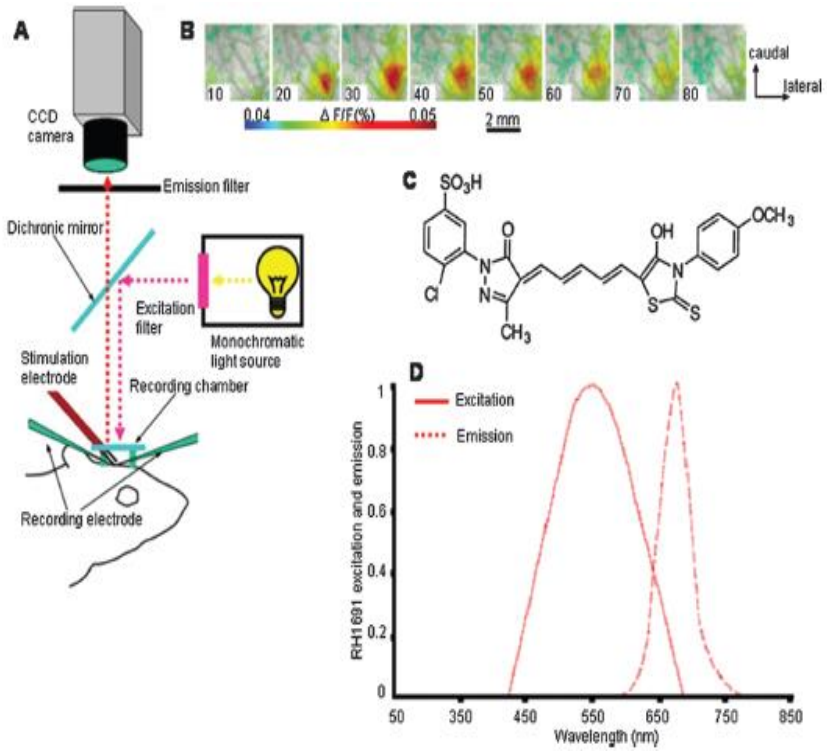

Figure 1. Voltage-sensitive dye optical imaging setup

(A) Main parts of the voltage-sensitive dye optical imaging setup. (B) Voltage-sensitive dye optical images of the somatosensory cortex showing single-whisker stimulation fluorescence changes, the time after stimulus onset (ms) is indicated at the bottom left corner of each image.(C) RH1691, one of the most common voltage-sensitive dye molecule. (D) Excitation and emission spectrum of the RH1691 voltage-sensitive dye [75, 76].

activity *in vivo* with relatively high spatial and temporal resolution (up to microseconds) (Fig. 1). VSDs are based on chemical compounds that change their optical properties in response to a change in membrane's electric field intensity [77] . Dye molecules can bind to the neuron membrane, the changes in membrane potential

can be converted into the energy of the emitted photons. Measuring the changes in the fluorescence of the dye can then infer the changes in membrane potential [78]. VSD signals can reflect both spiking and synaptic activities since much of the total membrane area is dendritic [79]. For a commercial VSDi system, the sample is illuminated by excitation light through appropriate optical filters based on the VSD used, and the fluorescent signal is recorded by a high-speed CCD camera through a dichroic mirror and appropriate optical filters as shown in Fig. 2(A). The temporal resolution of the system is mainly determined by parameters of the CCD camera [3] and the spatial resolution is determined by both the CCD camera and the field of view (FOV) imaged. However, since CCD cameras integrate the fluorescence signals from different depths, like other the wide field optical imaging techniques, the current VSDi setup cannot allow visualization of neural activities in three dimensions [80].

1.2.3 Light Sheet Fluorescence Microscopy

Light sheet fluorescence microscopy (LSFM) can function as a non-destructive microtome and microscope. LSFM uses a thin plane of light to optically section transparent tissues or whole organisms that have been labeled with a fluorophore with subcellular resolution and penetration depth over 1 cm [81]. LSFM is well suited for imaging transparent tissues or within whole organisms, and has huge impact in fields of developmental and cell biology, anatomical science, biophysics and neuroscience [82]. One obvious advantage is that the photo-bleaching and photo-toxicity of specimen are minimized compared to wide-field fluorescence, confocal, or multiphoton microscopy since tissues are exposed to only a thin plane of light [81].

Moreover, LSFM produces well-registered optical sections that can be easily reconstructed in three-dimensions and the samples can be processed by other histological methods (e.g., mechanical sectioning) after imaging [81, 83]. Furthermore, it costs much less to construct an LSFM system compared to these other microscopes.

1.2.4 Two-Photon Microscope (TPM)

Two-photon excitation microscopy, first demonstrated by Denk *et al.*[84], is a fluorescence imaging technique that allows imaging of living tissue up to about one millimeter depth with a high resolution of less than 1μm. Being a special variant of the multiphoton fluorescence microscope, it uses a red-shifted excitation light which can also excite fluorescent dyes. However for each excitation, two photons of the infrared light are absorbed. Due to the multiphoton absorption, the background signal is strongly suppressed. In addition, using infrared light can minimize scattering in the tissue. Both effects lead to an increased penetration depth for these microscopes. Two-photon excitation can be a superior alternative to confocal microscopy due to its deeper tissue penetration, efficient light detection and reduced phototoxicity [84-88].

1.2.6 Fluorescence laminar optical tomography (FLOT)

Laminar optical tomography (LOT) is a promising optical imaging method that collects scattered light travelling through different depths by using multiple detectors, and reconstructs the depth-resolved images through mathematical deconvolution [89]. LOT can achieve a resolution of 100-200 μm with 2-3 mm penetration depths [80, 90-94]. It was initially utilized to image hemodynamic changes based on absorption contrast [91, 95, 96]. Soon after, LOT was rapidly adapted for fluorescent molecular imaging,

which was termed either fluorescence laminar optical tomography (FLOT) [80, 92-94] or mesoscopic fluorescence molecular tomography (MFMT) [97, 98], and several improvements and alternative system designs have been investigated [80, 92, 97-101]. FLOT has been reported to quantify depth-resolved distribution of fluorescence-labeled tumors[100, 102, 103], to image fluorescence-labeled cells in tissue engineering[98, 99, 103], and to visualize neural activities in mouse brains *in vivo* [19, 80].

1.2.7 Light Field Microscopy

High-speed, large-scale three-dimensional (3d) imaging of samples poses a major challenge in optical imaging. Light-field microscopy (LFM) is a 3D high-speed imaging method that has been applied to nonbiological and fixed biological samples [104-106]. Comparing to conventional imaging schemes, a LFM captures both the 2D location and 2D angle of the incident light by placing a microlens array in the native image plane such that sensor pixels capture the rays of the light field simultaneously and such 4D light fields allow the synthesis of a focal stack computationally [104]. Since no scanning process is needed, this technique can achieve high-speed volumetric imaging and has been reported to capture the dynamics of spiking neurons in volumes of ~700 μm × 700 μm × 200 μm at 20 hz for simultaneous functional imaging of neuronal activity at single-neuron resolution in an entire Caenorhabditis elegansand in larval zebrafish brain [104]. While diffraction places alimit on the product of spatial and angular resolution in these light fields, the penetration depth is also limited [106].

1.3 Goals and objectives

Three-dimensional FLOT can achieve resolutions of 100-200 μm and penetration depths of 2-3 mm. FLOT has been used in tissue engineering, neuroscience, as well as oncology. The limited dynamic range of the charge-coupled device-based system makes it difficult to image fluorescent samples with a large concentration difference, limits its penetration depth, and diminishes the quantitative accuracy of 3D reconstruction data. In Chapter 3, by incorporating the high-dynamic-range (HDR) method widely used in digital cameras, we present HDR-FLOT, which can increase penetration depth and improve the ability to image fluorescent samples with a large concentration difference. The method was tested using an agar phantom and a B6 mouse for brain imaging *in vivo.*

In Chapter 4, we applied angled FLOT (aFLOT) to record 3D neural activities evoked in the whisker system of mice by deflection of a single whisker *in vivo*. A 100 μm capillary and a pair of microelectrodes were inserted to the mouse brain to test the capability of the imaging system. The results show that it is possible to obtain 3D functional maps of the sensory periphery in the brain. This approach can be broadly applicable to functional imaging of other brain structures.

Regenerative medicine has emerged as an important discipline which aims to repair injury or replace damaged tissues or organ by introducing living cells or functioning tissues. Successful regenerative medicine strategies will likely depend upon a simultaneous optimization strategy for the design of biomaterials, cell-seeding methods, cell-biomaterial interactions, and molecular signaling within the engineered tissues. The imaging modality to assess the three-dimensional (3-D) structures and

functions of the cell-seed scaffold remains a challenge in mesoscopic scale (>2~3 mm). In Chapter 5, we investigated the different applications of aFLOT in bone tissue engineering. First we demonstrated the depth-resolve capability of aFLOT and ability to quantify cell density inside a scaffold. Then, the 3D printed bone osteons were evaluated using aFLOT to show its capability in accurately differentiating distinct cell populations. The 3D migration process of cells was also visualized and quantified using the aFLOT system. Finally, aFLOT was used to image the mineralization of alginate scaffolds seeded with human mesenchymal stem cells (hMSCs) by measuring hydroxyapatite (HA) deposition.

OCT can provide high-resolution morphology information, but is less sensitive to biochemical or molecular processes associated with early neoplastic formation before the exhibition of structural alterations. Fluorescence imaging has high sensitivity for detecting biochemical and molecular alterations, but has limited specificity [107]. Combining these two complementary imaging technologies would potentially improve the diagnostic capability for early cancer detection. In Chapter 6, we investigated the feasibility of a novel multi-modal optical imaging approach including high-resolution OCT and high-sensitivity FLOT for structural and molecular imaging. The C57BL/6J-Apc^{Min}/J mice were imaged using OCT and FLOT, and the correlated histopathological diagnosis was obtained. Quantitative structural (scattering coefficient) and molecular (relative enzyme activity) parameters were obtained from OCT and FLOT images for multi-parametric analysis. This multi-modal imaging method has demonstrated the capability for more accurate diagnosis with 88.23% (82.35%) for sensitivity (specificity) compared to either modality alone. This study

suggested that combining OCT and FLOT is promising for subsurface cancer detection, diagnosis, and characterization.

Furthermore, in Chapter 7, we applied OCT and FLOT to quantify the 3D mAb-IR700 distribution in tumor and therapeutic effects during and after PIT in real time and *in vivo*. To verify the results, we designed a minimally invasive two-channel fluorescence fiber imaging system by combining the traditional fluorescence imaging microscope with two imaging fiber bundles (~0.85 mm). This method can monitor mAb-IR700 distribution and therapeutic effects during PIT at different intratumor locations (e.g., tumor surface vs. deep tumor) *in situ* and in real time simultaneously. This enabled evaluation of the therapeutic effects *in vivo* and treatment regimens. The average IR700 fluorescence intensity recovery after PIT to the tumor surface is 91.50%, while it is 100.63% in deep tumors. Also two-photon microscopy combined with a microprism was also used to record the mAb-IR700 distribution and fluorescence intensity of green fluorescent protein (GFP) at different tumor depths during PIT. After PIT treatment, there was significantly higher IR700 fluorescence recovery in deep tumor than in the tumor surface. This phenomenon can be explained by increased vascular permeability immediately after NIR-PIT. Fluorescence intensity of GFP at the tumor surface decreased significantly more compared to that of deep tumor and in controls (no PIT).

Lastly, the novelty and impact of each project is concluded in Chapter 8, and other potential applications are suggested. The limitations and the future improvements are also discussed.

Chapter 2: Laminar optical tomography (LOT) *

2.1 Introduction

Laminar optical tomography (LOT) was initially developed to image absorption contrast for hemodynamic changes. [91, 95, 108, 109] Soon after, it was rapidly adapted to fluorescent molecular imaging, applications termed either fluorescence laminar optical tomography (FLOT)[80, 93, 94, 109] or mesoscopic fluorescence molecular tomography (MFMT). [98, 99] Similar to diffuse optical tomography (DOT), [110] LOT uses an array of photon detectors or a charge coupled device (CCD) camera to collect photons emitted from locations at different distances away from the illumination position, enabling simultaneous detection of scattered light travelling through different depths in the tissue. LOT is sensitive to both absorption and fluorescence contrasts providing an axial resolution of ~100-200 microns with several millimeters imaging depth. [80, 91, 93, 111] Recent studies demonstrated that angled illumination or detection modification (termed aFLOT) improves both resolution and depth sensitivity. [80, 112] Another rapid, non-contact depth-resolved imaging method called modulated imaging (MI) has also been developed for quantitative, wide-field characterization of optical absorption and scattering properties of turbid media, utilizing frequency-domain sampling and model-based analysis of the spatial modulation transfer function (s-MTF). [113-115]

---

* Part of the contents in this chapter is reproduced from "Q. Tang, J. Lin, V. Tsytsarev, R. S. Erzurumlu, Y. Liu and Y. Chen, "Review of mesoscopic optical tomography for depth-resolved imaging of hemodynamic changes and neural activities," ***Neurophotonics*** 4(1), 011009-011009 (2016)" with permission.

2.2 LOT basic principle

The working principle of LOT is based on light transport in tissues, [90] which includes three primary physical processes: scattering, absorption, and fluorescence. The relative probability of occurrence for each process depends upon the type of sample imaged and the wavelength of light used.[116] For *in vivo* brain imaging, scattering is the prevalent phenomenon. During light propagation, some of the photons will scatter out from the surface of the tissue. These photons will be captured by the detectors near the tissue surface with various separations from the light illumination/entrance position (source-detector separations). The light emerging at greater distances (i.e., larger source-detector separation) has a higher statistical probability of having travelled deeper into the tissue. By detecting the emerging light for a range of positions with different source-detector separations, it is possible to perform depth-resolved imaging of subsurface tissue structures through a proportional relationship between the source-detector separations and the average investigation depths. [109] Fig. 1 (a) shows the cross-sectional diagram of a typical LOT source-detector configuration and representative photon paths. The detection geometry used in LOT is similar to the detection geometry used in DOT. In contrast to DOT, where source-detector separations are typically several centimeters, [20] LOT utilizes smaller source-detector separations (from several tens of microns to a few millimeters). As a result of this difference, information from a relatively shallow depth (millimeter or mesoscopic scale) is collected by the detectors, enabling tomographic imaging with a higher resolution compared to that of DOT. [103]

2.2.1 Mathematical expression of LOT based on fluorescence contrast

The linearized relationship (Born Approximation) between the measured fluorescence signals *F* and the steady-state fluorescence distribution *O* at position *r* can be expressed as [90, 103]

$$F(\overrightarrow{r_n}, \overrightarrow{r_m}) = \frac{1}{4\pi} \int S(\vec{r} - \overrightarrow{r_n}) \cdot \mathrm{O}(\vec{r}) \cdot G(\overrightarrow{r_m} - \vec{r}) d^3\vec{r} = W_{n.m}\mathrm{O}(r) \quad (1)$$

Where

$$\mathrm{O}(\vec{r}) = \varepsilon_{\mathrm{ex}} \cdot \mathrm{c}(\vec{r}) \cdot \gamma \quad (2)$$

S is the distribution over $\vec{r}$ from the excitation photon radiance in the tissue resulting from a source at position $\overrightarrow{r_n}$ (related to the absorption and scattering coefficients, tissue anisotropy and refractive index of the tissue at this excitation wavelength). G is the probability that a photon emitted by a fluorescence source at position $\vec{r}$ within the tissue will be detected by the detector at $\overrightarrow{r_m}$ (related to the absorption and scattering coefficients, tissue anisotropy and refractive index of the tissue at this emission wavelength respectively). $\varepsilon_{\mathrm{ex}}$ is the extinction coefficient of the fluorophores at the excitation wavelength, $\mathrm{c}(\vec{r})$ is the concentration of the fluorophore, and γ is the fluorescent quantum yield of the fluorophores. Thus, the measured fluorescence signals and the fluorescence distribution are related by *W*, which is referred to as the weight matrix or sensitivity (Jacobian) matrix and represents the likely paths (spatial sensitivity) into which the scattered photons have travelled, and also back out of the tissue. Since the fluorescence emission will always result in a longer wavelength from that of the excitation light, *W* must account for the different absorbing and scattering properties at the excitation and emission wavelengths. One common scenario for functional brain imaging is described as follows. The tissue is already fluorescent at the initial stage (e.g. loaded with voltage-sensitive dye), and then a local signal

perturbation occurs (increase or decrease) in the fluorescence at a discrete region after an intended stimulation, which is similar for absorption case. Equation 1 can be then expressed in the following way:

$$\Delta F(\overrightarrow{r_n}, \overrightarrow{r_m}) = \frac{1}{4\pi} \int S(\vec{r} - \overrightarrow{r_n}) \cdot \Delta O(\vec{r}) \cdot G(\overrightarrow{r_m} - \vec{r}) d^3\vec{r} = W_{n.m} \Delta O(\vec{r}) \,, \qquad (3)$$

where the small signal change ΔF results from a small change in fluorescence distribution ΔO. We can imagine that when a photon interacts with a fluorophore, the photon is absorbed and a photon with a longer wavelength is emitted, which is an incoherent process so the photon loses all knowledge of its previous propagation status. So the emission fluorescence will scatter in an isotropic way within the tissue. Furthermore, it is preferable to normalize the equation into the form known as 'Normalized Born'. As shown in Equation 4, the measured fluorescence signal is normalized by F_0 (the signal measured before perturbation) and the right hand side of is similarly divided by $\emptyset_0$(the expected fluorescence simulated on a homogeneous medium).

$$\frac{\Delta F}{F_0} = \frac{W}{\emptyset_0} \Delta O. \qquad (4)$$

By using 'Normalized Born', it is very helpful to cancel the systematic errors related to measurements (e.g. variations in gain between each detector). [20, 91, 117] Also, in fluorescence LOT measurements, fluorescence signals detected from shallower layers are much stronger than those from the deeper perturbation signal. By normalizing to the original signal, it becomes possible to measure the change in fluorescence before and after the perturbation at different depths within a proper dynamic range. [20]

2.2.2 Mathematical expression of LOT based on absorption contrast

For the absorption case, the detected photons scatter along a random walk path from the source to the detectors and usually the scattering is predominantly in the forward direction, so we assumed that each scattering event causes a relatively small change to the direction of the photon. The perturbed radiance can be expressed as [39]:

$$\Delta M(\overrightarrow{r_n}, \overrightarrow{r_m}) = -\frac{1}{4\pi}\int M_0(\vec{r} - \overrightarrow{r_n}) \cdot \Delta\mu_a(\vec{r}) \cdot G(\overrightarrow{r_m} - \vec{r}) d^3\vec{r} = W_{n.m}\Delta\mu_a(\vec{r}), \quad (5)$$

Where $$M_0(\overrightarrow{r_n}, \overrightarrow{r_m}) = \frac{1}{4\pi}\int S(\vec{r} - \overrightarrow{r_n}) \cdot G(\overrightarrow{r_m} - \vec{r}) d^3\vec{r}, \quad (6)$$

M_0 is the measurement of a homogeneous background. ΔM is the small change in measurement results from a small change in absorption $\Delta\mu_a$, while W in this absorption case needs not account for the change of excitation and emission wavelengths. Similar to Equation 4, the normalized form for LOT based on absorption contrast is expressed as [20]:

$$\frac{\Delta M}{M_0} = \frac{W}{\varphi_0}\Delta\mu_a. \quad (7)$$

M_0 represents the signal measured before a perturbation and φ_0 represents the simulated signal expected from the tissue in the absence of the perturbation in absorption case. [20]

2.3 Forward modeling in LOT

The spatial sensitivity matrix W can be predicted using light propagation models, in which tissue scattering and absorbing properties, fluorophore characteristics (extinction coefficient and quantum yield), and the relative positions of the light source and detectors must be included. Several methods have been used to model

photon propagation in scattering samples. [118, 119] Two common types of forward modeling methods are summarized below.

2.3.1 Radiative transfer equation based model

Time-dependent Radiative Transfer Equation (RTE) can be used to accurately describe photon migration through tissue. [120] The Diffusion Approximation (DA) to the RTE is often applied since solving RTE is complex and computationally expensive, and there are analytic solutions to the infinite and semi-infinite geometry with different boundary conditions of the diffusion equation. [121, 122] DA has been the preferred forward model in DOT due to its computational efficiency and ease of implementation. [103, 118] It has been shown that DA cannot account for boundary measurements when there are structures within the scattering length from the surface of superficial tissues. [123, 124] In other words, DA is invalid and will not provide accurate results for the small source-detector separations typically used for LOT in mesoscopic regime.

An improved diffusion approximation to radiative transport, delta-P1 approximation, has been developed and validated for LOT.[125] While delta-P1 approximation can improve the computational efficiency, the estimation accuracy is moderate (with relative errors ~40%). Also, there are larger relative errors when source–detector separations are very small or when the heterogeneity is very close to the source or detectors due to the intrinsic limitations of the diffusion model. [125] However, for some applications where high speed is needed, delta-P1 approximation can be a good choice, especially for LOT based on fluorescence contrast. Furthermore, by taking advantage of the delta-isotropic phase function, the phase function

corrected (PFC) DA approach improves the performance of the DA and agrees with experimental results to an excellent degree, opening a potential for modeling photon propagation in LOT.[126]

2.3.2 Monte Carlo methods

By tracing the random walk steps that each photon packet takes when it travels inside the tissue, the Monte Carlo (MC) method has been used for simulating light transport in tissues for over three decades. [127, 128] MC provides a flexible and rigorous solution to the problem of light transport in turbid media with a complex structure. [129, 130] The MC method is able to solve the radiative transport equation (RTE) with a desired accuracy, hence it is well suited to simulating the light propagation in mesoscopic regimes. [103, 123, 130, 131] Compared to other analytical or empirical methods, large packets of photons need to be simulated (10^5 to 10^9) to obtain simulations with stochastic accuracy, requiring intensive computation and a great deal of time. A variety of methods for speeding up MC simulations, including scaling methods, [132] perturbation methods, [133] hybrid methods, [134] variation reduction techniques, [135] and parallel computation [136, 137] have been developed. [130] The majority of LOT/MFMT work employs the Monte Carlo method to compute the optical forward problem. [80, 93, 95, 103, 138, 139] Most of the current LOT/MFMT results used only homogenous forward models for generation of the spatial sensitivity *W*, while heterogeneities (such as large blood vessels and different tissue layers) could feasibly be considered into the forward model to achieve improved fitting between the data and the model. [20, 140] However, since the photon path becomes more uncertain as they scatter further, especially in complexed biological tissues, the mismatch between the mathematical

model prediction and actual measurement may cause the degradation of resolution as a function of depth. [20, 80, 109]

2.4 Image reconstruction for LOT

After knowing *W*, the next step is to solve Equation (3) or (4) to estimate the 3D distribution of the fluorescence (or absorption) changes ΔO(or $\Delta\mu_a$). It is challenging to solve the inverse problem since the number of measurements available are often much smaller than the number of unknown 3D image elements (voxels), which may result in a non-unique solution. [141] Moreover, compared to transmittance geometry, solving the inverse problem for reflectance geometry is more challenging due to limited angular sampling. [142] The typical approach to solve the inverse problems is to minimize $L = W\Delta O - \Delta F$ (or $L = W\Delta\mu_a - \Delta M$) using an iterative solver, with the estimate ΔO(or $\Delta\mu_a$) updated iteratively to minimize L until a preset number of iterations is reached or when *L* is below a set value (tolerance). [103] The most common iterative methods employed in the field are the conjugate gradient (CG) method, [98] the least squares (LSQR) method, [97, 143] and algebraic techniques. [94, 144] However, only using these iterative solvers is still not enough since the system is ill-conditioned and very sensitive to noise propagation. [103] A regularization term is required to tolerate small mismatches between the actual measurement and the prediction using the forward model, which could result from systematic errors or noise and inaccuracies in the light propagation model. [20] One typical formulation of the inverse problem in LOT/MFMT is:

$$\Delta O = W^T(WW^T + \lambda I)^{-1}\Delta F (or\ \Delta\mu_a = W^T(WW^T + \lambda I)^{-1}\Delta M), \quad (8)$$

where λI is a regularization factor which dictates how well the data (ΔO(or $\Delta\mu_a$)) fits the model ($W\Delta O$(or $W\Delta\mu_a$)). [20] It becomes the Tikhonov regularization if I is the identity matrix, which has been commonly used in LOT/MFMT. [91, 112] Large values of λ will generate superficially-weighted smooth images with underestimated quantification. [20] Radially variant λI has the potential to minimize high-frequency noise in the reconstructed image and produce constant image resolution and contrast across the image field, [145] with I being a diagonal matrix whose elements are the square-root of the corresponding diagonal elements of W^TW ,[98, 146] and λ can be selected via L-curve analysis. [147]

2.5 LOT instrumentation

The first LOT system was reported in 2004. [91] Since then, several improvements or alternative designs have been investigated. [80, 96, 98-100, 109] We first summarize two representative LOT systems in the following sections, and then LOT/MFMT with variant configurations and time-resolved protocol are also covered.

2.5.1 LOT based on absorption contrast

In the living brain, the main absorption contrast relies on the distinctive absorption spectra of oxy- and deoxyhemoglobin (HbO_2 and HbR). At visible and near-infrared (NIR) wavelengths, hemoglobin in blood is the most significant absorber. Changes in blood flow, blood volume, and oxygenation can be induced following functional activities in the brain. [148] Changing the oxygenation status of blood can be inferred from the changes in the relative concentrations of HbO_2 and HbR. In this way, absorption properties of the brain can be related to the variations in

the oxygenation state of hemoglobin and further connected to the localized neural activities. In brain research, the cortical hemodynamic response to stimulus provides a detectable signal, which can report the presence and location of neuronal activation. [95, 149, 150] Furthermore, by using different wavelengths of excitation lights and the known absorption spectra of HbR and HbO_2, the changes in the concentration of HbO_2 and HbR can be calculated. One of the main advantages of the method based on absorption contrast is that there is no need to use any extrinsic chemical probes, which makes this approach more feasible for clinical translation. The scattering of brain tissues is often assumed to not change significantly during the hemodynamic response [3]. While this method can record the hemodynamic responses to functional activations in the brain, the interrelation between neural activities and hemodynamic changes is still an area of intense research. [151-156]

The general schematic of a LOT system based on absorption contrast is shown in Fig. 1 (b). [95] Illumination light from one or more lasers is first coupled into a fiber and then collimated. The collimated light then passes through a polarizing beam splitter and is steered by a pair of galvanometer scanning mirrors onto a scan lens. Together with an objective lens, the beam is focused onto the surface of the tissue. Signals collected from the tissue will pass back up through the same light path and is de-scanned by the galvanometers. To be able to separate the incident light and the scatter light, a strongly polarized laser is normally used. Since specular reflections from optics and the tissue surface will maintain the same polarization, while light which has been scattered several times will lose its original polarization quickly. 50% of the scattered light emerging from the sample will be successfully separated from

specular reflections through the polarizing beam splitter. That successfully separated light then passes through a lens and is focused onto a linear fiber bundle or directly on the detector array. [95] Different from the pinhole setting in a confocal microscope, the line of fibers in the LOT system acts like 7 axially-offset pinholes, each leading to a separate detector corresponding to signals from different depths. As the focused beam is scanned over the surface of the tissue, scattered light emerging from the tissue at 7 different depths will be collected simultaneously by the seven avalanche photodiode detectors (APD), which result in seven 2D images per raster scan (e.g. if we choose 50 x 50 pixels over a 3.5 mm^2 field of view, then we have 50 x 50 = 2500 source positions and 50 x 50 x 7 = 17,500 measurements from all the detector positions.). A faster and more sensitive second generation LOT system which utilizes three excitation wavelengths and incorporates simultaneous imaging of both absorption and fluorescence contrast has also been reported. [109]

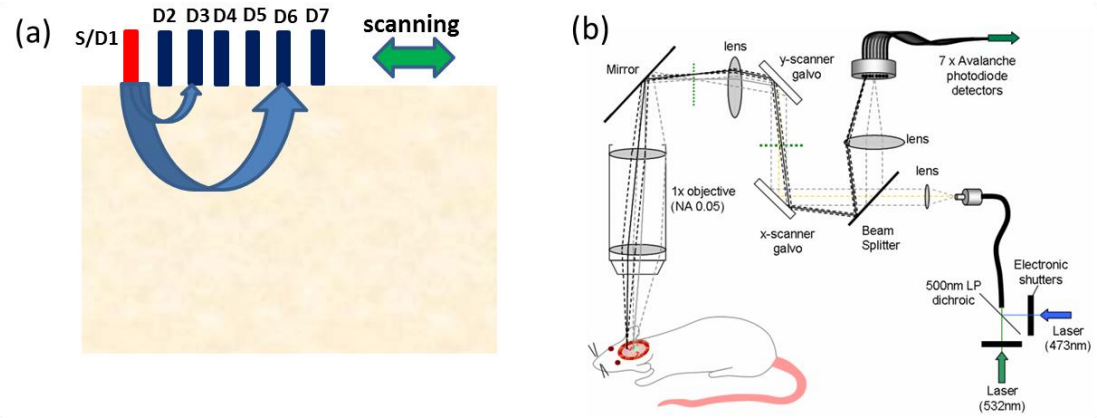

Figure 1. Schematic of LOT
(a) Schematic of LOT source (S) and detector (D1…D7) setup. (b) Laminar Optical Tomography system for depth-resolved hemodynamic imaging of rat cortex [95].

2.5.2 LOT based on fluorescence contrast

Exogenous fluorescent dyes, as well as novel transgenic methods, can also provide highly specific optical contrast enhancement. They can report functional parameters such as changes in membrane potential (voltage-sensitive dyes, VSD) or ion concentrations (pH-, Calcium-, Chloride-, Potassium-sensitive dyes). [5, 157] Compared to hemodynamics imaging based on absorption contrast (slow signal changes ~ second time scale), fluorescence signal change originates directly from rapid changes of neural activities, which is at the millisecond scale. [5]

The main difference of the LOT system based on fluorescence contrast compared to the LOT based on absorption contrast is the use of a dichroic mirror (for fluorescence) or a polarizing beam splitter (for absorption), and a long-pass or band-pass optical filter (depending on the type of fluorophores) before the detectors to further block the excitation light. Fig. 2 (a) shows one schematic diagram of a recently developed line-scanning aFLOT system. [80] The excitation light from a 637 nm laser diode is collimated and then coupled into a fiber to shape the light beam. An objective lens is then used to collimate the light from the fiber and the collimated light is further expanded into line-field illumination using a cylindrical lens. The emitted fluorescent light is collected through the objective lens, dichroic mirror, emission filter, and finally focused onto a high-speed CCD camera. Since the illumination light path is not confocal with the emission light path, the dichroic mirror is optional. Both fluorescence and reflectance images can be recorded by changing the corresponding filters. This system achieves scanning by moving the sample, using

a precisely controlled motor stage laterally in the scanning direction (perpendicular to the line illumination direction). [80] The acquired image is in XYS format (where X and Y represent X and Y dimensions of the 2D image acquired by CCD, S represents the different scanning positions, X= 184, Y=128; S=120, with a pixel size of ~23 μm in the specific system introduced.). To reconstruct the images, the first-order Born approximation between the measurement and the fluorophore distribution was applied on the cross-section FOV_{XZ}, with 100 source-detector pairs and 100 scanning positions chosen to constitute 10,000 measurement modes. [80] And each reconstructed FOV_{XZ} including 100x100 pixels with a pixel size of ~23 μm. Weight matrix W is therefore of size 10000×10000. [80] Finally, the 3D FOV_{XYZ} was constituted by superimposing individual FOV_{XZ} in the Y direction (illumination line direction). [80] Although a Graphics Processing Unit (GPU) was applied for parallel computation, the reconstruction process for one 3D image still takes around 10 minutes. However, with parallel computation developing so rapidly, we definitely believe that the time needed for Monte Carlo modeling and image reconstruction will not be a concern in the future.

2.5.3 LOT/MFMT with variant configurations

Several LOT/MFMT systems have been reported using different source/detector and scanning configurations, including point scanning with sparse array detection, [93] point-scanning with dense array detection, [97] and line-scanning with dense array detection. [94, 102] Laser diodes or solid-state lasers are typically chosen as the light source. [103] A point-focused light illumination with a 1D array detector is usually used in the LOT/MFMT system. [93] 3D images are obtained through 2D raster scanning of

the illumination point as shown in Fig. 1 (b). Alternatively, a line-field illumination with a 2D-array detector (CCD or electron multiplying CCD (EMCCD), or 2D-photomultiplier tube (PMT)) can be utilized, and then only 1D scanning is required to acquire the 3D information as shown in Fig. 2(a). Line-scan imaging can alleviate the complicated 2D scanner design. While similar to confocal microscopy, the line illumination mode potentially decreases the axial resolution. [158]

We should note that in LOT/MFMT, a detector closer to the illumination source will receive high light intensity, while a detector with larger source-detector separation collects a much lower signal, meaning that the detector with a larger source-detector separation may need higher gain. If possible, each detector's gain should be chosen to match its optimal signal intensity. However, when using CCD/EMCCD as the array detector, all pixels have the same gain and exposure time, which is a main drawback of such a design and may limit the system's dynamic range.

2.5.4 LOT/MFMT recording with time-resolved protocol

Hemodynamic response is usually slow and happens in seconds, therefore the LOT system with ~40 frames/s imaging speed can be utilized in studying hemodynamic responses. [95] In order to use LOT/MFMT to record VSD dynamics which reflects the cellular processes at the millisecond scale, [5] a new acquisition protocol has been investigated. [80, 93] Hillman et al. first reported a time-resolved FLOT system with an effective frame rate of 667 Hz imaging speed on perfused rat hearts. [93] Basically, it requires the biological response to be repeatable for each stimulation trial, and records the time relation of the acquired data with respect to the stimulus. Recently, Tang et al. used aFLOT to visualize neural activities in the living

animal brain using VSD. [80] One representative image acquisition protocols for time-resolved aFLOT is illustrated in Fig. 2 (b). The line-illumination light is focused on the border of the desired field of view (FOV) at the beginning of recording. An experimental session including all the time related images is acquired at each scanning position (e.g. for the whisker stimulation experiment, the experimental session consists of the recording before stimulus onset, and long-enough recording after stimulus onset to cover both the activation and recovery of neuronal signals). Then, another experimental session is performed to obtain the dataset at the next illumination/collection area by moving a step in the scanning direction. This process is repeated until the entire FOV is covered. The process is similar to previously published point-scanning FLOT. [93] For reconstruction of data recorded using the time-

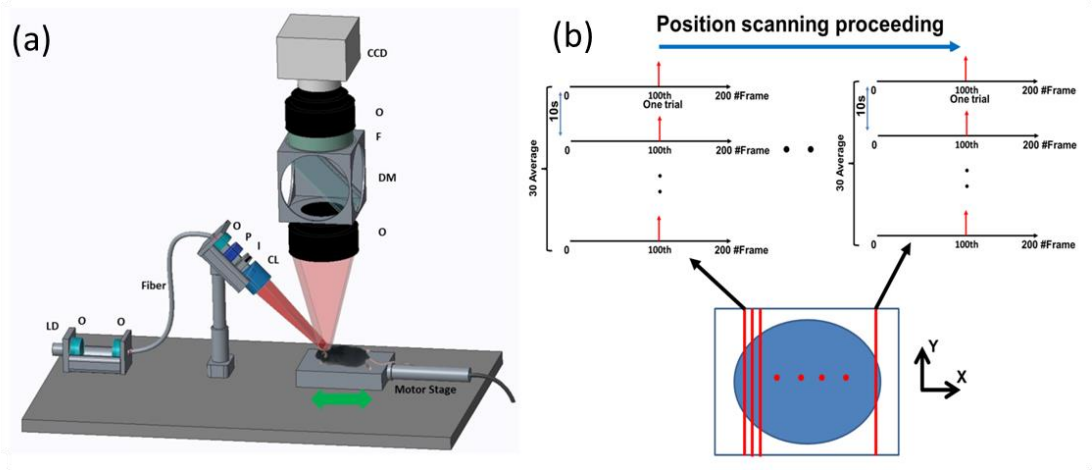

Figure 2. Schematic of the aFLOT system and Time-resolved protocol

(a) Schematic of the aFLOT system. LD: laser diode; O: objective lens; P: polarizer; S: shutter; I: iris; CL: cylindrical lens;F: filter; DM: dichroic mirror [80]. (b) Time-resolved image acquisition protocol [80].

resolved protocol, the measurements from multiple detectors at different scanning positions with the same frame number (or corresponding to the same time points in a dynamic process) should be firstly regrouped as one dataset. Then, the entire time course of 3D neural responses can be obtained by repeating the reconstruction process for all time points.

2.6. Conclusion

3D imaging techniques enabling examination of spatiotemporal patterns of samples will definitely provide more details in explaining both the structures and functions in the living/static objectives. In this chapter, we first review the fundamental basis of the LOT/MFMT system, including the Monte Carlo (MC) method which is usually used to model photon propagation, and common iterative methods and regularization models for image reconstruction. Specific LOT/MFMT systems based on absorption and fluorescence are described in detail, including the data acquisition process, data size, and image reconstruction process.

By adopting a microscopy-based setup and DOT imaging principles, LOT/MFMT can perform 3D imaging with higher resolution 100-200 μm than DOT and deeper penetration (2–3 mm) than confocal and two-photon microscopy. While, there is always a trade-off between axial resolution and penetration depth. Due to the limited penetration depth of LOT/MFMT, thinning or exposing the skull are usually necessary when imaging the cortical hemodynamic responses or neural activities using LOT/MFMT, which indicates that imaging the brain with LOT/MFMT is mainly applicable in small-sized animals. [80, 95] In such cases, LOT/MFMT has been focused on applications where tissues of interest are superficial, such as the exposed

mouse brain and skin, as well as oncological applications. [20, 100, 102, 159] For instance, LOT/MFMT has been applied to image skin cancers to describe the depth and thickness of pigmented skin lesions in clinical settings [159] and has also been employed to image the bio-distribution of a photodynamic therapeutic agent with ultrasound (US) co-registration in skin cancer models *in vivo,* though we can see there is still a long way to human clinical translation. [100] Imaging of internal organs using LOT/MFMT can be potentially achieved via endoscopic, intraluminal or an intra-surgical imaging setup. [20] Laser scanning microscopy (e.g. confocal and two-photon microscopy) aims to reject light that has been scattered to obtain high-resolution image of the tissue either by isolating the signal from the focus using a conjugated pinhole or by employing the non-linear effect. [84, 160] Instead, LOT/MFMT takes advantage of the scattered light so that they are much more sensitive to the optical signal changes in the tissue. LOT/MFMT obtains depth-resolved information by measuring the scattered light emerging from the tissue using detectors at different distances from the source illumination position, instead of scanning the tissue in the axial direction, which can dramatically improve the data acquisition efficiency. On the other hand, since the detected light undergoes multiple scattering in the tissue, the resolution of LOT/MFMT cannot compete with laser scanning microscopy. Moreover, estimation of photon migration using the mathematical models could not be exact, especially for the complicated biological tissues and the path of photons become more uncertain as they scatter further. LOT/MFMT faces resolution deterioration of these reconstructed images as a function of depth. [20, 80, 109] A combination of dense spatial data sets with regularization terms like compressive sensing based methods has the

potential to push LOT/MFMT resolution close to 100 μm or beyond, even at depths of several millimeters. [103] In terms of image visualization, since laser scanning microscopy uses a more 'direct' way to obtain intensity of every pixel in the image, it can achieve nearly real-time image feedback. While applying Monte Carlo modeling and regularization term to solve the inverse problem, LOT/MFMT has a high computational burden and is time-consuming especially for a system with high source-detector density as mentioned. As a result, for now, LOT/MFMT cannot provide the reconstructed image in real time, perhaps restricting the translation to clinical applications. With the advent of the supercomputer, the time needed for high-burden computation in LOT/MFMT could be alleviated significantly.

With the advantages of overcoming the scattering limit, offering relatively high resolution, multiplexing capabilities, large field of view, and high acquisition speed, LOT provides a promising imaging technique to investigate 3D neural activities in a minimally-invasive manner *in vivo*. By combining absorption and fluorescence LOT into one unit, it also has the potential to study neurovascular coupling since hemodynamic responses and neural activities can be imaged by absorption and fluorescence LOT respectively. Being able to achieve depth-resolved imaging of both absorption and fluorescence contrast, LOT/MFMT is also a promising non-destructive imaging tool in oncological applications and the tissue engineering area.

Chapter 3: High-dynamic-range fluorescence laminar optical tomography (HDR-FLOT)*

3.1 Introduction

In the FLOT system configuration, a charge-coupled device (CCD) or electron-multiplying CCD (EMCCD) can be used as the array detector since either one has a higher sampling density in comparison to a photomultiplier tube (PMT) array or an avalanche photodiode (APD) array [80, 103]. During signal collection in FLOT with reflectance imaging mode, the photons collected at larger source-detector separations have a higher statistical probability of travelling through deeper tissues. In general, the detector with a larger source-detector separation collects a lower signal compared to a detector closer to the illumination source, indicating that the deeper area will have a low signal-to-noise ratio (SNR), which will limit reconstruction accuracy [103]. We can increase either the excitation power or exposure time to enhance the collected signals from deeper regions. However, all pixels acquired from CCD/EMCCD have the same gain or exposure time, meaning that increasing the excitation power or exposure time will saturate the pixels near the illumination source very quickly.

* The contents in this chapter is reproduced from "Tang, Q. et al. High-dynamic-range fluorescence laminar optical tomography (HDR-FLOT). *Biomed. Opt. Express* **8**, 2124-2137 (2017)" with permission.

Another scenario occurs when imaging fluorescent samples with a large concentration difference (e.g., inhomogeneous dye loading, tumors at different stages), and the area with higher fluorescence concentrations will easily become saturated, while areas with a low fluorescence concentration will have a low SNR, which may affect the quantitative accuracy of FLOT. Ultimately, the insufficient dynamic range of the CCD/EMCCD limits the penetration depth and quantitative accuracy of FLOT.

A high-dynamic range (HDR) method based on a multiple-exposure scheme is widely used in digital cameras and smartphones [161-163]. Taking advantage of the multiple-exposure-based HDR method, HDR optical projection tomography (HDR-OPT), HDR laser-scanning microscopy (HDR-LSM), and HDR fluorescence molecular tomography (HDR-FMT) were recently reported [164-166]. Localization of fluorescent targets with a large concentration difference is effectively improved with HDR-FMT. Good quantitative accuracy was demonstrated in both the phantom and *in vivo* animal experiments [164].

In this paper, we present an HDR-FLOT method to increase both its dynamic range and penetration depth. To assess the potential of this method, we first fabricated an agar phantom in which three 150-μm capillaries filled with different concentrations of Cy 5.5 solution were inserted at similar depths. Then, we obliquely inserted one capillary within the brain of a mouse in vivo to illustrate the improved penetration depth of HDR-FLOT for brain imaging. Our data demonstrated the feasibility of HDR-FLOT in increasing the dynamic range and penetration ability of

FLOT, and provide a potentially improved mesoscopic tomography method for imaging neuronal activities.

3.2 Methods

3.2.1 Construction of 2D HDR fluorescence images

The basic idea of HDR-FLOT is to implement 3D reconstruction in FLOT based on 2D HDR fluorescence images [163, 164]. The first step to reconstruct 2D HDR images is to recover the CCD response function. The exposure *X* of a pixel can be defined as the product of irradiance *E* and the exposure time *t*, where irradiance *E* is influenced by the optical properties of the sample as well as illumination from the light source. From the CCD, we can obtain a digital number *Z* (CCD output), which is related with *X* at every pixel. We can define this relationship as CCD response function *f*. Since the background noise could cause deviation of the CCD response function, we first subtract the noise from the original CCD output, so that Z at every pixel will be:

$$Z = Z_{sample} - Z_{background} \tag{1}$$

Z_{sample} are the values of samples from CCD, and $Z_{background}$ are background values in the corresponding images. Then, we can denote the response function as:

$$Z_{ij} = f(\mathrm{E}_i \mathrm{t}_j) \tag{2}$$

where *i* is the index of pixels and *j* is the index of exposure time. Since *f* is monotonic, we can rewrite Eq. (2) as:

$$f^{-1}(\mathrm{Z}_{ij}) = \mathrm{E}_i\, t_j \tag{3}$$

Taking the natural logarithm of both sides, we can obtain:

$$\ln f^{-1}(\mathrm{Z}_{ij}) = \ln \mathrm{E}_i + \ln t_j \tag{4}$$

Then, we can rewrite the equation with a defined function $g = \ln f^{-1}$ as:

$$g(Z_{ij}) = \ln E_i + \ln t_j \tag{5}$$

The parameters *E* and function *g* are unknown, but there is a linear relationship between $g(Z_{ij})$ and $\ln E_i$. We change the problem to solving the quadratic objective function as follows:

$$O = \sum_{i=1}^{N}\sum_{j=1}^{T} \omega(Z)[g(Z_{ij}) - \ln E_i - \ln t_j]^2 + \sigma \tag{6}$$

where $\omega(Z)$ is a weighting function. When the signal is low or saturated, the pixel value *Z* and exposure *X* may fit the response function poorly. Thus, we may give smaller weighting to those pixels. Simply, we can define $\omega(Z)$ as [163]:

$$w(Z) = \begin{cases} Z - Z_{\min} & for\ Z \le \frac{1}{2}(Z_{\min} + Z_{\max}) \\ Z_{\max} - Z & for\ Z > \frac{1}{2}(Z_{\min} + Z_{\max}) \end{cases} \tag{7}$$

σ is introduced as a smoothness parameter to make sure that the function g is continuous and smooth [163]. The best estimate of CCD response function *g* will be obtained when *O* in Eq. (6) has its minimum value. The commonly used method to satisfy the equation is the least-square method for linear regression [163, 164].

Because of the limited memory of a computer, we pick 2500 pixels instead of all the 512*512 pixels for calculation (i.e., the sampling rate is 1/10). The best estimate of the CCD response function g will be obtained when O reaches its minimum value. After the CCD response function g has been obtained, we can calculate irradiance *E* by Eq. (5). The weighting function *w* is introduced again here to give a higher weighting value to data at reliable ranges (the middle of the response function), but a

lower value to the ranges near the extremes. Then, we can reconstruct the 2D HDR image as [163, 164]:

$$\ln E^{HDR} = \frac{\sum_{i=1}^{N}\sum_{j=1}^{T}\omega(Z_{ij})\left[g(Z_{ij}) - \ln t_j\right]}{\sum_{i=1}^{N}\sum_{j=1}^{T}\omega(Z_{ij})} \tag{8}$$

After that, we can obtain the 2D HDR image using all the images with different exposure times, and a series of 2D HDR images can be obtained at each scanning position, which will later be used for 3D HDR-FLOT reconstruction.

3.2.2 System setup

The schematic of the FLOT system is shown in Fig. 1(A), which is similar to the system reported previously [80, 167]. A pigtailed 637-nm laser diode was used as the light source (LP637-SF70, Thorlabs Inc.). Light from the pigtailed laser diode was first collimated by an objective lens. A cylindrical lens was used to shape the collimated light into a line-field illumination with a full line-width at the half maximum of ~26 μm at the focal plane. An iris was utilized to control the length of the line illumination. The backscattered light and emitted fluorescent light were collected back through another objective lens, a filter wheel (695-nm long-pass emission filter for fluorescence imaging and no filter for recording reflectance images), and finally onto a 12-bit CCD camera (EM-CCD, Cooke) [80]. A pair of polarizers was used to reject the specular reflection from the sample surface. The illumination angle was set at 45°, rendering an ~30° transmission angle in tissue (n~1.33) [80], as our previous studies indicated that angled illumination and detection configurations can improve both resolution and depth sensitivity [80, 112]. We set the

focal plane slightly below the sample surface to compensate for the defocusing effect. The sample was scanned laterally in the scanning direction X (perpendicular to the line illumination direction Y) using a motorized stage.

To co-register the FLOT fluorescence information with morphological/anatomical information, we also imaged the samples with optical coherence tomography (OCT). The OCT system shown in Fig. 1(B) was described previously [64, 94, 168, 169]. A wavelength-swept laser centered at 1310 nm with a 100-nm bandwidth was used in this frequency-domain OCT system as a light source [64, 94, 168]. The wavelength-swept frequency was 16 kHz and the output power from the laser was approximately 16 mW. About 97% of the laser power was split 50:50 to the sample and the reference arms of a fiber-based Michelson interferometer [64, 94, 168]. A balanced detector (BD) was used to receive the interference fringes from different depths encoded with different frequencies. The remaining 3% of the laser output power was sent to a Mach-Zehnder interferometer (MZI) to generate a frequency-clock signal with a uniformly spaced optical frequency to trigger the sampling of the OCT signal [64, 94, 168]. Then, a fast Fourier transform of the interference fringes was performed to obtain the depth-resolved axial profile [64, 94, 168].

3.2.3 Experimental design

All animal experiments were performed in compliance with the National Institutes of Health *Guide for the Care and Use of Laboratory Animals* (NIH Publication No. 80-23) and the protocol approved by the Institutional Animal Care and Use Committee of the University of Maryland, College Park campus.

(1) Phantom study

To demonstrate the capability of HDR-FLOT to image fluorescent samples with a large concentration difference, an agar phantom was fabricated with three 150-μm glass capillaries (ID: 0.15 mm, OD: 0.25 mm, VitroCom Inc.) inserted at similar depths filled with different Cy 5.5 concentrations. First, the three glass capillaries were filled with 2 μM, 1 μM, and 0.2 μM Cy5.5 solutions, respectively (Cyanine5.5 azide, Lumiprobe Corporation). The filled capillaries were then fixed side by side on the empty petri dish. Then, 1.5-g agar powder (Now Inc.), 0.3-mL 20% intralipid solution (Hospira Inc.), and 49-mL PBS buffer were mixed and stirred well. After heating in a microwave for ~2 minutes, the mixed liquid gel was poured into the petri dish on which the glass capillaries were fixed and the capillaries were submerged in the liquid gel. After the liquid gel cooled and solidified (~10 minutes), the gel was ready to be imaged. The scattering coefficient (μ_s) of the agar phantom was determined from the reflectance data using oblique-incidence spectroscopy to be ~2.3 mm^{-1} (g = 0.9, n = 1.33, μ_a= 0.01/mm, μ_s'= 0.23/mm at 635 nm) [170]. We further fabricated another agar phantom with 1.5-g agar powder, 2.5-mL 20% intralipid solution, and 49-mL PBS buffer, providing a reduced scattering coefficient μ_s'= ~1.2/mm at 635 nm, which is within the range of most biological tissue [171, 172]. To co-register 3D OCT and FLOT images, a piece of black tape was stacked on the phantom surface near the glass capillaries, as shown in Fig. 1(C), as a fiducial marker.

(2) Animal study

LOT/FLOT has been applied in recording 3D neural activities and hemodynamic responses in the mouse brain *in vivo* [80, 95]. Increasing the penetration depth would

broaden the application of FLOT for neuroscience research. Since the optical properties of the living mouse brain are too complicated to mimic using a simple phantom, a 150-μm glass capillary filled with voltage-sensitive dye (commonly used for reporting neural activities [5, 80, 173-175]) was inserted into a mouse brain *in vivo* to demonstrate the feasibility of HDR-FLOT to increase penetration depth.

A 4-5 month-old B6 mouse was anesthetized with urethane (1.15 g/kg body weight). The mouse's head was shaved before being placed into a stereotaxic frame (Stoelting Co.) [80, 173]. Then, a cranial window was made over the left parietal cortex (about 4×4 mm). The surface of the dura mater was cleaned with hemostatic sponges dipped in artificial cerebrospinal fluid (ACSF) as described previously [80, 173]. One 150-μm glass capillary filled with voltage-sensitive dye RH-1691 (Optical Imaging Ltd.; 1.0 mg/ml in ACSF) was then slowly inserted into the exposed area. The cortical surface was then covered with high-density silicone oil. The scattering coefficient (μ_s) of the living mouse brain was determined from the reflectance data using oblique-incidence spectroscopy (g = 0.9, n = 1.33, μ_a= 0.01/mm, μ_s'= 0.82 /mm at 635 nm) [80, 170]. The brain phantom was then imaged by OCT and FLOT subsequently.

3.2.4 Data acquisition and image reconstruction

For FLOT image acquisition, the excitation laser line was first focused on the border (X=0) of the sample field of view (FOV) [80]. At each scanning position, one 2D XY image (512x512, with pixel dimension of 30.8 μm) was obtained with different exposure times (e.g., 100 ms, 200 ms, 500 ms, 1000 ms, and 2000 ms). Next, the sample was moved by the motorized stage in the X direction with a step size of 61.6

μm to another illumination/collection position. Another 2D XY dataset with different exposure times was obtained. This process was repeated until scanning was completed on the entire sample [80]. The raw measurement had the format of XYT. A typical 3D dataset recorded 512×512×500 XYT voxels for five different exposure times. To fit the experimental data to the theoretical model used for 3D reconstruction, the sample surface should be found [80]. To obtain the surface profile of the samples, the same FOV was scanned with a 100 ms exposure time at lower laser power (driver current: ~40 mA) to avoid saturating the CCD camera. The emission filter was removed by rotating the filter wheel during the acquisition of the reflectance images. Without the emission filter, most of the acquired signal was from the reflection of the illumination light at the sample surface. This signal would then be used to indicate the location of the sample-air interface. The raw measurement of reflectance dataset had the same format of XYT (X=512, Y=512, T=100) [80]. The ROI was then imaged by the OCT system described above to obtain the 3D morphological tomography.

To reconstruct the FLOT tomograms, first, the fluorescence images with the same exposure time at different scanning positions were arranged as one group (e.g., the data set for all the images at different scanning positions with 100 ms exposure time: XYT_{100ms}, X=512, Y=512, T_{100ms}=100). The separated images were then applied to obtain the CCD response curve and to further construct the HDR images based on the protocol described in Section 2.1. After that, we had six data sets for each sample, five with different exposure times and one with a constructed HDR data set. Each 3D data set was then downsized to 256×256×100 voxels to match the pixel size in XYT

dimensions. The raw measurements of the reflectance data were stacked together according to the geometrical relationship between the illumination plane and the detection FOV, as described previously [80, 176]. The stacked reflectance data were also used to co-register 3D FLOT images with the 3D OCT data based on the black tape for the agar phantom and the shape of the mouse brain's blood vessels. Reconstructing the fluorescence images with different exposure times was via the same method as described previously [80]. We assumed a first-order Born approximation to obtain the linearity between the CCD measurement F (with background noise subtracted) and the fluorophore distribution C (i.e., for each FOV_{XZ}, $F = JC$, with J the weight or sensitivity matrix) [80, 167]. J was constituted by Monte Carlo simulation and the reciprocity principle. J was later decomposed by singular value decomposition (SVD) [80, 177]. Last, the undetermined system was solved by least square fitting and Tikhonov regularization [80, 112]; the regularization parameter was determined by the L-curve criterion [147, 178]. In our experiment, for each FOV_{XZ}, 100 source-detector pairs and 100 scanning positions starting from the surface were chosen to constitute F. Each reconstructed FOV_{XZ} was composed of 100×100 pixels with the same pixel size of ~61.6 μm. The 3D FLOT image (FOV_{XYZ}) was constituted by juxtaposing individual FOV_{XZ} along the Y-direction. Six 3D FLOT images (five with different exposure times and one with a constructed HDR data set) were reconstructed to compare their performances.

3.2.5 Data statistical analysis

Data are expressed as mean ± standard deviation. Statistical analyses were carried out using MATLAB. A Student's t-test was used to compare the response error ratio

(RER), diameter difference ratio (DDR), and penetration depth obtained from different exposure times and HDR mode. Statistical significance is considered at $P = 0.05$.

3.3 Results and Discussion

3.3.1 Co-registration of the 3D FLOT and OCT images

To obtain the distribution of the capillaries (e.g., depth and angle) in the agar phantom and living mouse brain, the samples were first imaged by the OCT imaging system. A piece of black tape was used as a landmark on the phantom surface near the glass capillaries [see Fig. 1(C)]. Fig. 1(D) and (E) show the images of the same black tape from the 3D stacked reflectance LOT data set and the 3D OCT data set, respectively. Fig. 1(F) presents the co-registered OCT and FLOT images using the black tape as a fiducial mark, which can guarantee that the structure provided by OCT is in the same ROI imaged by FLOT. Based on the OCT images, we can further evaluate the capability and accuracy of the HDR-FLOT system in the following studies.

3.3.2 Phantom study

Fig. 2(A) shows a representative cross-sectional OCT image of the phantom with three capillaries filled with Cy 5.5 solution. The locations of the three capillaries with different Cy 5.5 concentrations are indicated by the 3 differently colored arrows (red: 2 μM, yellow: 1 μM, green: 0.2 μM). All three capillaries are at similar depths of~650-750 μm. We denote them as C1 (2 μM), C2 (1 μM), and C3 (0.2 μM), respectively, in the following sections.

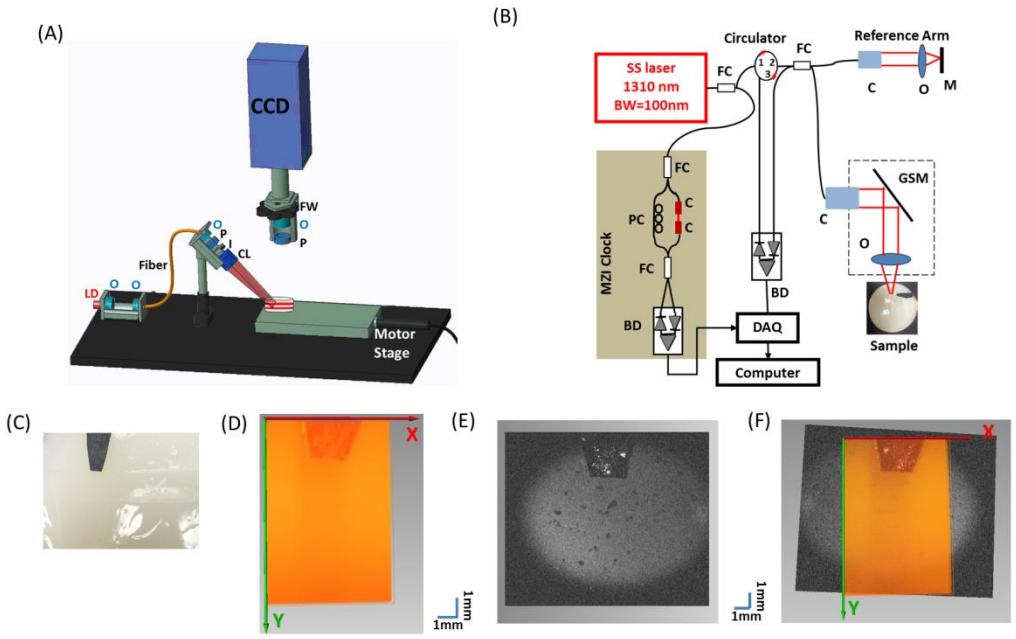

Figure 1. Schematic of the FLOT and OCT system

(A) Schematic of the FLOT system. (B) Schematic of the OCT system. FC: fiber coupler; PC: polarization controller; C: collimator, BD: balanced detector, MZI: Mach-Zehnder interferometer (frequency clocks), DAQ: data acquisition board, M: mirror, GSM: galvanometer scanning mirror, O: objective lens, LD: laser diode, P: polarizer, S: shutter, I: iris, CL: cylindrical lens, FW: filter wheel. (C) Photo of the black tape on the surface of the agar phantom. (D) Surface of the agar phantom from stacked 3D reflectance data. (E) Surface of the agar phantom from OCT. (F) Co-registered OCT and FLOT images by the black tape.

Fig. 2(B) is the 3D rendered image of these three capillaries from OCT. Fig. 2(C-E) show 2D images obtained from FLOT at one scanning position using exposure times of 100 ms, 500 ms, and 2000 ms, respectively. With an exposure time of 100 ms, C1 and C2 clearly stand out from the background, while C3 is difficult to distinguish. C3 appears when the exposure time is increased to 500 ms, while C1 starts to get saturated at this exposure time. Further increasing the exposure time to 2000 ms also increases the fluorescence intensity of C3 to the middle of the CCD signal range, while C1 and C2 are both saturated, which means we cannot recover the quantitative relationship of the fluorophore concentrations in these capillaries. Fig.

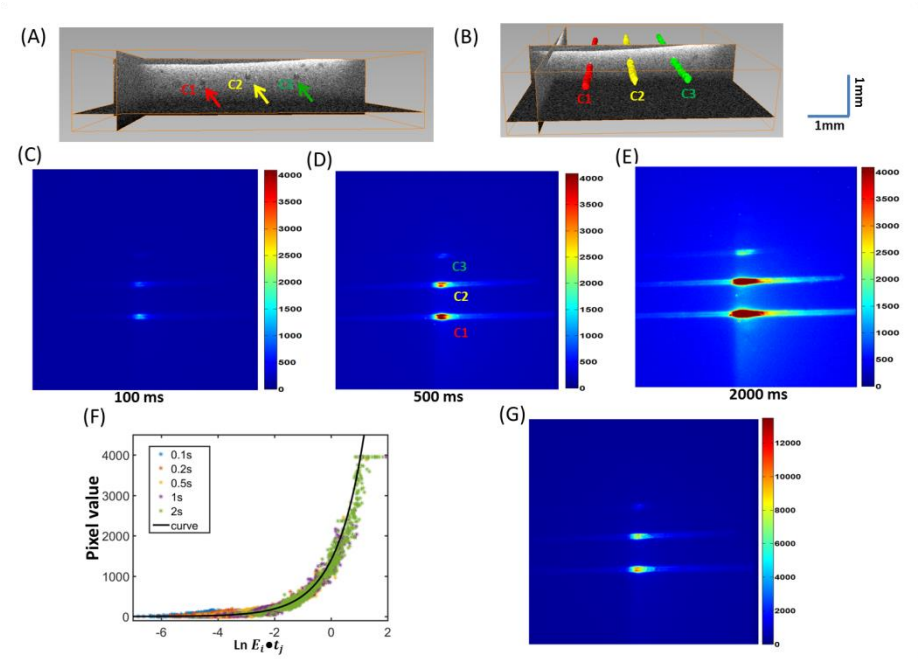

Figure 2. 2D FLOT raw images

(A) Image from OCT system of the three capillaries filled with Cy 5.5 solution, indicated by the 3 arrows (red: 2 µM (C1), yellow: 1 µM (C2), green: 0.2 µM (C3)). (B) 3D rendered images of the 3 capillaries from the OCT system. (C-E) 2D images obtained from FLOT using exposure times of 100 ms, 500 ms, and 2000 ms. (F) Recovered CCD response curve; the solid black line is the fitted curve (x axis is in loge scale). (G) Constructed 2D HDR-FLOT image.

2(F) shows the recovered CCD response curve obtained by using all of the images with five different exposure times. As the exposure time increases, the data points shift to the high range of the CCD and some points become saturated, indicating the limited dynamic range of the CCD system. The recovered CCD response curve and all the images with five different exposure times were then used to construct the 2D HDR fluorescence image, shown in Fig. 2(G). In the 2D HDR fluorescence image, the dynamic range of the fluorescence projection image is effectively improved. The relationship of the CCD response with the five different exposure times was further plotted in Fig. 3.

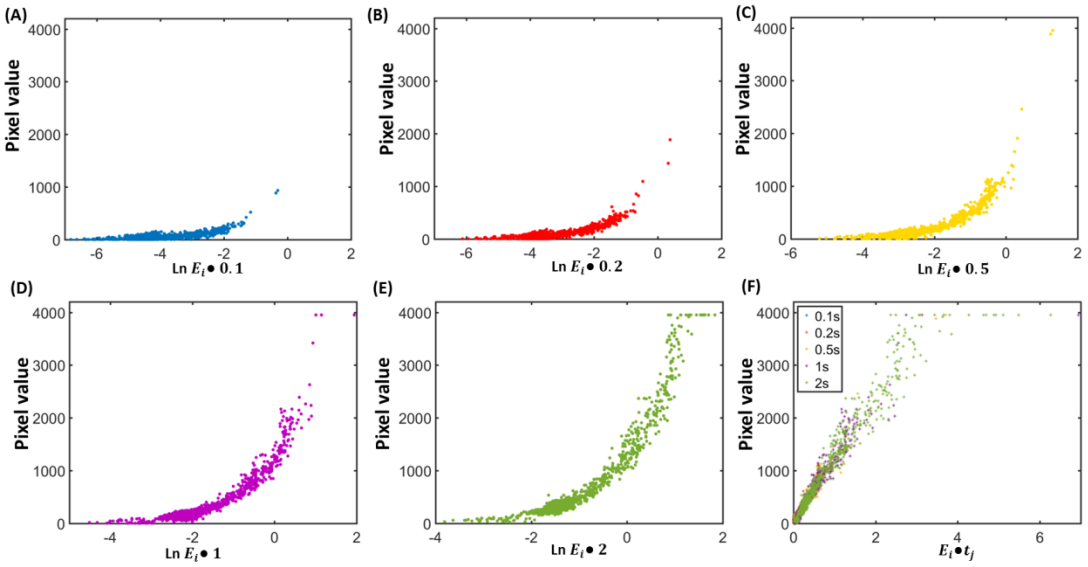

Figure 3. Relationship of the CCD pixel values with different exposure times
Relationship of the CCD pixel values with exposure time 0.1 s (A), 0.2 s (B), 0.5 s (C), 1 s (D) and 2 s (E) (x axis is in $\log_e$ scale). (F) Relationship of the CCD pixel values with different exposure times.

To assess the accuracy of the 2D HDR fluorescence images, the fluorescence value was averaged from a 5x5 region of interest (ROI) at 100 capillary positions for each capillary. The averaged fluorescence values were then normalized and plotted as a function of true Cy 5.5 concentration, as shown in Fig. 4. (We normalized the CCD values at 2 µM as 1, then normalized the CCD values at 1 µM and 0.2 µM to the CCD values at 2 µM.) The cyan dashed line depicts the ideal linear relationship of the normalized fluorescence values as a function of true Cy 5.5. With an exposure time of 100 ms, the fluorescence values from C1 and C2 perform well in linearity, while C3 is off the line and has a low quantitative accuracy, since the signal in this area is weak and has a low SNR [Fig. 4(A)]. Since the fluorescence signal from C1 has already been overexposed for data obtained with exposure times of 500 ms and 2000 ms, the linearity relationship is completely distorted and the fluorescence signals are unable

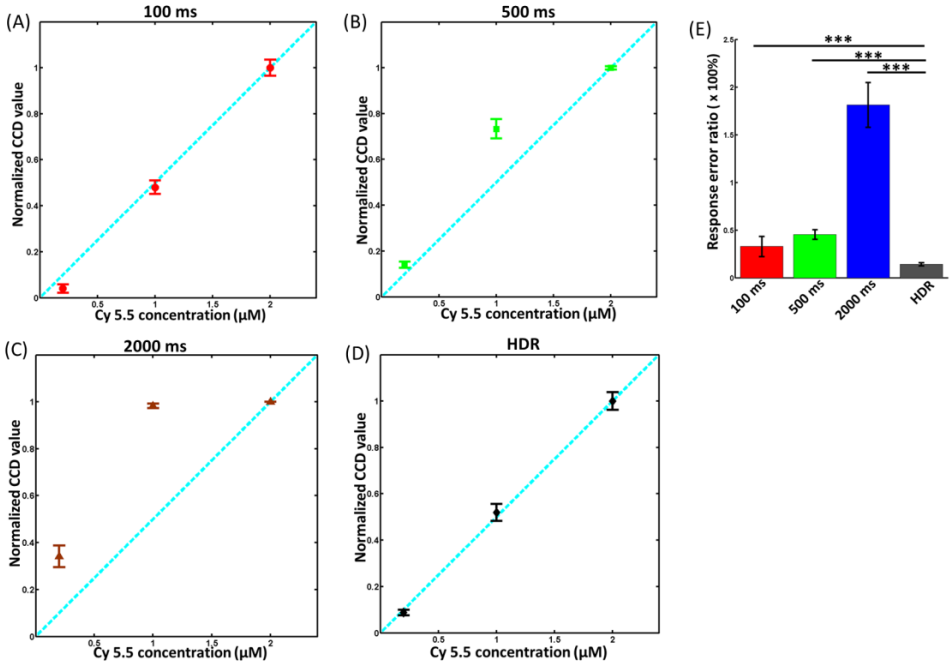

Figure 4. Quantifications of 2D FLOT images

Average fluorescence intensity of the raw 2D fluorescence images as a function of true Cy 5.5 concentration with exposure times of 100 ms (A), 500 ms (B), 2000 ms (C), and the HDR method (D). The fluorescence values were normalized to the maximum value (n=100). (E) Average CCD response error ratios with different exposure times (n=100).

to quantify the true Cy 5.5 concentration [Fig. 4(B) and (C)]. In comparison, the fluorescence signals from the constructed 2D HDR images show an excellent linear response to the true Cy 5.5 concentration [Fig. 4(D)]. To quantify the accuracy of normalized CCD values with different exposure times from the ideal linear relationship, the measured response error ratio (RER) was defined as following: $RER = |NCV - IV_p|/IV_p \times 100\%$, where NCV represents the normalized CCD values from measurements and IV_p represent the ideal values at different Cy 5.5 concentrations (since we normalized the CCD values at 2 μM as 1, we just need to calculate RER for $p = 1\ \mu M\ \&\ 0.2\ \mu M$ with $IV_{p=1\ \mu M} = 0.5, IV_{p=0.2\ \mu M} = 0.1$). We averaged the RER_s for $p = 1\ \mu M\ \&\ 0.2\ \mu M$ at each scanning position and further

averaged all the RER_s from all the 100 scanning positions. 2D HDR images present significantly smaller DDR within 15% of that from all the other exposure times [Fig. 4(E)].

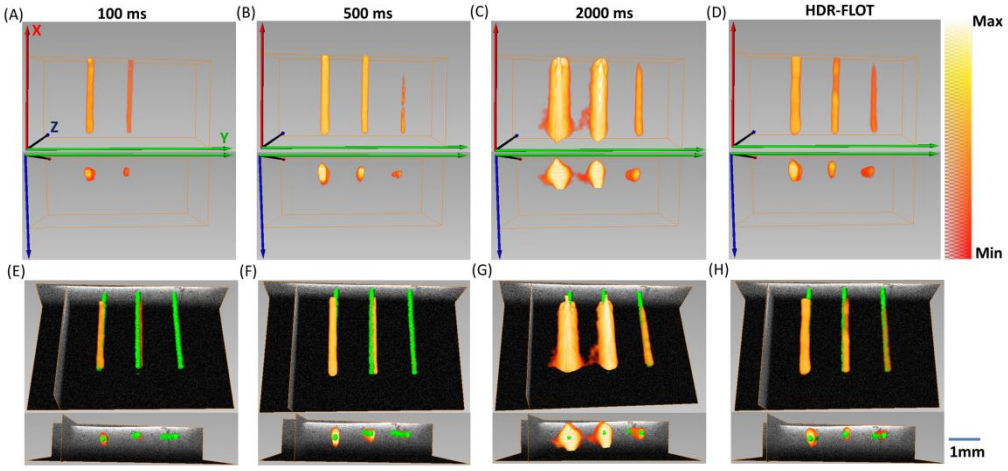

Figure 5. 3D FLOT reconstructed images in the agar phantom with μ_s' = 0.23/mm at 635 nm

(A-C) 3D FLOT reconstructed images with exposure time of 100 ms, 500 ms, and 2000 ms. (D) 3D HDR-FLOT reconstructed image. (E-H) Co-registered 3D FLOT reconstructed images with corresponding OCT images (green). The Max in the colormap is the maximum value in the image and Min represents the value: (Background + (Max-Background)/2).

Fig. 5(A-C) show the 3D FLOT reconstructed images with exposure times of 100 ms, 500 ms, and 2000 ms. As expected, C3 cannot stand out from the background with 100 ms exposure time [Fig. 5(A).]. Although increasing the exposure time will enhance the SNR of this capillary, the shapes of C2 and C3 become distorted because overexposure and noise become more apparent, as shown in Fig. 5(C). With 2D HDR fluorescence images, the 3D reconstructed image can resolve all three capillaries with different concentrations of Cy 5.5 simultaneously, as shown in Fig. 5(D). To quantify the fluorescence intensity of the reconstructed FLOT 3D images, the normalized average fluorescence intensities of the three capillaries were again plotted as a function of true Cy 5.5 concentrations, as shown in Fig. 6. Similar to the 2D data, the

3D FLOT images reconstructed with 2D HDR fluorescence images show the smallest *RER* within 20%.

To further assess the size accuracy of capillaries from the reconstructed 3D FLOT images with different exposure times, the 3D FLOT images were then co-registered with the corresponding 3D OCT images, as shown in Fig. 5(E-H). All the three capillaries from OCT data were labelled green for better visualization. The sizes of capillaries reconstructed from FLOT were evaluated as the diameter difference ratio (DDR) as follows:$\mathrm{DDR} = \frac{|D_{FLOT} - D_{OCT}|}{D_{OCT}} \times 100\%$, where D_{FLOT} is the diameter of the capillary measured from FLOT, and D_{OCT} is the diameter of the capillary measured from OCT, respectively. We first analyzed the DDR for FLOT with different exposure times at different Cy 5.5 concentrations, as shown in Fig. 6(F). HDR-FLOT and 2000 ms exposure time provide similar DDR which is better than those from 100 ms and 500 ms at the lowest Cy 5.5 concentration (0.2 μM). At the modest Cy 5.5 concentration (1 μM), the best DDR comes from 500 ms, while HDR-FLOT also presents relatively good DDR. When it goes to high Cy 5.5 concentration (2 μM), 100 ms offers the best DDR with HDR-FLOT the second-best. Then we define the average DDR was the mean of the three DDRs calculated from the three capillaries. As shown in Fig. 6(G), the averaged DDR is around 46% with an exposure time of 100 ms and C3 cannot be resolved ($D_{FLOT} = 0$ since C3 cannot be resolved at this exposure time). When the exposure time increases, averaged DDR increases, indicating the sizes measured from FLOT deviate from the correct values. HDR-FLOT presents significantly better average DDR (within 40%) than any of the other three cases and with all the three capillaries clearly displayed.

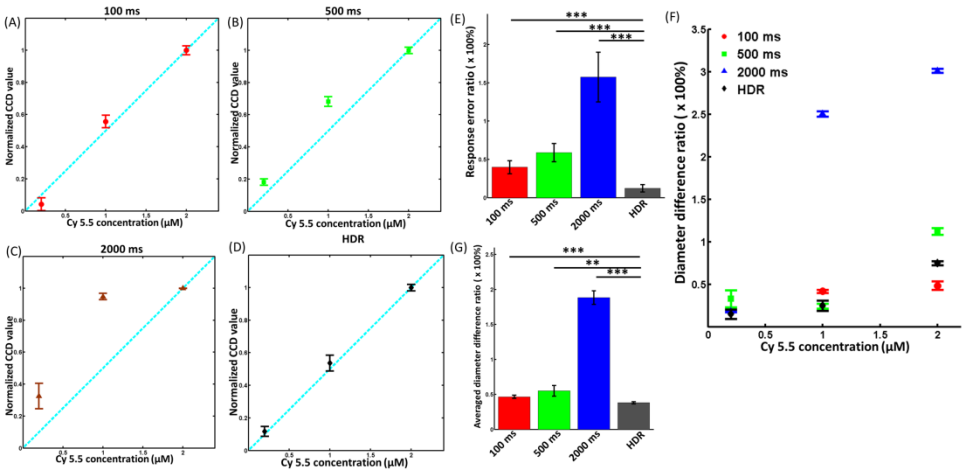

Figure 6. Quantifications of 3D FLOT images

Average fluorescence intensity of the 3D images as a function of true Cy 5.5 concentration with exposure time 100 ms (A), 500 ms (B), 2000 ms (C), and the HDR method (D). The fluorescence values were normalized to the maximum value (n=50). (E) Average fluorescence response error ratios with different exposure times (n=50). (F) Diameter difference ratios for FLOT with different exposure time at different Cy 5.5 concentrations compared to OCT data (n=50). (G) Average diameter difference ratios for FLOT with different exposure times compared to OCT data (n=5).

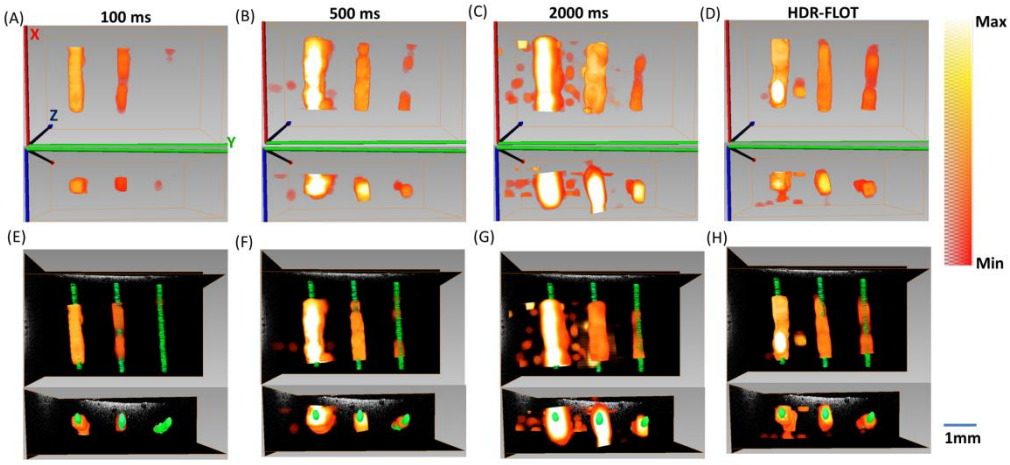

Figure 7. 3D FLOT reconstructed images in the agar phantom with $\mu_s' = 1.2$/mm at 635 nm.

(A-C) 3D FLOT reconstructed images with exposure times of 100 ms, 500 ms, and 2000 ms. (D) 3D HDR-FLOT reconstructed image. (E-H) Co-registered 3D FLOT reconstructed images with corresponding OCT images (green). The Max in the colormap is the maximum value in the image and Min represents the value: (Background + (Max-Background)/2).

In another phantom with a reduced scattering coefficient of ~1.2 mm^{-1}, similar to the previous case, only parts of C3 can stand out from the background with 100 ms

and 500 ms exposure, as shown in Fig. 7(A) and (B). Although increasing the exposure time will enhance the SNR of this capillary, the shapes of C1 and C2 become distorted because overexposure and noise become more obvious for 2000 ms [Fig. 7(C)]. With 2D HDR fluorescence images, the 3D reconstructed image can resolve all three capillaries with different concentrations of Cy 5.5 simultaneously [Fig. 7(D)]. Because of the increased scattering, there are more noises in the reconstructed 3D images and the constructed capillaries appear larger in diameter (more distortion).

3.3.3 Oblique glass capillary in living mouse brain

Fig. 8(A) shows the 150-μm capillary in a mouse brain *in vivo*. The upper row in Fig. 8(B) shows the 3D FLOT-reconstructed images with exposure times of 100 ms, 500 ms, 2000 ms, and HDR-mode. The reconstructed image using 500 ms exposure time has a clear increase in depth than that using 100 ms exposure time, as a longer exposure time will enhance the signals at deeper regions that have a lower SNR. On the other hand, we can also notice that there is more noise at shallower areas using an exposure time of 500 ms, as a higher exposure time will saturate the sample and increase the noise in the shallow areas. The saturation and noise become more obvious when using an exposure time of 2000 ms, resulting in the shape of the capillary being hardly distinguishable at the shallow areas. However, as indicated by the red arrow in the image, the capillary in the deeper area is displayed clearly, indicating that a higher exposure time overexposes the detectors closer to the illumination source, while enhancing the signals collected by the detectors farther away from the illumination source. In comparison, the capillary reconstructed by

HDR-FLOT has a relatively deep penetration with a relatively low noise level at the shallow areas. The bottom row of Fig. 8(B) shows the reconstructed 3D FLOT images superimposed with the 3D OCT images (labelled in green). We define the reconstructed depth as the vertical length of the obliquely inserted capillary in the mouse brain under the preset threshold, which indicates the limitation of the depth that FLOT can reconstruct in the mouse brain. Fig. 8(C) shows the quantitative penetration depth using different exposure times. With an exposure time of 100 ms, the reconstructed depth of the capillary can reach around 550 μm and up to around 800 μm with an exposure time of 500 ms. Our HDR-FLOT method presents a ~1 mm depth, more than 20% deeper than that at 500 ms. Although the reconstructed depth of the capillary reaches deepest (1.2 mm) with an exposure time of 2000 ms, it is not practical since the 3D shape of the capillary is distorted too much at the shallower regions. We further evaluated the DDR as a function of depth for each of the exposure times and the HDR image in Fig. 8(D). In the shallow range (within 400 μm), 100 ms provides the best DDR. HDR and 500 ms exposure time give similar DDRs while HDR has a deeper penetration depth. Further increasing the exposure time to 2000 ms results in a better DDR at deeper range (>700 μm) and larger penetration depth, while the signal cannot be distinguished from noises in the shallow range because of saturation.

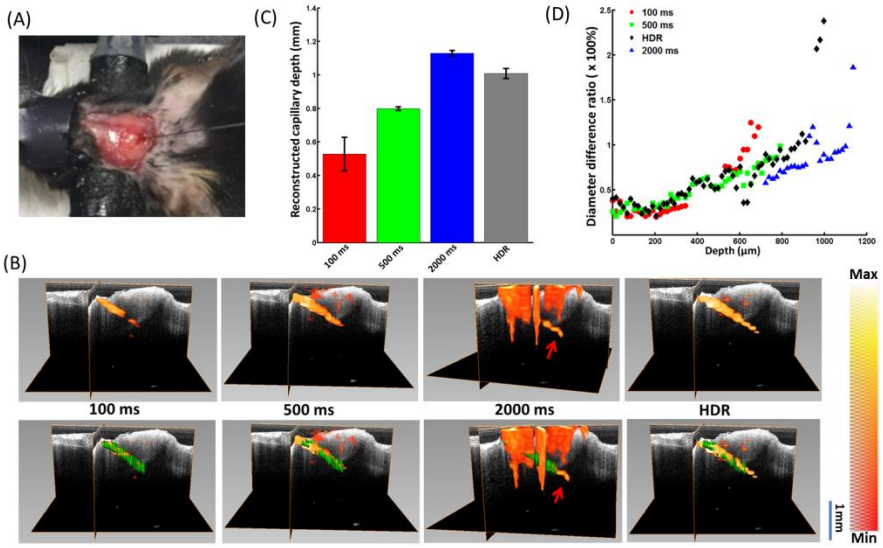

Figure 8. 3-D living mouse brain data

(A) Photo of a 150-μm capillary in the mouse brain *in vivo*. (B) 3D FLOT reconstructed oblique capillary with exposure times of 100 ms, 500 ms, and 2000 ms, and HDR-FLOT. (C) Capillary depths in mouse brain from FLOT with exposure times of 100 ms, 500 ms, and 2000 ms and HDR-FLOT (n=5). (D) Diameter difference ratios for FLOT with different exposure times as a function of depth compared to OCT data. The Max in the colormap is the maximum value in the image and Min represents the value: (Background + (Max-Background)/2).

3.4 Conclusion

In this paper, by combining the commonly used multi-exposure-based HDR method, we presented HDR-FLOT. We first imaged a phantom with three 150-μm capillaries filled with different concentrations of Cy 5.5 solution to demonstrate the feasibility of HDR-FLOT in imaging samples with large concentration differences. Then, we imaged a mouse brain *in vivo* with an oblique capillary inserted to show the improved penetration depth of HDR-FLOT for brain imaging. Our data indicate that HDR-FLOT has increased the detection dynamic range, allowing it to resolve samples with large concentration differences simultaneously in the same ROI, and the reconstructed 3D data are more quantitatively accurate. HDR-FLOT can also increase

imaging depth by more than 20% compared to conventional FLOT in a mouse brain *in vivo*.

Depth-resolved LOT/FLOT has been demonstrated in imaging tumors/fluorescence-labeled tumors [100, 102, 103, 159], perfused rat hearts [93], and fluorescence-labeled cells in tissue engineering [98, 99], as well as for visualizing neural activities in mouse brain and spinal cord [80, 95, 179]. In a realistic experiment, usually we do not know the fluorescence situation/distribution of the sample, which means that it is difficult to choose a proper excitation power or exposure time for the unknown inhomogeneous fluorescence distribution. By employing the HDR-FLOT, samples with large concentration differences can be resolved simultaneously in the same ROI, and in a more quantitatively accurate way. Since light attenuation is exponential in biological tissues, while SNR gain with integration time grows with the square root of the integration time, HDR-FLOT may provide only limited improvement in penetration depth. However, in biological studies, small increases in penetration depth will add confidence to the result and may provide more information. For example, with more than a 20% depth increase compared to conventional FLOT in a mouse brain *in vivo*, we may be able to image the entire six layers in the mouse cortex with HDR-FLOT compared to four layers. Hemodynamic response usually occurs in seconds; therefore, the LOT system with ~40 frames/s imaging speed can be used to study hemodynamic responses [19, 95]. Use of exogenous fluorescent dyes and transgenic animals can also aid in studying functional parameters, such as changes in membrane potential [voltage-sensitive dyes (VSD)] or ion concentrations (pH-, calcium-, chloride-, or potassium-sensitive dyes) [5, 19]. The time-resolved acquisition

protocol to record the fast neural dynamics, which requires the biological response to be repeatable for each stimulation trial [19], was investigated for FLOT [19, 80, 93]. The HDR-FLOT presented in this paper can be incorporated with a time-resolved acquisition protocol to provide a potentially improved mesoscopic imaging method to image neuronal activities for functional brain mapping. In future, we can shorten each exposure time by increasing the excitation power and reducing the quantity of the exposure times, using two or three exposure times instead of the five, as used in this paper, to accelerate overall data acquisition time.

Chapter 4: *In Vivo* Mesoscopic Voltage-Sensitive Dye Imaging of Brain Activation*

4.1 Introduction

Sensory pathways in the mammalian brain have been particular targets of imaging studies, because neural networks can be evaluated following specific stimulation of the sense organs, which translate, and transmit physical energy to the brain. One such sensory pathway, highly amenable to experimental manipulations, is the rodent whisker-barrel system[173]. Whisker-specific sensory afferents and their postsynaptic partners form discrete physical representations in the brainstem, thalamus and neocortex [180]. Thus, point-to-point and topographic representation of the activation of the sensory periphery in the brain can be evaluated with electrophysiological and imaging approaches [80].

Fig. 1 shows schematic of the whisker-to-barrel pathway. Sensory information from the whisker on the mouse snout first transmits from trigeminal nerve to the trigeminal nucleus, then to the ventrobasal thalamus and finally to the barrel field in layer IV of somatosensory cortex. Interestingly, the patterned distribution of whiskers

* The contents in this chapter is reproduced from "Tang, Q. et al. *In Vivo* Mesoscopic Voltage-Sensitive Dye Imaging of Brain Activation. *Sci. Rep*. 6, 25269 (2016)" with permission.

on the snout is replicated at all the three presynaptic afferent terminals (the brainstem, thalamus and cortex). These cellular patterns are named "barrelettes" in the brain stem, "barreloids" in the thalamus and "barrels" in the cortex by the neuroscientists, respectively [181]. Generally speaking, stimulation of a single whisker (air puff or mechanical shaking) will evoke neural responses/activities in its corresponding barrelette, barreloid, and then barrel [173]. The barrel fields have been studied intensively with a variety of imaging approaches due to their ease of access, identification and close to surface location[173, 182-185]. However, functional mapping of the subcortical brain was technically challenging and limited due to their deep locations in the brain[173, 186].

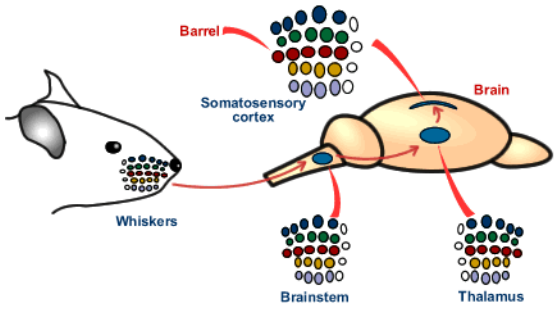

Figure 1. Schematic of the whisker-to-barrel pathway [187].

Voltage-sensitive dye imaging (VSDi) has been quite useful in imaging activities of the neural networks in the brain [5]. VSDi is based on fluorophore molecules that bind to the neural membrane and convert changes in transmembrane voltage into the fluorescence of the emitted light [5]. VSDi creates an opportunity to monitor neural activity *in vivo* with relatively high spatial and temporal resolution (up to microseconds). However, VSDi, being a variety of the wide field optical imaging

technique, cannot allow visualization of neural activity in three dimensions.

Mesoscopic imaging has been developed in recent years, including mesoscopic epifluorescence tomography[188, 189], and fluorescence laminar optical tomography (FLOT) [108, 109, 190]. An array detector with different separations from the light source is used in FLOT, which enables simultaneous detection of scattered light from different depths. FLOT can achieve an axial resolution of ~100-200 microns with several millimeter imaging depth [111], and has been extended to time-resolved imaging in the perfused rat heart with voltage-sensitive dyes (VSDs) to obtain 3-dimensional (3D) propagation of electrical waves [108]. Recent studies indicate that angled illumination and detection configurations can improve both resolution and depth sensitivity [112].

In this paper, combining aFLOT with VSDs, we present 3D neural activities evoked in the whisker barrel cortex of mice by deflection of a single whisker *in vivo* with 5 ms temporal resolution (e.g., an effective frame rate of 200 Hz). Further, our results lend support to the hypothesis that a 3D dynamic activity patterns, represent neural network processing in different parts of the cerebral cortex.

4.2 Methods

All experiments were performed in accordance with the National Institutes of Health Guide for the Care and Use of Laboratory Animals (NIH Publication No.80-23) and a protocol approved by the Institutional Animal Care and Use Committee of the University of Maryland, Baltimore and College Park campuses.

4.2.1 Animal preparation

Experiments were performed on five B6 mice at 2-3 months of age. Animals were anesthetized with urethane (1.15 g/kg body weight). Their heads were shaved before placing in a stereotaxic frame (Stoelting Ltd) [191]. A cranial window (about 3x3 mm) was made over the left parietal cortex, and the surface of the dura matter was cleaned with hemostatic sponge dipped in artificial cerebrospinal fluid (ACSF). Voltage-sensitive dye RH-1691 (Optical Imaging Ltd; 1.0 mg/ml in ACSF) was applied to the exposed area for 45 min [191]. After staining, the cortex was washed with dye-free ACSF for 15 min and the cortical surface was covered with high-density silicone oil and then sealed with a 0.1-mm-thick cover glass. A glass pipe (1.0 mm in diameter) fitted onto an XYZ manipulator was aimed at the facial C2 whisker. An air-puff stimulus of a 20 ms duration was applied through a Picospritzer pressure valve connected to the glass pipette [191].In the electrode stimulation experiments, a bipolar tungsten electrode (containing two electrodes) (FHC Ltd, Bowdoin, US) was inserted into the brain by using a micromanipulator (Narishige, Japan). Electrical currents were applied through both electrodes. The stimulation system was coupled to the computer of the imaging system.

4.2.2 Experimental setup

Fig. 2(A) shows the schematic diagram of the aFLOT system. A 637 nm laser diode was utilized as the light source; the light was collimated and coupled into a single-mode fiber to shape the light beam. Light coming out from the fiber was first collimated by an objective lens and passed through a polarizer, which was used to reject the specular reflection from the surface. The collimated light was expanded into line-field illumination using a cylindrical

lens with a full line-width at the half maximum of 26 μm at the focal plane. An iris was used to control the length of the line illumination. The emitted fluorescent light was then collected back through the objective lens, dichroic mirror (650 nm, single edge dichroic beam splitter; FF650-DiO1-50×70 mm; Andover Corporation), emission filter (695 nm, 695FG07-50, Andover Corporation), and finally imaged to a high-speed CCD camera (MiCAM02-HR, SciMedia, Ltd). The laser diode and emission filter used for quantum dots were 649 nm and 705 nm respectively. The illumination angle was set at 45°, rendering ~30° transmission angle in tissue (n~1.33). The CCD camera was placed vertically to record both fluorescence and reflectance images by changing the filter. The reduced scattering coefficient (μ_s') of the sample was determined from the reflectance data using oblique-incidence spectroscopy [192]. A motor stage was used to translate the sample laterally in scanning direction (perpendicular to the line illumination direction). OCT can provide depth-resolved cross-sectional images of tissue microstructures with micrometer resolution [43, 193]. In the glass capillary and electrode experiments, the living mouse brain was first scanned with the OCT system to get 3D images, which provided the structure information of the mouse brain. The 3D images can also indicate the shape and tip location of the glass capillary and electrodes which served as the reference for the following results from aFLOT experiments in the same mouse brain. The OCT system used here utilized a wavelength-swept laser source (Thorlabs, Inc.), which generated a broadband spectrum of 100 nm FWHM centered at 1310 nm, and has been described previously [64, 94].

4.2.3 Stimuli and data acquisition

For 3D reconstruction of the 100 μm glass capillary in the mouse brain, since the fluorescence signal is static (i.e., no time-dependent information), only one image at each scanning position was needed [190]. The CCD pixel size was 23 μm. In order to scan a long enough (~2.7 mm) area in scanning direction and save the overall data recording time, 46 μm was chosen as the step size. Typical scanning protocol was 60 steps with a step size of 46 μm, which equaled to ~2.7 mm total movement in scanning direction. The raw measurement for glass capillary imaging had the format of XYS_j (where X and Y represent the X and Y dimensions of the 2D image acquired by CCD, S represented the different scanning position, X=184; Y=128; j=1, …, 60). Since the optical properties were different in the air versus brain, in order to compare the theoretical model with experimental data as precisely as possible, the brain surface must be found. To obtain the surface tomography of the mouse brain, the emission filter was removed and the same FOV was scanned to get the reflectance images with the same scanning step size. Without the emission filter, most of the collected light was from the reflection of the illumination light at the brain surface, which would then serve as an indicator of the location of the brain surface. The raw measurement of reflectance mode had exactly the same format of XYS_j (X=184; Y=128; j=1, …, 60). The image acquisition protocol for time-resolved aFLOT is shown in Fig. 2(B). The illumination line was first focused on the border of the desired field of view (FOV). At each scanning position, an experimental session consisting of 30 trials, with 200 frames per trial and 5 ms/frame was finished. In each trial, the stimulus (the train of square electrical pulses, 100 μA, 0.3 ms, 300 Hz, 10 ms train duration) or 20 ms whisker deflection was presented at the 100^{th} frame (one stimulus per trial). The images from these 30 trials were averaged to obtain the response

XYT_iS_0 (where X=184; Y=128; i=1, …, 200). Next, the motor stage moved 46 μm in scanning direction to another illumination/collection area and another experimental session was performed to obtain the next dataset XYT_iS_1 (where X=184; Y=128; i=1, …, 200). This process was repeated until finishing the entire FOV scanning. The raw measurement had the format of XYT_iS_j (where X=184; Y=128; i=1, …, 200; j=1, …, 60) for electrodes and whisker imaging. Finally, because of defocus effect, we set the focus plane slightly below the dural surface.

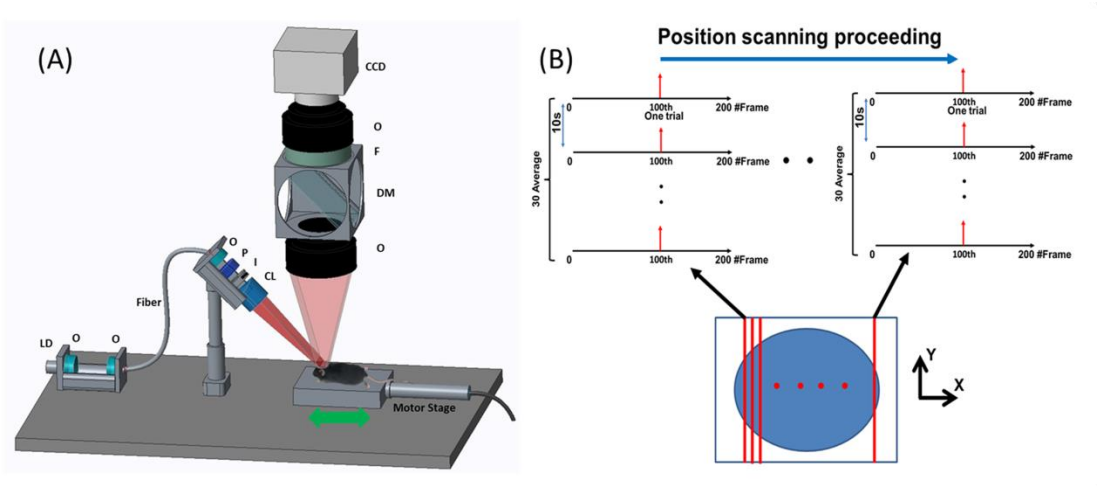

Figure 2. Schematic of the aFLOT system and Image acquisition protocol
(A) Schematic of the aFLOT system. LD: laser diode; O: objective lens; P: polarizer; I: iris; CL: cylindrical lens; F: filter; DM: dichroic mirror. CCD is for capturing both laminar fluorescence and reflective light distribution (by removing F). The illumination arm is arranged at 45° in air. (B) Image acquisition protocol.

4.2.4 Data reconstruction and analysis

The raw measurements of the reflectance data were simply stacked, according to the geometrical relationship between the illumination plane and detection FOV, which was similar to the unprocessed stacked raw images in selective-plane illumination microscopy [176]. Additionally, for the experiment of glass capillary and electrodes, the stacked reflectance data were used to co-register with the OCT data based on the shape / structure /

insertion feature of the glass capillary and electrodes. To reconstruct the 3D fluorescence distribution, the first step was to match the step size and the pixel size; interpolation was then done only in the scanning dimension changing the raw dataset from XYS_j (X=184; Y=128; j=1, …, 60) to XYS_j (where X=184; Y=128; j=1, …, 120) for glass capillary imaging using a custom MATLAB algorithm. To reconstruct the images, we assumed first-order Born approximation to obtain linearity between the measurement F and the fluorophore distribution C, which is the FOV_{XZ} to be reconstructed. This linear relationship is written as $F = JC$,where J is the weight or sensitivity matrix. To constitute J, photon distribution was first generated by Monte-Carlo simulation (g=0.9, n=1.33, μ_a=0.01/mm, μ_s'=0.82/mm) [137]. Then we applied the reciprocity principle. J was later decomposed by singular value decomposition (SVD) [177]. Lastly, least square fitting and Tikhonov regularization [112] were used to solve the underdetermined system [112]. The regularization parameter α=0.0016 was determined by L-curve criterion[178]. 100 source-detector pairs and 100 scanning positions were chosen to constitute 10,000 measurement modes. Each reconstructed FOV_{XZ} was 100x100 pixels with a pixel size of ~23 μm. Weight matrix J is therefore of size 10000×10000. FOV_{XYZ} was constituted by superimposing individual FOV_{XZ} in Y direction. Since the reflectance images and fluorescence images have exactly the same format, the reflectance images, which can indicate the location of the brain surface can be used to select the ROI for fluorescence images to perform reconstruction using our custom MATLAB algorithm. For the time-resolved aFLOT experiment in electrodes and whisker stimulation, since fluorophore intensity changes were used to indicate the activated area in VSDi, the original fluorophore intensity needed to be calculated first. For each XYT dataset at each scanning position, the final ten pre-stimulus frames (90-99th

frame) were averaged as the baseline image. The baseline image was then subtracted from each subsequent frame to obtain changes in fluorescence signals. The next step was to match the step size and pixel size; interpolation was then done only in the scanning dimension changing the raw dataset to XYT_iS_j (where X=184; Y=128; i=1, …, 200; j=1, …, 120) for electrodes and whisker imaging using a custom MATLAB algorithm. The images at different scanning positions with the same frame number were rearranged as one data set (e.g. the dataset for 1st frame of the trial at all scanning positions was XYT_1S_j (where X=184; Y=128; j=1, …, 120)). This reconstruction process was repeated for all time points (from 1st to 200th frame) to obtain the entire time course of 3D neural responses.

4.3 Results

4.3.1 3D characterization of the aFLOT system

We used quantum-dot-embedded hydrogel to characterize the point spread function (PSF) of our aFLOT system. Recipe of this phantom was 35 μL QD705 (QD705, Invitrogen), 1.5mL poly(ethylene glycol) diacrylate (PEGDA), 3.5mL water, 1mL ammonium persulfate (APS) (0.2M), and 1mL N,N,N',N'-tetramethylethylenediamine (TEMED) (0.2M). The mixture was vortexed and immediately poured into a well plate as it crosslinked within 30 s. The measured reduced scattering coefficient (μ_s') of the hydrogel was 0.5/mm. For aFLOT imaging, the emission filter was first removed and the field of view (FOV) was scanned to get the reflectance images with the step size 46 μm. Only one image was needed at each scanning position for reconstruction of the static quantum dots (i.e., the fluorescence signal is not time-dependent), thus only one image at each scanning position was

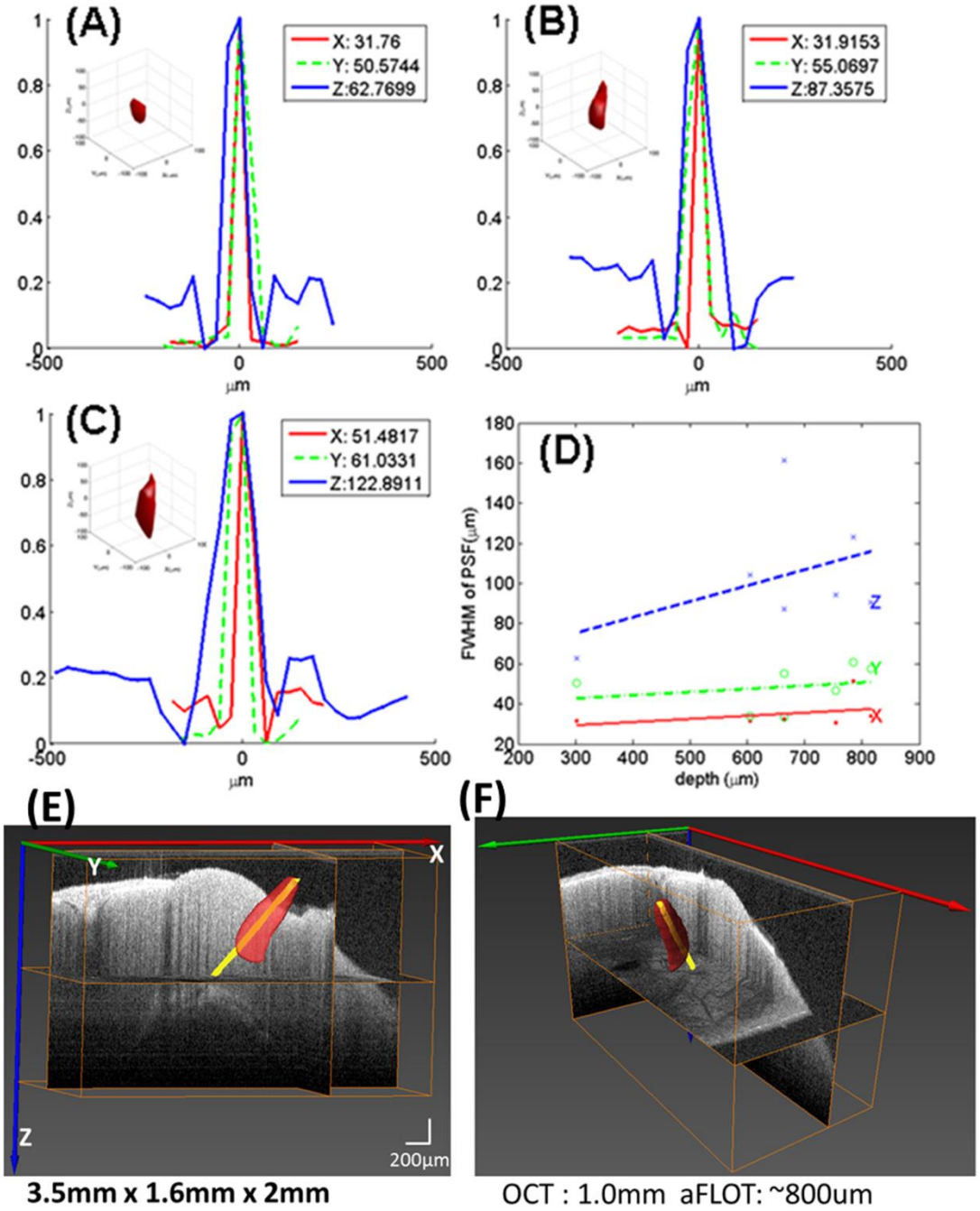

Figure 3. 3D PSFs of the aFLOT system

3D PSFs of the aFLOT system at 302 μm (A), 664 μm (B), and 785 μm (C). Insets show the isosurface of PSFs with μ_s'= 0.5/mm. Legends report FWHM in μm in x, y, and z directions. (D) FWHM versus depths. •, ○, and × represent respectively the FWHM in x, y, and z directions of a single PSF at the corresponding depth. (E,F) Reconstructed 3D aFLOT fluorescence images of 100 μm glass capillary tube superimposed with OCT data.

acquired after adding the emission filter [94]. Fig. 3(A-C) show 3 PSFs of the quantum dots at depths of 302, 664, and 785 µm, respectively. Full width at half maximum (FWHM) in x, y, and z directions mildly increases toward deeper depths (Fig. 3(D)). Pixelation of PSF was observed. This however suggests that true PSF would be slightly smaller than the values reported here. We observed an increasing trend for axial PSF with depth, reaching ~120 µm at 800 µm depth. Furthermore, we also observed in general, PSF in y direction is larger than x direction, which is due to the asymmetric illumination between x and y direction.

4.3.2 3D reconstruction of 100 µm glass capillary in mouse brain

Since the optical properties of the living mouse brain is complicated, it is difficult to make a phantom to simulate this sophisticated biological machinery. Therefore we carried out an experiment using a 100µm glass tube to verify the performance of the aFLOT system in the living mouse brain. The 100µm glass capillary tube (ID: 0.1mm, OD: 0.17mm, Vitrocom Inc.) was filled with VSD and fixed on a 3D manipulator. The capillary was then inserted into a mouse brain, which was handled through the animal preparation protocol except dye loading. In this experiment, we first used OCT to scan the glass capillary tube in the brain. Then the mouse brain with the capillary tube was used for the aFLOT experiment. For aFLOT imaging, the emission filter was first removed and the field of view (FOV) was scanned to get the reflectance images with the step size 46 µm. Only one image was needed at each scanning position for reflectance mode. To record the fluorescence images for capillary, we intended to obtain 3D reconstruction of the static capillary structure (i.e., the fluorescence signal is not time-dependent), thus only one image at each scanning position was acquired after adding the emission filter [94]. The reflectance

images of the FOV ware used to reconstruct the surface feature, which was used to align the 3D OCT data with the 3D aFLOT fluorescence data. Fig. 3(E, F) shows different perspectives of the reconstructed 3D aFLOT fluorescence images superposed with the optical coherence tomography (OCT) data. OCT can provide information about the brain structure and depth. The yellow object in the 3D OCT image is the capillary recorded by OCT and the red one is the aFLOT reconstructed capillary tube. OCT can image around 1 mm deep in the living mouse brain while aFLOT around 800 μm in depth, without major image distortion; barrels are about 300-500 μm deep from the pial surface in adult mice.

4.3.3 Time-resolved 3D reconstruction of electrode stimulation in the mouse brain

We verified the overall process for 3D functional imaging using a pair of electrodes. The electrodes were first fixed on a 3D manipulator, and then the electrodes were inserted into the mouse brain. Similar to the capillary tube experiment, we first used OCT to get the 3D electrode image in the brain and then used aFLOT to image the mouse brain with the electrodes. For aFLOT imaging, the emission filter was first removed and the FOV was scanned to get the reflectance images with the step size of 46 μm, with only one image at each scanning position used for the reflectance mode. Then the emission filter was applied, and based on the data acquisition protocol for time-resolved aFLOT imaging (described in the Methods section), the fluorescence images were recorded. The reflectance image of the FOV was used to reconstruct the surface features, which were used to align the 3D OCT data with the 3D aFLOT fluorescence data. Fig. 4 shows the electrodes reconstructed with 3D aFLOT in the

fluorescence images superposed with OCT data. OCT shows that the electrode tips are at around 440 μm depth from the cortical surface. The two green rods in the 3D OCT image are the electrodes recorded by OCT and the orange ones are the aFLOT-reconstructed changes in fluorescence (ΔF/F(%), ordinate) in response to electrical stimulation at different time points. The signal appeared about 15 ms after the stimulus onset, and reached peak at 25 ms after the stimulus onset. At time 30 ms and 35 ms we can clearly see a pair of signals surrounding the two electrode tips, which indicate that aFLOT system and imaging protocol can be used to record 3D functional images. The activated signals disappeared gradually, after 40 ms.

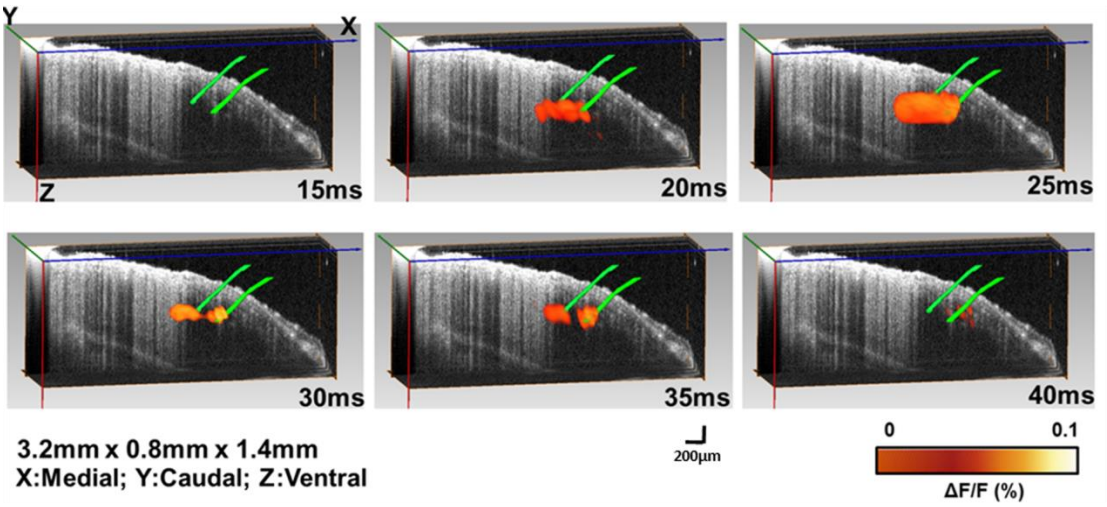

Figure 4. 3D aFLOT images to electrical stimulation
3D changes in fluorescence (ΔF/F(%), ordinate) in response to electrical stimulation reconstructed by aFLOT system superimposed with OCT data. Time period after stimulation is indicated at the bottom right corner of each image.

4.3.4 Time-resolved 3D reconstruction of cortical neural activity evoked by single whisker deflection

After verifying the imaging ability of the aFLOT system, for both structure and function, aFLOT was used to record 3D neural activities evoked in the barrel cortex

by deflection of a single whisker *in vivo*. The C2 whisker was used for 20 ms stimulation. Fig. 5 shows the 3D aFLOT reconstructed changes in fluorescence (ΔF/F(%), ordinate) in response to C2 whisker stimulation at different time points. The signal appeared about 30 ms after the stimulus onset, and reached its peak at 50 ms after the stimulus onset. After 70 ms, the activated signals disappeared gradually. The time course corresponds well with the previously published data [175]. Fig. 6(A) shows the change in fluorescence (ΔF/F(%), ordinate) in response to the C2 whisker stimulation. Fluorescence signal was calculated from the region of interest (ROI, green cubic box: 3x3x3 pixels) shown in Fig. 5 at 50 ms post-stimulation. Fig. 6(B) shows coordinates of the largest changes in fluorescence (ΔF/F(%), ordinate) in response to the C2 whisker stimulation. Fig. 6(B) shows that the signal center was at around 500 μm below the cortical surface at 30-45 ms and then moved to around 440 μm below the cortical surface at 50 and 55 ms. Finally, the center of the signal moved to around 380μm below the cortical surface.

To better visualize the depth-resolved neural activity, changes in fluorescence (ΔF/F(%), ordinate) in response to the C2 whisker stimulation were reconstructed by aFLOT in different depths (XY cross-sections) as shown in Fig. 7. The changes in fluorescence first took place in the range 380-520 μm at about 35-40 ms, then the response became stronger in both deeper (680 μm) and shallower region (300 μm and 380 μm) at around 50 ms and 55 ms. Although the signal response trend existed at depth of 300 μm and 680 μm,

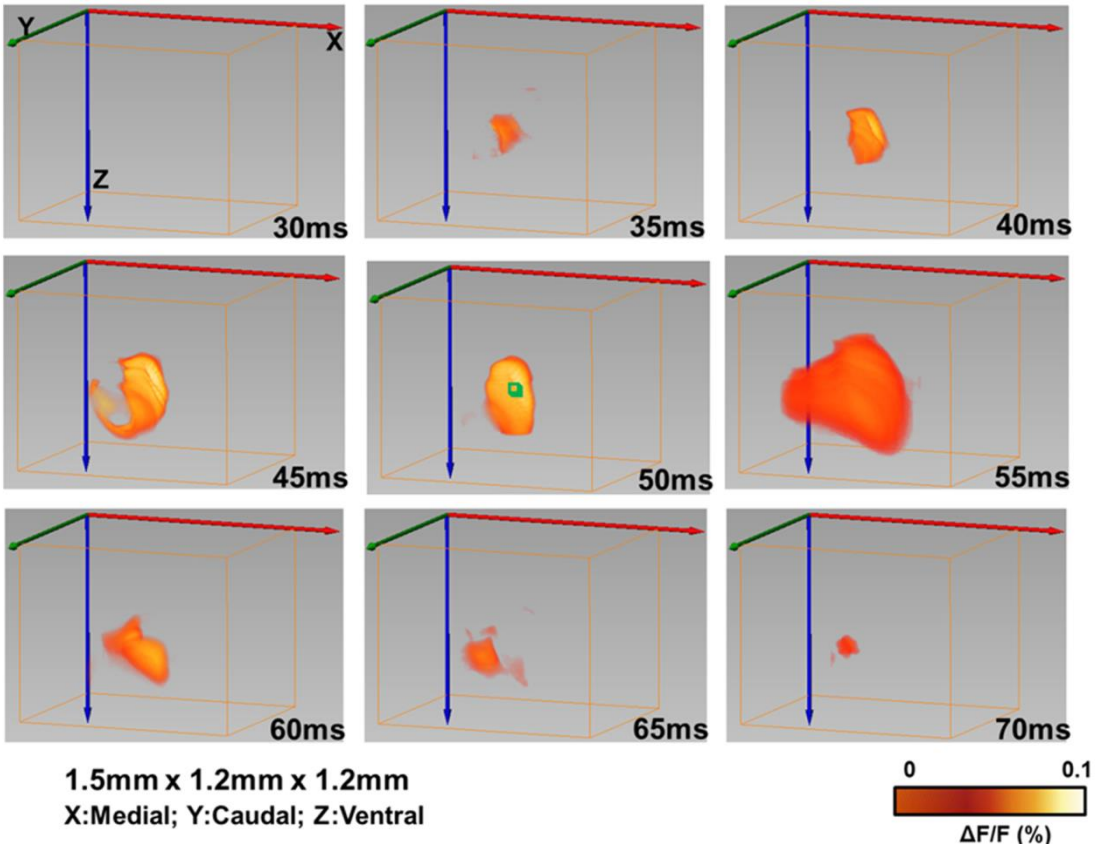

Figure 5. 3D aFLOT images to C2 whisker stimulation

3D changes in fluorescece (ΔF/F(%), ordinate) in response to the C2 whisker stimulation reconstructed by the aFLOT system. Time period after stimulation is indicated at the bottom right corner of each image.

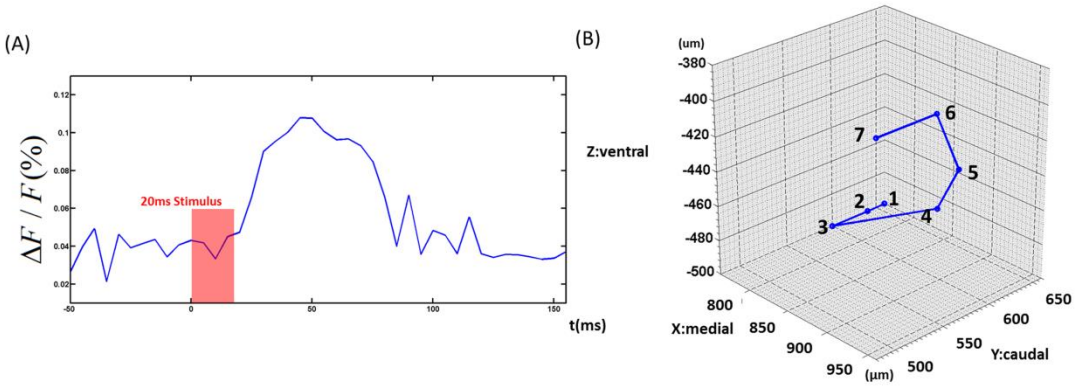

Figure 6. C2 whisker response analysis

(A) Change in fluorescence (ΔF/F(%), ordinate) in response to the C2 whisker stimulation. Fluorescence signal was calculated from the ROI (green cubic box: 3x3x3 pixels) shown in Figure 5 at 50ms post-stimulation. (B) Coordinates of the strongest change in fluorescence (ΔF/F(%), ordinate) in response to the C2 whisker stimulation. 1: 30ms and 35ms (760μm,660μm, -500μm); 2: 40ms (760μm,640μm,-500μm); 3: 45ms (760μm,600μm,-500μm); 4: 50ms (940μm, 560μm,-440μm); 5: 55ms (900μm,620μm,-440μm); 6: 60ms and 65 ms (960μm, 540μm,-380μm); 7: 70ms (960μm,480μm,-380μm).

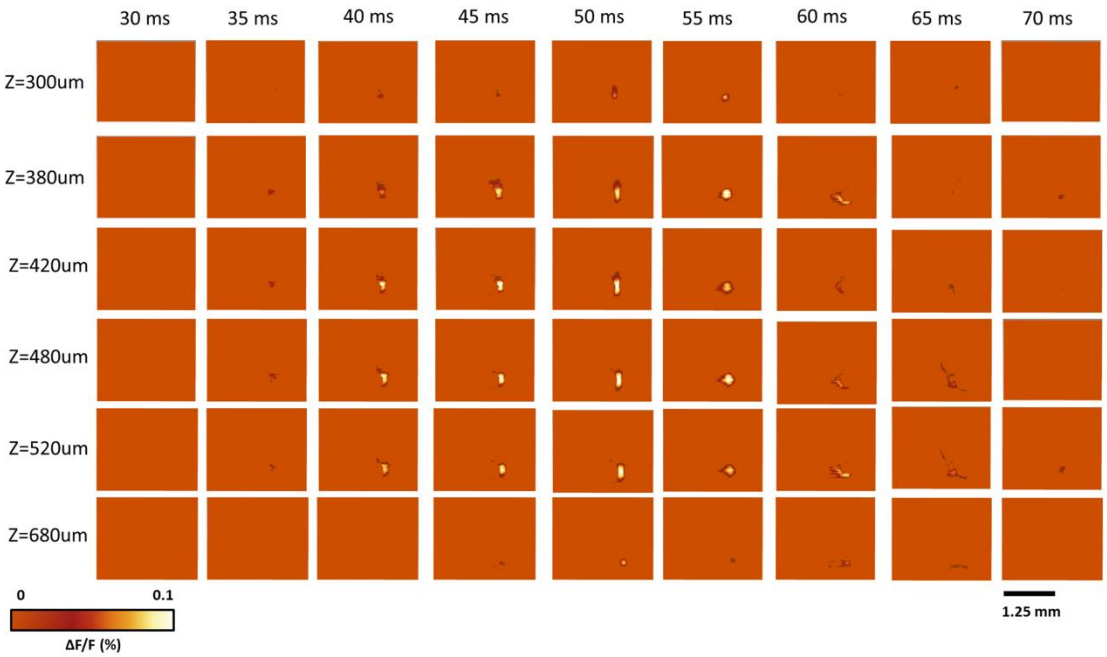

Figure 7. aFLOT images to C2 whisker stimulation at different depths

Changes in fluorescence (ΔF/F(%), ordinate) in response to the C2 whisker stimulation reconstructed by the aFLOT system in different depths. Time period after stimulation is indicated at the top of the whole image. The left column shows the depth information.

the average response intensity was weaker compared to the other depths, which may be caused by the difference of neuronal density at different depths or in layers. Also, we observed that the neural responses in the 420-520 μm range lasted longer than in other depths.

Fig. 8(A) shows changes in the fluorescence (ΔF/F(%), ordinate) in response to C2 whisker stimulation reconstructed by aFLOT in the XZ cross-section. Fig. 8(B) shows the change in fluorescence (ΔF/F(%), ordinate) intensity in response to C2 whisker stimulation, in the middle XZ cross-section. The fluorescence signal was calculated from the ROI (green square: 3x3 pixels) shown in Fig. 8(A) at 50 ms post-stimulation. Compared to neural responses in XY plane, XZ cross-section provides us with a new perspective to investigate the neural activities at different time points.

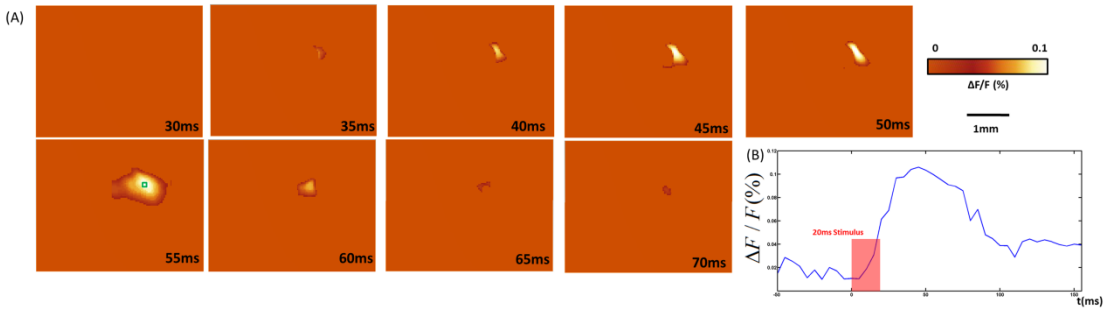

Figure 8. aFLOT images to C2 whisker stimulation at XZ cross-section
(A) Changes in fluorescence (ΔF/F(%), ordinate) in response to C2 whisker stimulation reconstructed by aFLOT system in XZ cross-section. Time period after stimulation is indicated at the bottom right corner of each image. (B) Change in fluorescence (ΔF/F(%), ordinate) in response to the C2 whisker stimulation. Fluorescence signal was calculated from the ROI (green square: 3x3 pixels) shown in Figure 8 (A) at 55ms post-stimulation.

4.4 Discussion

Development of VSDi and other 3D imaging techniques enable examination of spatiotemporal patterns of neuronal activities in the brain. We have demonstrated that it is possible to detect the 3D neural activities by deflection of a single whisker using non-contact optical measurements of the mouse brain *in vivo*.

Time-resolved FLOT has been used in the perfused rat heart with VSDs to obtain 3-dimensional (3D) propagation of electrical waves [108]. In this study, we applied time-resolved FLOT but with angled illumination configuration and CCD camera as detectors which promise to improve both resolution and penetration depth [112]. We have demonstrated the 3D imaging capabilities of our aFLOT system using a quantum-dot-embedded hydrogel. Since the resolution and penetration depth depend on the optical properties of sample, an ideal sample to test the feasibility of the aFLOT system would be a living mouse brain. As illustrated in Fig. 3(E, F), the reconstructed 100 μm glass capillary tube by aFLOT was compared with the image acquired by OCT. The accuracy and resolution of aFLOT degrade with depth. We can observe the reconstruction distortion was within ±120 μm up to 800 μm depth, which definitely covered the Layer IV in mouse somatosensory cortex. Performance

of our aFLOT system is quite remarkable, despite limitations, and future work will incorporate the newer NIR and red-shifted VSDs to achieve significantly improved penetration of light into the mouse brain.

In addition to the 3D static system performance evaluation, we observed a rapid response to direct electrical stimulation through the use of a bipolar electrode in the living mouse brain. A study of the intracortical microsimulation provided insight into the spatial extent of the excited neural tissue and its relationship to the exciting current [194]. The threshold gradient across neurons ($\Delta V / \Delta r$) is constant and is related to the applied current as: $\frac{\Delta V}{\Delta \gamma} = \frac{dV}{d\gamma} = \frac{is}{4\pi\gamma^2} = C$, where i is the applied current, s is the specific resistivity of the tissue, and γ is the distance from the current source to the neuron[194]. Thus, the relationship between a particular neuron's threshold current and the neuron's distance from the tip of the stimulating electrode can be expressed as: $i = K\gamma^2$, in which $K = 4C\pi/s$. For mammalian brain tissue, the K has a value of ~1200 μA/mm^2 [194]. Thus, if the stimulation current is 100 μA, more than half of the neurons will be excited in the sphere with a radius of 288 μm from the tip of the electrode [174, 194]. These computations do not take into account the frequency of the stimulation, as well as K having the possibility of being slightly different in different brain tissues. They also do not take into account the influence of pulse duration on the neural excitation and the level of the threshold used for analysis. Nevertheless the computation is generally correct as can be seen in Fig. 4 (the size of the changes in fluorescence at 25ms). Since bipolar electrode consists of two metal needles, isolated at all longevity except the tips, there are two metal tips in the brain and both stimulated the brain tissues simultaneously. The size of the fluorescence changes at 25 ms was around 1000 μm in length through the direction of the two tips of the electrodes and around 450 μm in z direction. Calculated 288 μm was compared with the distance of

fluorescence border to the needle tip (~250 μm in radius). By comparing the spatial extent of the excited neural tissue with the calculation data mentioned above, we were able to evaluate the likely accuracy of our 3D imaging performance.

The voltage-sensitive dye spread along the mediolateral and dorsoventral axes of the neocortex. It was shown that the voltage-sensitive dye RH-1691 loading extended across all cortical layers, but the dye concentration in deep layers (V–VI) is lower[191, 195]. Neurons within layer IV directly respond for whisker movement, in other words, many neurons of this layer will fire when the whisker is mechanically stimulated. The strongest inputs from the thalamus carrying information from a facial whisker to the barrels of layer IV, but the inputs from the thalamus to the layers III, V and VI also exist [195]. Excitatory signals from the thalamus reach different layers of the barrel cortex at different times. From Fig. 6 we can observe the neural responses in the range 420-520 μm which represents the layer IV last longer and have stronger than other depths (shallower and deeper depths). The weaker response in deeper layers (V–VI) may originate from both less neurons corresponding to whisker movement and also less dye concentration. The intensity of the responses at different depths can be more intuitionally visualized in XZ cross-section in Fig. 7(A) at 55ms.

Also we can see that in Fig. 5, the VSDi activity patterns in the cortical area evoked by stimulating a single whisker is larger than the corresponding barrel [196, 197]. The larger response size than barrel in our experiment may also partially caused by the resolution of our reconstruction.

An important question in sensory information processing is how sensory information is represented and processed in the neocortex. The manner by which sensory-evoked neural activity propagates across cortical layers remains unclear[198] . During the last few decades,

propagating waves have been observed during different types of cortical processing as revealed by imaging or electrophysiological methods [199]. The spiral-like waves, as well as more complex activity patterns have been visualized by VSDi *in vivo* in the turtle visual cortex [200].

In our experiment, by localizing the coordinates of largest fluorescence signals at different time point, we were able to show the progress of sensory activity in the neocortex. As shown in Fig. 6(B), we can see the movement of the activated area in both horizontal and vertical directions. The movements of signal centers at different time points are particular kind of propagating waves that rotate around a center point. Although the resolution of our aFLOT system is not high enough to demonstrate the propagating wave, for the first time we demonstrated the propagating trajectory in 3D manner and our data agrees with the electrophysiological data recently obtained using multi-electrode arrays [198] . Future work will focus on further improving the resolution of our aFLOT system.

Chapter 5: Mesoscopic Fluorescence Tomography for Imaging Bone Engineered Tissues*

5.1 Introduction

Bone tissue engineering scaffolds act as vehicles for the delivery of progenitor cell populations or support structures for surrounding tissue ingrowth. Scaffold properties often determine the success in an engineered tissue and must be designed for a specific application. In many outcomes, key parameters allow for improved cell migration, proliferation, and vascularization [201]. To improve tissue regeneration and integration, a scaffold should mimic surrounding tissue morphology, structure, and function. This environment should promote cellular interactions and signaling, and as a result, differentiation. One challenge is to comprehensively observe and quantify the distribution, migration, and differentiation of seeded cells throughout the scaffold. Bone tissue engineering could benefit from a precise and noninvasive imaging method to follow cells activity. Such an imaging technology could provide useful information on the interplay of scaffold designs, cells, and chemical/environmental cues to optimize the development of bone grafts.

---

* The contents in this chapter is reproduced from "Tang, Q. et al. Imaging Stem Cell Distribution, Growth, Migration, and Differentiation in 3D Scaffolds for Bone Tissue Engineering using Mesoscopic Fluorescence Tomography. In review" with permission.

Currently, fluorescent confocal microscopy (FCM) is the gold standard method for quantifying 3D cell distribution. FCM can visualize cells and molecules via a wide variety of fluorescence probes and is a powerful technique for molecular imaging. However, FCM has a limited imaging depth of 100 μm [24] . In addition, two-photon microscopy (TPM) has been used to image engineered tissues [24], but is also associated with limited penetration depth of 500 μm [25, 26, 202]. The current state-of-the-art method for quantifying 3D cell distribution, migration, or differentiation involves FCM imaging of cryo-sectioned scaffolds and 3D image recompiling [203]. Although robust, this approach is destructive and time-consuming. To overcome the depth-limitation of confocal microscopy, fluorescence laminar optical tomography (FLOT) or mesoscopic fluorescence molecular tomography (MFMT) has been developed by using an array of photon detectors or a charge coupled device (CCD) camera to collect photons emitted from locations at different distances away from the illumination position, and then reconstructs the depth-resolved images through mathematical deconvolution [40, 92-94, 97-100, 103]. FLOT can provide an axial resolution of 100-200 microns with 2-3 mm penetration depths [19, 80, 91, 93, 111]. FLOT has been recently applied to image tissue engineering scaffolds in 3D [98, 99], quantify depth-resolved distribution of fluorescence-labeled tumors [100, 111], and visualizing neural activities in mouse brains *in vivo* [19, 80]. Recent studies demonstrated that angled illumination or detection modification (termed aFLOT) can improve both resolution and depth sensitivity [19, 80, 112].

Therefore, aFLOT represents a promising novel imaging platform to non-destructively quantify depth-resolved information of cell-scaffold interactions in situ.

The proposed study aims at investigating different applications of aFLOT in bone tissue engineering. First we demonstrated the depth-resolve capability of aFLOT and the ability to quantify cell density inside a scaffold. Then, 3D printed bone osteons were evaluated using aFLOT in order to show its capability in accurately differentiating distinct cell populations. The 3D migration process of cells was also visualized using aFLOT. Finally aFLOT was used to image the mineralization of alginate scaffolds seeded with human mesenchymal stem cells by measuring hydroxyapatite (HA) deposition.

5.2 Materials and methods

5.2.1 Mesoscopic fluorescence tomography

The aFLOT system is similar to that reported previously [80, 167, 204]. Pigtailed 637-nm and 520-nm laser diodes were used as the light sources (LP637-SF70 and LP520-SF15, Thorlabs Inc.) to illuminate the samples at two wavelengths in time-shared manner. A cylindrical lens was used to shape the collimated light into a line-field illumination with a full line-width at the half maximum of ~26 μm at the focal plane [80, 204]. An iris was used to adjust the length of the line illumination. The backscattered light and emitted fluorescent light were collected through an objective lens, a filter wheel (695-nm and 561-nm long-pass emission filters for fluorescence imaging and no filter for reflectance images), and finally onto a 12-bit CCD camera (EM-CCD, Cooke) [80, 204].

5.2.2 Cell culture

Human mesenchymal stem cells (hMSCs) (Lonza, Walkersville, MD) were cultured in control media consisting of DMEM (Gibco, Carlsbad, CA) supplemented with 10% fetal bovine serum (Gibco), 1.0% v/v penicillin/streptomycin (Gibco), 0.1 mM non-essential amino acids (Gibco), and 4 mM L-glutamine (Gibco as per the manufacture's specifications). hMSCs were expanded on tissue culture polystyrene flasks with media changes every 3 days. Prior to the experiment, cells were passaged using trypsin/EDTA (Lonza). L929 cells (ATCC, Manassas, VA) were cultured as per the manufacturer's specifications with Minimum Essential Medium (Life Technologies, Frederick, MD) and 10% horse serum (Life Technologies). Cells were plated and allowed to grow to 80% confluency before initiating the assays.

5.2.3 Sample fabrication and cell seeding

5.2.3.1 Gelatin methacrylate synthesis

Gelatin methacrylate was synthesized according to previously published methods [205]. Type A porcine skin gelatin (Sigma-Aldrich; 300 bloom) was mixed at 10% (w/v) into phosphate buffered saline (PBS; Thermo Fisher Scientific) at 50 °C for 20 min. Methacrylic anhydride (MA, SigmaAldrich) was added at the ratio of 0.6 g MA/g gelatin under rigorous stirring for an hour. The reactants were then diluted 2-fold with PBS to stop the reaction. After centrifugation, the pellet was discarded and the supernatant was dialyzed against deionized water using dialysis cassettes (10 kDa MWCO, Thermo Fisher Scientific) for at least 3 days at 50 °C, to remove salts and

excess methacrylic acid. The dialyzed GelMA was then lyophilized and kept at −80°C for long-term storage. To form samples, gelMA was rehydrated in PBS for 10 min at 50 °C. Photoinitiator (2-hydroxy-1-(4-hydroxyethoxy)phenyl)-2-methyl-1-propanone (BASF) was then added into the GelMA solution at a concentration of 0.5% (w/v). If needed, cells were added at this point, and the prepolymer solution was UV-cured into the desired shape for 1 min (0.09 mW/cm^2) using a UV box (VWR).

5.2.3.2 Gelatin Methacrylate layered and 3D printed scaffolds fabrication

To demonstrate the feasibility of aFLOT imaging of cell distribution inside engineered tissue scaffolds, L929 fibroblasts were labeled with orange fluorescent dye (CellTracker™ Orange CMRA Dye, 548⁄576 nm, Thermo Fisher Scientific). The labelled cells were suspended into a solution of 10w/v% gelatin methacrylate (gelMA), and 3D constructs were obtained by photo crosslinking of the solution. The constructs were seeded at concentrations of 0.015×10^6, 0.05×10^6, 0.1×10^6, 0.5×10^6,1×10^6 and 2×10^6 cells/mL. The hydrogels with different cell concentrations were then imaged by the aFLOT system.

To demonstrate the depth-resolve capability of the aFLOT system, we fabricated a three-layer structure with an acellular gelMA layer in the middle and two layers with fluorescent labelled cells (1M cells/mL) as illustrated in Fig. 2(B). The L929 fibroblasts were labelled either with orange fluorescent dye (CellTracker™ Orange CMRA Dye, 548⁄576 nm, Thermo Fisher Scientific) or far red fluorescent dye (DiIC18(5)-DS,650/670 nm, Thermo Fisher Scientific) to demonstrate the multi-wavelength capability of the aFLOT system. We also constructed a three-layer

gelMA cylinder with far red labelled cells (2M cells/mL) in the middle, orange labelled cells at the left and right sides (or the other way, orange labelled cells in the middle, far red labelled cells at the left and right sides) as shown in Fig. 3.

Furthermore, samples were 3D printed using an extrusion-based bioprinter (3D-Bioplotter; EnvisionTEC; Germany). The bioink containing orange or far red-labelled cells was loaded into the low-temperature printer head and allowed to equilibrate for 30 min at 22 ^{o}C. Printed constructs were UV-cured for 30 s (0.09 mW/cm^2) using a UV box (VWR) [206]. In this study, three letters "UMD" were printed using a labeled-cells suspension of gelMA, with far red and orange labelled cells respectively. Another construct mimicking bone osteon was also printed as shown in Fig. 4(B).

5.2.4 Cell migration model

To demonstrate the feasibility of aFLOT imaging to track cell migration inside a scaffold, orange-labelled (CellTracker™ Orange CMRA Dye, Thermo Fisher Scientific) hMSCs were encapsulated in 10w/v% GelMA to print cylindrical scaffolds at a concentration of 4x10^6 cells/mL. Acellular gelMA was printed along the periphery of the cylinder, while cells were printed in the center. Samples were cultured in growth media and imaged at different time points over the course of four days to study cell migration from the center toward the edge of the gel.

5.2.5 Cell differentiation study

To demonstrate the feasibility of aFLOT imaging to visualize cell differentiation, hMSCs were cultured in a tubular perfusion bioreactor under differentiation condition

[207]. Hydroxyapatite (HA) deposition, indicator of hMSCs differentiation into osteoblasts, was assessed using both aFLOT and histology.

5.2.5.1 Alginate beads fabrication

Alginate beads were fabricated as described previously in the literature [208]. Alginate solution (Sigma, St. Louis MO) was sterilized via sterile filtration then mixed with a cell pellet containing hMSCs. Beads were seeded with orange fluorescent dye labelled cells (CellTracker™ Orange CMRA Dye, 548⁄576 nm, Thermo Fisher Scientific) at a concentration of $2x10^6$ cells/mL. This solution was added dropwise by 20 gauge syringe to a 0.10 M calcium chloride solution, in which the alginate was ionically cross-linked into beads. The solution was stirred for 15 min. Beads were transferred to the tubular perfusion system, as described in [209, 210], and cultured for 14 days in control media supplemented with 100 nM dexamethasone (Sigma, St. Louis MO), 10 mM β-glycerophosphate, and 173 µM ascorbic acid.

5.2.5.2 Hydroxyapatite (HA) deposition assay

For each time-poin during the 14 days study, alginate beads were removed from the bioreactor and washed for 15 min in PBS. The beads were stained for HA deposition in 300 µl of Osteosense 680 [211] (Perkin Elmer) per ml of PBS. After 15 min incubation, the beads were rinsed again and imaged using the aFLOT system. The labelled cells were imaged using the 520-nm laser diode, and the labelled HA was imaged by 637-nm laser diode with 561-nm/695-nm long-pass emission filters respectively.

5.2.5.3 Histology

At each time-point, beads were collected and fixed in 4% paraformaldehyde (Sigma) for 12 h at 4°C. Following fixation, the beads were dehydrated for histological processing by ethanol washes followed by two citrisolv (Fisher Scientific, Pittsburgh, PA) washes. The samples were then embedded in paraffin (Fisher Scientific, Pittsburgh, PA) and sectioned to 5 μm thickness sections and placed on glass slides. Sections were oven dried at 64°C for 2 h, deparaffinized in citrisolv, and rehydrated in ethanol. Von Kossa staining was performed to visualize mineralization using a Nuclear Fast Red (Poly Scientific, Bay Shore, NY) counterstain using standard protocols.

5.3 Results and Discussion

5.3.1 Imaging of cell distribution using aFLOT

We demonstrated here the feasibility of using aFLOT to image the cell distribution and quantify cell density inside a 3D scaffold. At a cell density of 0.015×10^6 cells/mL, the fluorescent spots were sparsely distributed as shown in Fig.1 (A). With increasing cell density, the fluorescence from the 3D reconstructed images become denser. When the cell density is larger than 2×10^6 cells/mL, the fluorescence-labeled cell clusters become too dense to be resolved (i.e., the image becomes homogeneous). To further quantify the correlation between aFLOT detected cell number and the true cell density, the number of fluorescent pixels over a preset threshold value (Background + (Max-Background)/2) were counted and averaged from ten random 3D cubic voxels (each contained 30x30x30 pixels) from 3D reconstructed images with different cell densities. The averaged pixel numbers were then normalized and plotted as a function of the true cell densities, as shown in Fig.1 (G). The pixel value

of the 2×10^6 cells/mL group was set as 1, and was used to normalize the results from other groups. The normalized averaged pixel numbers show an excellent linear response to the true cell densities with R^2= 0.99. This demonstrates the capability of aFLOT to correlate fluorescence imaging results with cell density and quantify cell growth in 3D samples in a non-destructive manner. Therefore this technique presents the advantage of monitoring a same sample overtime, unlike standard cell viability/proliferation assay such as XTT (2,3-bis[2-methoxy-4-nitro-5-sulfophenyl]-2H-tetrazolium-5-carboxyanilide tetrazolium salt), which is primarily an end point assay.

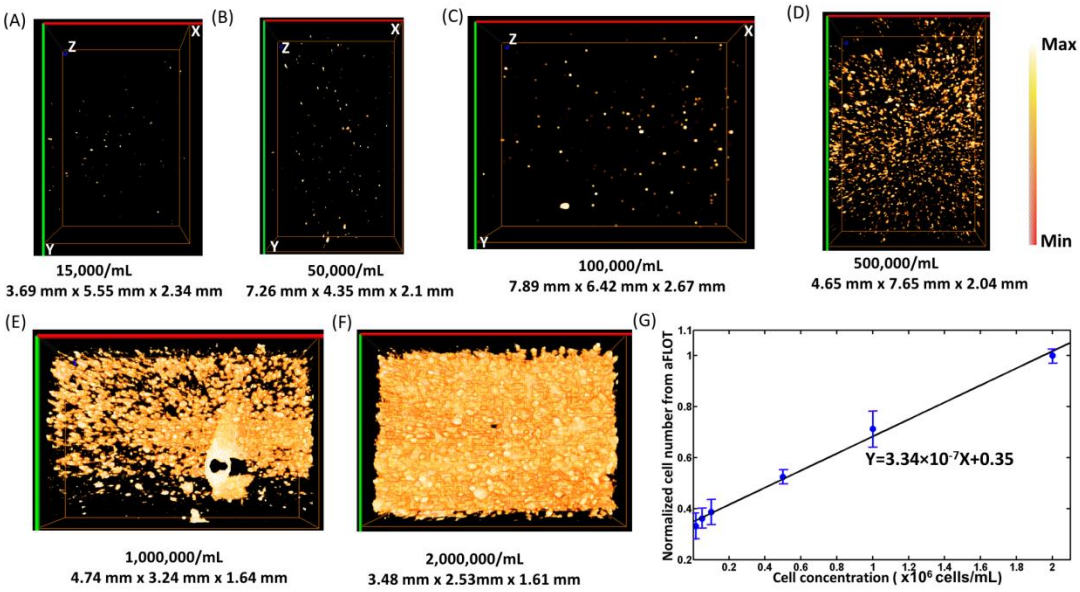

Figure 1. 3D aFLOT reconstruction images of Orange labelled fibroblast cells

(A) 3D aFLOT reconstruction images of Orange labelled fibroblast cells 15000/ml (A), 50000/ml (B), 100000/ml (C), 500000/ml (D), 1000000/ml (E), 2000000/ml (F), in the PEGDA gel. (G) Normalized averaged cell numbers from aFLOT as a function of true cell concentration in the gel. The Max in the colormap is the maximum value in the image and Min represents the value: (Background + (Max-Background)/2).

5.3.2 Demonstrating the depth-resolve imaging capability of aFLOT

To demonstrate the depth-resolve imaging capability of our aFLOT system, different fluorescence-labeled cells were seeded in the three-layer gelatin methacrylate scaffolds, different views at different depths are shown in Fig. 2. The aFLOT system

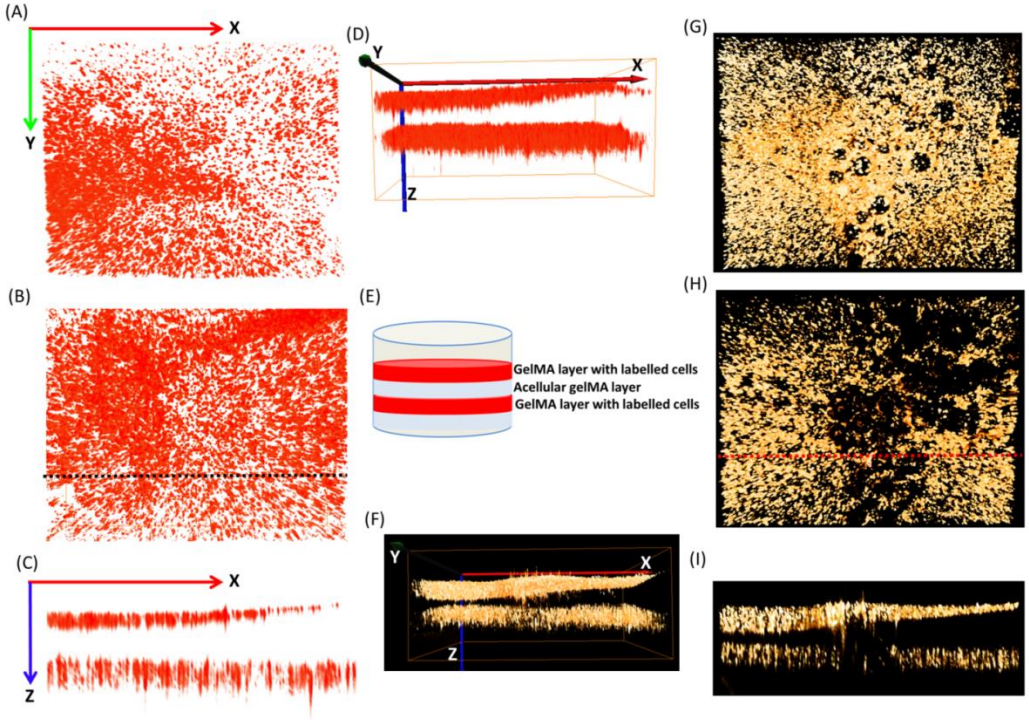

Figure 2. AFLOT reconstructed three-layer structure

(A) Upper layer of the 3D aFLOT reconstructed three-layer structure labelled by far-red fluorescence. (B) Lower layer of the 3D aFLOT reconstructed three-layer structure labelled by far-red fluorescence. (C) Cross-section of the 3D aFLOT reconstructed three-layer structure labelled by far-red fluorescence as indicated by the black dashed line in Fig. 2(B). (D) Side view of the 3D aFLOT reconstructed three-layer structure labelled by far-red fluorescence. (E) The three-layer gel structure. (F) Side view of the 3D aFLOT reconstructed three-layer gel structure labelled by orange fluorescence. (G) Upper layer of the 3D aFLOT reconstructed three-layer structure labelled by orange fluorescence. (H) Lower layer of the 3D aFLOT reconstructed three-layer structure labelled by orange fluorescence. (I) Cross-section of the 3D aFLOT reconstructed three-layer structure labelled by orange fluorescence as indicated by the red dashed line in Fig. 2(H). FOV: XYZ: 7.63 mm x 5.9 mm x 3.72 mm.

was able to image samples with more than 3 mm thickness, for both wavelength channels (far red and orange). To further demonstrate the capability of the imaging system in performing multi-wavelength imaging, other gelMA constructs seeded with both far red labelled cells and orange labelled cells were fabricated and imaged as

shown in Fig. 3. Fig. 2 further indicates the feasibility of aFLOT system to image the distribution of fluorescent-labeled cells in a 3D scaffold with great in-depth precision, and therefore enabling quantification of cell infiltration into hydrogel scaffolds.

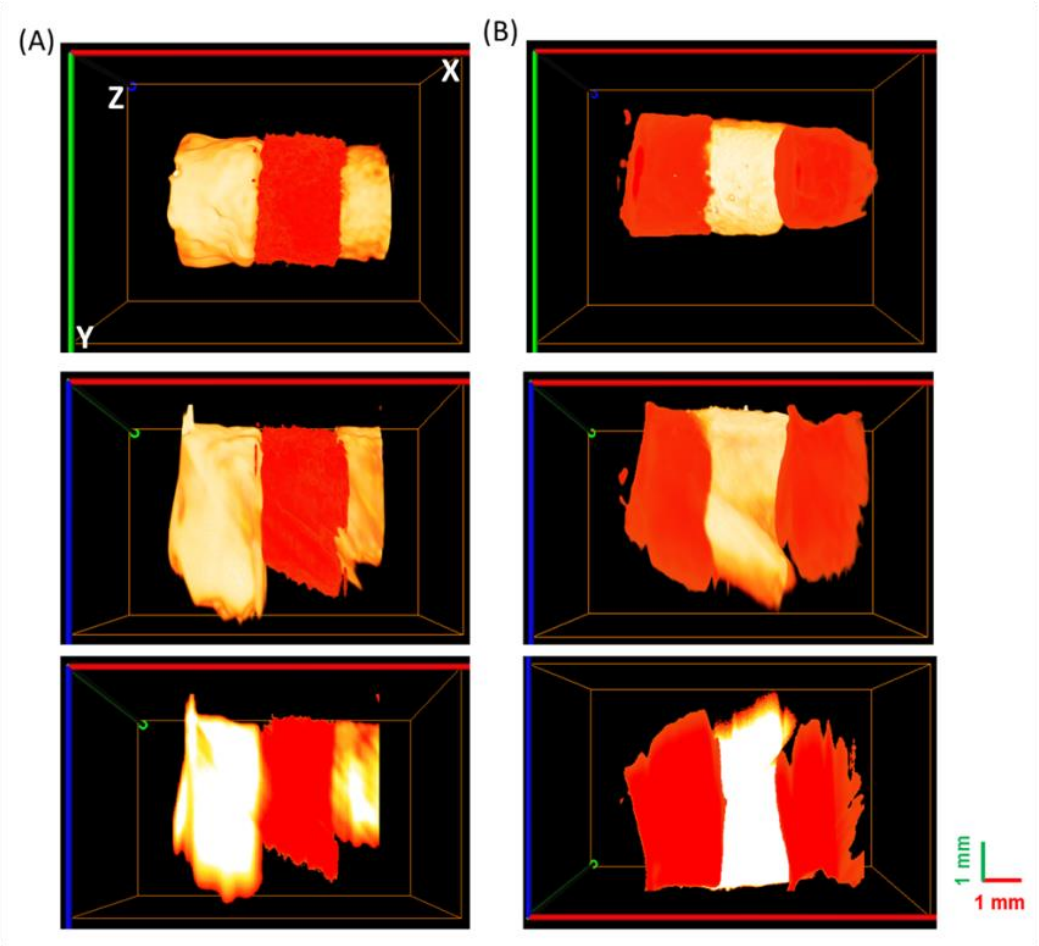

Figure 3. The reconstructed 3D aFLOT sandwich structure
(A) Top view, side view, and XZ cross-section of the reconstructed 3D aFLOT sandwich structure labelled by orange fluorescence and far-red fluorescence, respectively. (B) Top view, side view, and XZ cross-section of the reconstructed 3D aFLOT sandwich structure labelled by far-red fluorescence and orange fluorescence, respectively.

In addition, to validate the capability of the aFLOT system to reconstruct more complex structures or patterns, several samples were 3D printed using a suspension of gelMA and far red or orange labelled L929 cells, as shown in Fig. 4. AFLOT successfully reconstructed the printed patterns regardless of the spectral range as

shown in Fig. 4(A), demonstrating the ability of aFLOT to recover the patterns with accuracy.

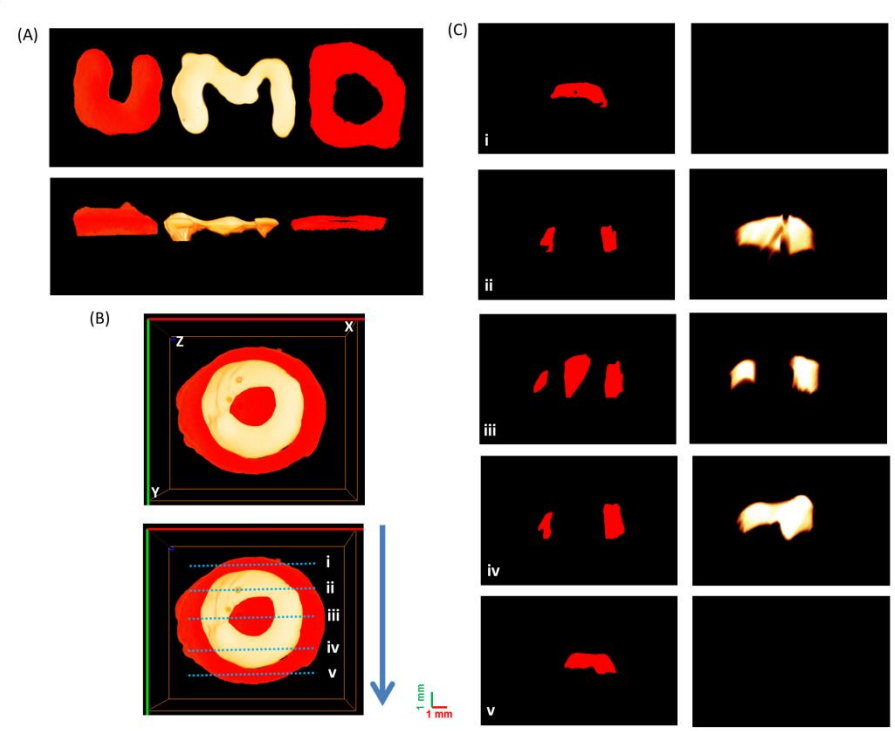

Figure 4. AFLOT reconstructed 3D printed images
(A) Top view and side views of the 3D aFLOT reconstructed 3D printed U,M,D letters labelled by far-red fluorescence and orange fluorescence, respectively. (B) Top view of the 3D aFLOT reconstructed 3D printed 'Osteon' structure labelled by far-red fluorescence and orange fluorescence, respectively. (C) Cross-sections of the 3D aFLOT reconstructed 3D printed 'Osteon' structure from the blue dashed lines labelled in (B).

An osteon-like structure was also 3D printed (Fig. 4B) to illustrate the potential application of aFLOT in bone tissue engineering. Osteons are a repetitive unit found in cortical bones consisting of organized concentric calcified regions with interpenetrated vasculature. Osteons consist of organized concentric calcified regions with interpenetrated vasculature, represented here by two cell populations labelled with different fluorescent proteins. The biomimetic osteon-like scaffolds were also imaged, as shown in Fig. 4(B). The concentric layers, or lamellae were successfully printed using cells labelled with different fluorescent proteins and reconstructed by

the aFLOT system. Fig. 4(C) shows the cross-sections of the reconstructed scaffolds from the blue dashed lines labelled in Fig. 4(B), demonstrating the capability of the aFLOT system in analyzing precise areas of a sample and identifying different cell populations.

5.3.3 Demonstrating the feasibility of aFLOT imaging to track cell migration

Cell migration is fundamental to many biological and pathological processes. Development, immune response and wound healing all rely on the directed migration of cells [212]. Moreover, in the case of tissue engineering, understanding cell migration within the native organ is important to evaluate cellular interactions with biomaterials and therefore creating successful outcomes.

In this study, we tracked the migration of hMSCs within a 3D printed gelatin methacrylate scaffold from a high cell density area (4×10^6 cells/mL) to a low cell density area (no cells). As illustrated in Fig. 5 (A)-(C), the scaffolds with 4×10^6 cells/mL have a strong fluorescence. On the first day, no cells outside the high density zone can be seen. After two days, cells outside of the high density zone can be detected. Finally after four days, cells have migrated further into the no cell area. To quantify the migration distance, the cells numbers was plotted over migration distance at day 2 and day 4 as shown in Fig. 5(D). The average migrated distance was defined as $D_{ave} = \sum_{i=1}^{X} \frac{N_i}{T} \times D_i$, X is the number of different migration distances, N_i is the pixel number of the migrated cells at the migration distance D_i, and T is the total number of the pixels that migrated (The migrated cell are defined as the fluorescent pixels over a preset threshold value (Background + (Max-Background)/2)). The

average migrated distance after two days is 650±38 µm and increased to 1208±167 µm after four days. The average migration rate of 12.6±2.33 µm/h is consistent with what have been previously reported in the literature [213, 214].

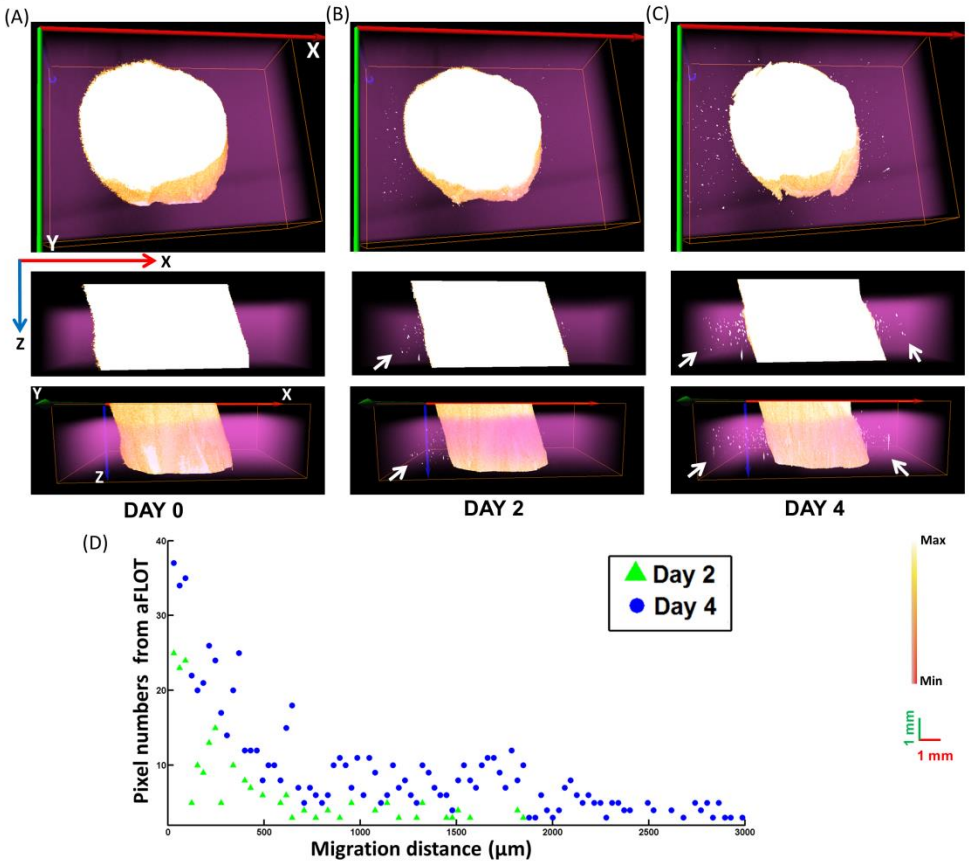

Figure 5. 3D aFLOT reconstructed migration model

Top view, cross-section from the center and side views of the 3D aFLOT reconstructed migration model at day 0 (A), day 2 (B), and day 4 (C). The Max in the colormap is the maximum value in the image and Min represents the value: (Background + (Max-Background)/2). The migrated and proliferated cells were indicated by the white arrows. (D) Cells (Pixels) numbers was plotted over migration distance at day 2 and day 4.

AFLOT is a promising tool to accurately follow cell migration. It presents the advantage of accurately tracking cells in 3D scaffolds when compared to conventional time-lapse microscopy. As migration of some cell types differs

dramatically between 2D and 3D environments, it is critical to be able to evaluate the effect of the structure and/or biomaterial on 3D cell migration [215, 216].

5.3.4 Demonstrating the feasibility of aFLOT imaging to visualize markers of cell differentiation

The capability of aFLOT to indirectly image and quantify cell differentiation was demonstrated in this study by evaluating the mineralization of alginate scaffolds seeded with hMSCs and cultivated in a tubular perfusion bioreactor (TPS). Mechanical stimulation from a perfusion bioreactor have been shown to induce osteoblastic differentiation of hMSCc [207, 209], with a significant increase in mineralization of the scaffold.

In this study, mineralization of alginate scaffolds were evaluated using our aFLOT system along with the near-infrared (NIR) fluorescent bisphosphonate derivative (OsteoSense 680 EX, Perkin Elmer), that exhibits rapid and specific binding to HA *in vitro* and *in vivo* [211]. Calibration of the aFLOT system in different HA concentrations was first carried out as shown in Fig. 6. The normalized pixel numbers from aFLOT show a linear relationship with HA percentage in the alginate beads, and the images of alginate-beads doped with different HA concentrations are also shown in Fig. 6. However, due to the increasing scattering as the HA concentration increases, high mineralization results in a decrease in light penetration into the sample, and therefore it is difficult to reconstruct deeper signals accurately. In the future, we can flip the sample to image the samples from different views and thus increase the sample imaging area.

Fig.7 (A) and (B) show different views of the 3D aFLOT reconstructed scaffolds seeded with hMSCs. HMSCs (orange-red) and HA (green-blue) distribution are superimposed with the alginate bead (pink). 3D cell distribution is clearly displayed and well co-registered with the bead contour. No HA deposition is seen at day 0. Cell distributions at different depths are further exhibited in Fig.7 (I). At day 7 HA deposition is still low, however cell proliferation is shown by the appearance of larger 'clusters' (Fig.7 (E) and (J)). At day 14, cells have continued to proliferate, as more large 'clusters' can be seen, and the HA deposition (green-blue) can be clearly seen in the alginate beads as shown in Fig.7 (B) and (F). 3D distribution of HA deposition and location with respect to the bead can be observed more clearly in Fig.7 (C) and (G). Most of the HA was deposited in the center of the bead, which can be clearly revealed at the depth 1.5 mm in Fig.7 (M).

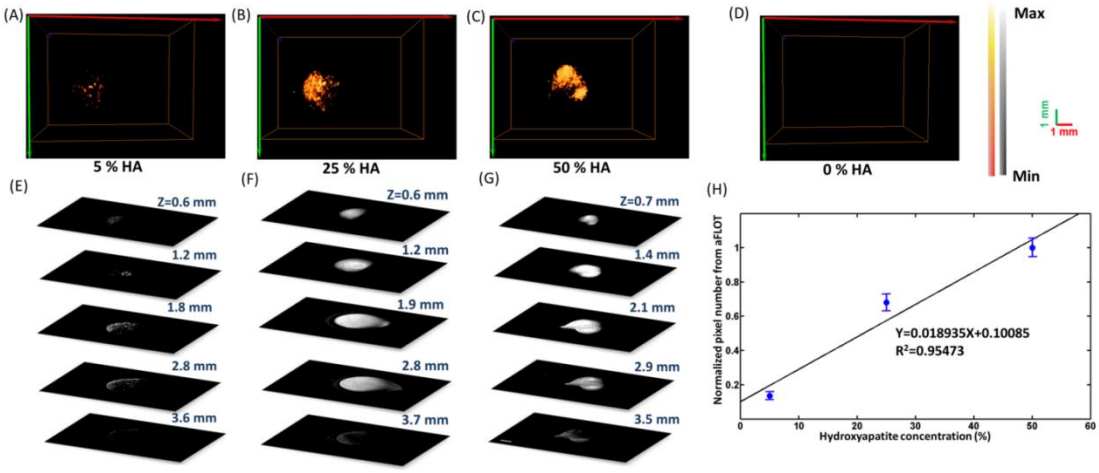

Figure 6. Quantification of the reconstructed 3D aFLOT HA+alginate-beads structure (A) – (D) Top views of the reconstructed 3D aFLOT HA+alginate-beads structure with different HA concentration labelled by OsteoSense 680. (E)-(G) XY cross-sections of the reconstructed HA+alginate-beads with different HA concentration at different depths. Scale bar=1 mm. (H) Normalized pixel numbers from aFLOT as a function of HA percentage in the gel. The Max in the colormap is the maximum value in the image and Min represents the value: (Background + (Max-Background)/2).

To confirm mineralization of the scaffolds, Von Kossa staining was performed alongside aFLOT imaging. The Von Kossa stain uses silver nitrate to detect calcium salt deposits with a black or brownish-black precipitate, and nuclear fast red to stain cell nuclei red and the cell cytoplasm pink. Von Kossa staining confirmed increased mineralization in the alginate scaffolds over the 14 day study in Fig.7 (N)-(O). In addition, cell nuclei (shown in pink), are observed to increase in number from day 7

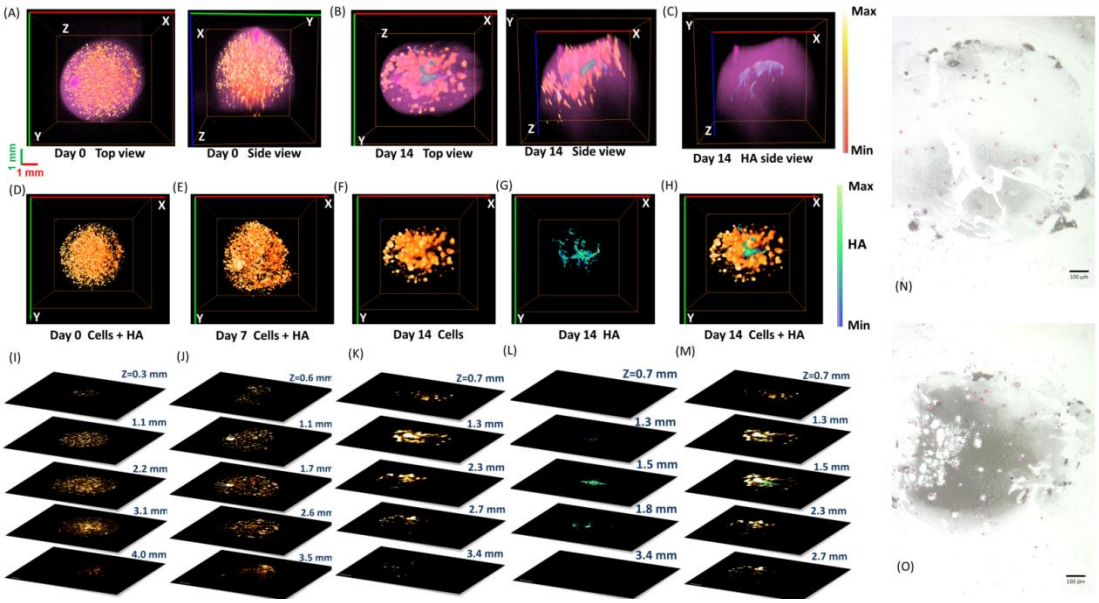

Figure 7. 3D aFLOT reconstructed cell differentiation model

Top view and side view of the 3D aFLOT reconstructed hMSCs (orange-red) and HA (green-blue) distribution superimposed with the bead surface (pink) in the alginate beads at day 0 (A) and day 14 (B). (C) Side view of the 3D aFLOT reconstructed HA distribution (green-blue) superimposed with the bead surface (pink) in the alginate beads at day 14. (D)-(F) Top views of the 3D aFLOT reconstructed hMSCs (orange-red) at day 0 (D), day 7 (E), and day 14 (F). (G) Top view of the 3D aFLOT reconstructed HA (green-blue) distribution at day 14. (H) Top views of the 3D superimposed aFLOT reconstructed hMSCs (orange-red) and HA (green-blue) distribution in the alginate beads at day 14. (I)-(M) Corresponding XY cross-sections of the 3D aFLOT reconstructed alginate beads at different depths to (D)-(H). Scale bar: 1 mm. (N)-(O) Von Kossa staining of alginate scaffold at Day7 (N) and Day 14 (O), respectively. Mineralization is stained in black while cell nucleus appears in pink.

to day 14. This study demonstrates that aFLOT imaging is able to image osteoblastic activity, and offer a practical, time-saving, non-destructive alternative to conventional histology.

5.4 Conclusion

In this paper, we demonstrated various potential applications of aFLOT in bone tissue engineering, and more specifically in non-destructively quantify the depth-resolved information of cell-scaffold interactions. We are able to successfully quantify 3D cell density and characterized cell distribution within a 3D scaffold, and visualize the 3D migration process of cells. Finally we are able to indirectly evaluate cell differentiation by quantifying the mineralization of alginate scaffolds, seeded with hMSCs, by measuring HA deposition. AFLOT is a promising tool in regenerative medicine, allowing to non-invasively investigate structural, cellular, and molecular information, therefore it enables longitudinal studies of cell viability, migration, proliferation, differentiation, and signaling within 3D scaffolds both *in vitro* and *in vivo*. Such an imaging technology could also provide useful information on the interplay of scaffold designs and materials, cell-seeding methods, and chemical/environmental cues to optimize the development of tissue grafts.

Chapter 6: Depth-resolved imaging of colon tumor using optical coherence tomography and fluorescence laminar optical tomography*

6.1 Introduction

Early detection of neoplastic changes remains a critical challenge in clinical cancer diagnosis and treatment. Many cancers arise from epithelial layers such as those of the gastrointestinal (GI) tract. White-light endoscopy guided excisional biopsy and histopathology is currently the gold standard for GI cancer diagnosis. However, it suffers from high false negative rates due to sampling errors [27-30]. Furthermore, a significant portion of patients after endoscopic ablative therapeutic treatment showed the presence of metaplasia or dysplasia buried underneath the neo-epithelium [31-35], which is associated with the risk of cancer development [30, 36-39]. Current standard endoscopic technology is unable to detect those subsurface lesions. Therefore, there is a critical need for developing new diagnostic tools which can assess tissue architectural and molecular information across the mucosal depth for improved detection of subsurface cancer, and evaluate the invasion depth of a lesion.

Optical coherence tomography (OCT) is an established biomedical imaging technology for subsurface imaging of tissues with high resolution (<10 μm) and 1-2

* The contents in this chapter is reproduced from "Q. Tang, J. Wang, A. Frank, J. Lin, Z. Li, C.-w. Chen, L. Jin, T. Wu, B. D. Greenwald, H. Mashimo and Y. Chen, "Depth-resolved imaging of colon tumor using optical coherence tomography and fluorescence laminar optical tomography," *Biomedical optics express* **7**(12), 5218-5232 (2016)

mm penetration depth [43-46], which is comparable to the size of standard pinch biopsy and histology. OCT can be interfaced with fiber-optic catheters and endoscopes to image inside the body [45, 64-66]. Endoscopic OCT has been demonstrated in the human GI tract [67-70] to detect Barrett's esophagus (BE) [71, 72] and dysplasia [73, 74]. OCT's high depth-resolution and appropriate penetration depth make it an attractive technology for detecting subsurface abnormalities in the mucosal and submucosal layers. Visualization of cross-sectional mucosal and submucosal features is a key advantage of OCT imaging when compared to standard endoscopy.

OCT can provide high-resolution morphology information, but is less sensitive to biochemical or molecular processes associated with early neoplastic formation before the exhibition of structural alterations. Fluorescence imaging has high sensitivity for detecting biochemical and molecular alterations, but has limited specificity [107]. Combining these two complementary imaging technologies would potentially improve the diagnostic capability for early cancer detection. Previous studies using OCT and depth-integrated fluorescence imaging already showed substantial promises in cervical [217, 218], bladder [107, 219], colorectal [220-222], and bronchial cancers [223]. However, depth-integrated fluorescence imaging lacks the depth-resolved information, therefore may not sufficiently indicate the subsurface lesions or estimate the depth-extent of the lesions. In addition, the detected fluorescence intensities are non-linearly attenuated with different imaging depths [224-226], which could lead to a surface weighted images.

Laminar optical tomography (LOT) is a promising approach to overcome this limitation by using multiple detectors to collect lights travelling through different depths, and through mathematical de-convolution to reconstruct the depth-resolved image [80, 91, 93]. LOT

has a resolution of ~100 μm with 2-3 mm penetration depths [80, 90-93, 190], which is comparable to the imaging depth of OCT, as well as the size of typical biopsy and histology. LOT imaging of skin cancer based on absorption contrast has been demonstrated [159]. Fluorescence-based LOT (FLOT) has the potential to quantify depth-resolved distribution of fluorescence-labeled tumor [19, 100, 102, 103].

Since cancer development is associated with both morphological and molecular alterations, imaging technologies that can quantitative image tissue's morphological and molecular biomarkers and assess the depth extent of a lesion, without the need for tissue excision, would be a major advance in cancer diagnostics and therapy. In this paper, we investigated multi-modal depth-resolved imaging approach by co-registering high-resolution OCT and high-sensitivity FLOT for both structural and molecular imaging. Our data on multi-modal imaging of mice colon tumor model demonstrated the feasibility of combining structural and molecular information for more accurate diagnosis.

6.2 Materials and methods

6.2.1 Animal preparation

All animal procedures were approved by the Institutional Animal Care and Use Committee (IACUC) at the University of Maryland, and animals were treated in accordance with the PHS Policy on Humane Care and Use of Laboratory Animals, the National Institutes of Health Guide for the Care and Use of Laboratory Animals, and the Animal Welfare Act (7 U.S.C. et seq.). Six 8-week-old male C57BL/6J-Apc^{Min}/J mice were purchased from Jackson Laboratory (Bar Harbor, ME). The mice received a high fat diet consisting of 23% corn oil in order to increase tumor incidence in the distal colon [227]. At time points of ~18 weeks, the mice were prepared

for imaging study. One day before imaging, the mice were injected with the cathepsin B-sensitive contrast agent (ProSense^{TM} 680, PerkinElmer), which was non-fluorescent at injection and locally activated after target interaction [228, 229]. After 24 hours, animals were euthanized. For each animal, a 5-cm long section of colon from the distal end was removed, opened longitudinally, and flushed with isotonic saline. The excised colon was pinned flat and fixed using Formalin in place to minimize fixation artifacts. After fixation, the samples are ready for imaging. Photos of all the samples were taken using a digital camera and all the tumors were numbered properly, which would be used to match the measurements from OCT/FLOT with histology results.

6.2.2 System setup

Fig. 1(A) shows the OCT system setup. This frequency-domain OCT imaging system utilized a wavelength-swept laser as light source which was centered at 1310 nm with 100 nm bandwidth [230]. The wavelength-swept frequency was 16 kHz with 17 mW output power [231]. About 97% of the laser power was split evenly to the sample and reference arms of a fiber-based Michelson interferometer [169, 173]. The signals reflected from the sample and reference arms formed interference fringes at the fiber couple (FC). The interference fringes from different depths received by a balanced detector (BD) were encoded with different frequencies. A Mach-Zehnder interferometer (MZI) obtained the remaining 3% of the laser output power and generated a frequency-clock signal with uniformly spaced optical frequency to trigger the sampling of the OCT signal [94]. Depth-resolved tomography can be achieved by performing fast Fourier transform of the interference fringes. During imaging, the

colon tissue was irrigated by phosphate buffer saline (PBS) to prevent dehydration [168].

The schematic of the FLOT system is shown in Fig. 1(B). A 637 nm laser diode was utilized as light source. Light from the laser diode was collimated and coupled into a single-mode fiber to shape the light beam. Light coming out from the fiber was first collimated by an objective lens (O1) and then passed through a polarizer (P1). The collimated light was expanded into line-field illumination using a cylindrical lens with a full line-width at the half maximum of 26 μm at the focal plane. An iris was used to control the length of the line illumination. The backscattered light and emitted fluorescent light were collected back through a cross-polarizer (P2, which was used to reject the specular reflection from the sample surface), another objective lens (O2), a filter wheel (695 nm emission filter for fluorescence imaging and no filter for reflectance imaging), and finally imaged on a CCD camera (EM-CCD, CooKe). Recent studies indicated angled illumination and detection configurations can improve both resolution and depth sensitivity [80, 112]. The illumination angle was set at 45°, rendering ~30° transmission angle in tissue (n~1.33). The CCD camera was placed vertically to record both fluorescence and reflectance images by rotating the filter wheel. Because of the defocusing effect, we set the focal plane slightly below the sample surface. The scattering coefficient (μ_s) of the colon sample was determined from the reflectance data using oblique-incidence spectroscopy [170] to be ~146 cm^{-1}. A motorized stage was used to translate the sample laterally in scanning direction X (perpendicular to the line illumination direction Y) with the speed of 0.2156 mm/s.

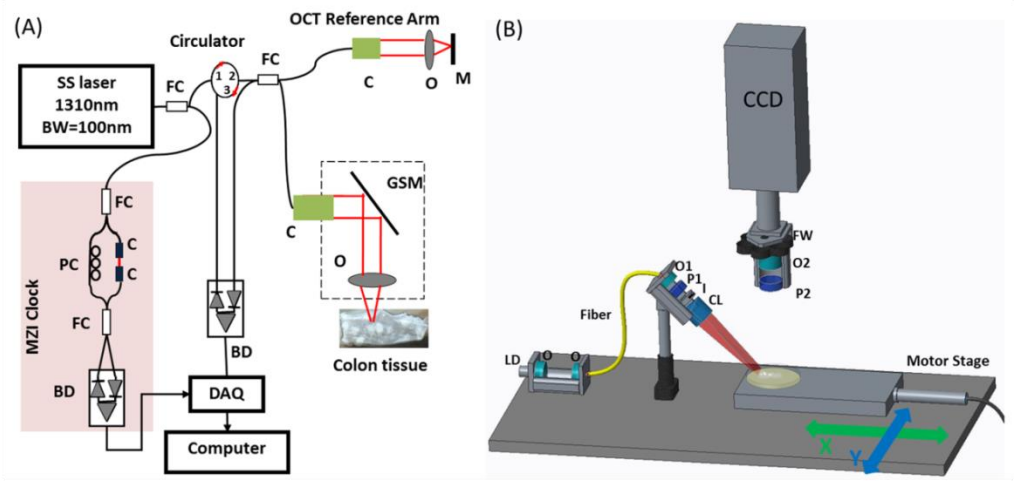

Figure 1. Schematic of the OCT and FLOT system

(A) Schematic of the OCT imaging system. (B) Schematic of the FLOT system. FC: fiber coupler; PC: polarization controller; C: collimator, BD: balanced detector, MZI: Mach-Zehnder interferometer (frequency clocks), DAQ: data acquisition board, M: mirror, GSM: galvonometer scanning mirror, O: objective lens, LD: laser diode, P: polarizer, S: shutter, I: iris, CL: cylindrical lens, FW: filter wheel.

6.2.3 Data acquisition and image reconstruction

For FLOT image acquisition, the illumination line was first focused on the border (X=0) of the sample field of view (FOV). At each scanning position, one 2D XY image (512x512, with pixel dimension of 30.8 μm) was obtained with 100 ms exposure time. Next, the motorized stage moved the sample in X direction with a step size of 30.8 μm to another illumination/collection position. Another 2D XY dataset was obtained. This process was repeated until finishing the entire sample scanning [80]. The raw measurement had the format of XYT. A typical 3D dataset recorded 512×512×400 XYT voxels. In order to fit the experimental data to the theoretical model for precise reconstruction, the surface of colon tissue must be found. To obtain the surface tomography of the colon tissue, the emission filter was removed, and the same FOV was scanned to get the reflectance images with the same scanning/acquisition protocol but lower laser power to avoid saturated image. Without

emission filter, most of the collected light was from the reflection of the illumination light at the tissue surface, which would then serve as an indicator of the location of tissue-air interface. The raw measurement of reflectance dataset had exactly the same format of XYT (X=512, Y=512, T=400).

To reconstruct the images, the 3D datasets were first downsized to 256×256×200 XYT voxels. The raw measurements of the reflectance data were stacked together according to the geometrical relationship between the illumination plane and the detection FOV, which was similar to the unprocessed stacked raw image in selective plane illumination microscopy [176]. Additionally, the stacked reflectance data were used to co-register with the 3D OCT data based on the shape / structural features of the same tumor. To reconstruct the fluorescence image, first-order Born approximation was assumed to obtain linearity between the measurement F and the fluorophore distribution C, i.e., for each FOV_{XZ}, $F = JC$, with J the weight or sensitivity matrix [80, 103]. To constitute J, photon distribution was first generated by Monte-Carlo simulation [137] (g=0.9, n=1.33, $\mu_a=0.01\times\mu_s$, $\mu_s=146$ cm^{-1}). Then the reciprocity principle was applied to obtain J. J was later decomposed by singular value decomposition (SVD) [177]. Lastly, least square fitting and Tikhonov regularization were used to solve the underdetermined system [112]. The regularization parameter $\alpha=0.0021$ was determined by L-curve criterion [178]. 100 source-detector pairs and 100 scanning positions starting from the surface were chosen to constitute F with 10,000 measurement data. Each reconstructed FOV_{XZ} included 100×100 pixels with a pixel size of ~61.6 μm. The entire volume FOV_{XYZ} was constituted by juxtaposing individual FOV_{XZ} along Y-direction. After imaging, the pinned tissue specimens were processed for histology and pathological review (Histoserv, Inc).

6.2.4 Data quantification

To achieve quantitative characterization of tumors and normal tissues in mouse colon, the structural and molecular parameters can be extracted from OCT and FLOT images respectively. Tissue extinction coefficient (μ_t) (or the slope of axial attenuation) is an indication of local tissue scattering changes associated with neoplasia, and has been shown to be able to detect dysplasia in oral cavities [232, 233] and breast cancer [234, 235]. The extinction coefficient (μ_t) can be estimated by fitting the OCT axial-scan intensity profiles with the single-scattering model: $I(z) \propto \exp(-2*\mu_t*z)$ [236]. Since the extinction coefficient (μ_t) is the sum of the absorption coefficient (μ_a) and scattering coefficient (μ_s), the enhanced light attenuation in the tumor regions could be due to the increase of tissue scattering coefficient, which is closely related to the structural changes such as nuclear-to-cytoplasmic ratio and extracellular matrix remodeling during the neoplastic progression. Absorption coefficients might be also changed due to changes in water contents (such as in the case of edema). However, at 1300 nm, for typical GI tissues, the scattering coefficient is at least one order of magnitude larger than the absorption coefficient [237]. Therefore, the majority of attenuation could be due to scattering, i.e., $\mu_t \approx \mu_s$. We therefore quantified the scattering coefficient (μ_s) as the structural parameter.

Molecular parameters include the level and spatial distribution of enzyme (cathepsin B) activities, which can be quantified from the depth-resolved FLOT tomogram using cathepsin-B-activatable contrast agent. Depth-resolved FLOT is capable of reconstructing the intensity and depth distribution of the contrast agent (ProSense^{TM}680). To calibrate the constructed values to fluorophore concentrations, capillary tubes with 200 μm inner diameter and 330 μm outer diameter (Vitrocom. Inc) filled with different concentrations of fluorescence dye Cy5.5

(0.5 μM, 1 μM, 1.5 μM) were used as a calibration phantom. They were placed ~500 μm deep in the scattering medium containing 1.5 g Agar powder, 1 mL intralipid (20% solution), and 49 mL PBS buffer with μ_s~146 cm^{-1} at 637 nm, which is close to colon tissue scattering coefficient. The reconstructed relative enzyme activity value for 0.5 μM, 1 μM, 1.5 μM Cy5.5 were 207.66, 217.46 and 224.50 respectively revealing a good linear relationship with R^2=0.99113 which can serve as a good reference for the FLOT system used.

6.2.5 Data statistical analysis

According to the sample size calculation in the study plan, we recruited 17 samples in total (from 6 different animals) to ensure at least 80% power to detect the difference between tumor and normal tissues. No missing data are observed in this study. Descriptive statistics such as mean and standard deviation were calculated. The distributions of scattering coefficients μ_s and relative enzyme activity of tumor tissues to the normal tissues were examined to verify the normality assumption. Ratios of absolute diameter and thickness difference from OCT and FLOT to histology (gold standard) at different thresholds were compared to determine the optimal threshold values (the smaller the better). Boxplots are used to demonstrate the difference in parameters for tumor and normal tissues using OCT and FLOT. Student *t*-test was also used to compare the mean diameter and thickness from OCT and FLOT to histology at the chosen thresholds. Student *t*-test was used to compare scattering coefficient μ_s and relative enzyme activity of tumor tissues to the normal tissues. To quantify the diagnostic sensitivity and specificity for GI cancer detection using multi-modal OCT/FLOT imaging technologies and validate its capability for enhanced cancer detection compared to single modality alone, different thresholds of the tissue scattering coefficient (μ_s) (for OCT) and relative enzyme activity (for FLOT) were applied. To classify

tumor tissue and normal tissue near tumor with combined OCT and FLOT results, linear discriminant analysis (LDA) was trained with relative enzyme activity and tissue scattering coefficient (μ_s) from the datasets plotting in X and Y dimensions respectively and applied to new testing samples. Receiver operations curve (ROC) was also used to assess the classification performance based on FLOT, OCT and the combined criteria. Statistical analyses were carried out using MATLAB (The MathWorks Inc., Natick, MA). Statistical significance is considered at $P = 0.05$.

6.3 Results and Discussion

A representative 3D OCT colon tissue volume is shown in Fig. 2(A). The shape of colon tumor is clearly displayed. Fig. 2(B) shows 3D FLOT image of the same colon tissue.

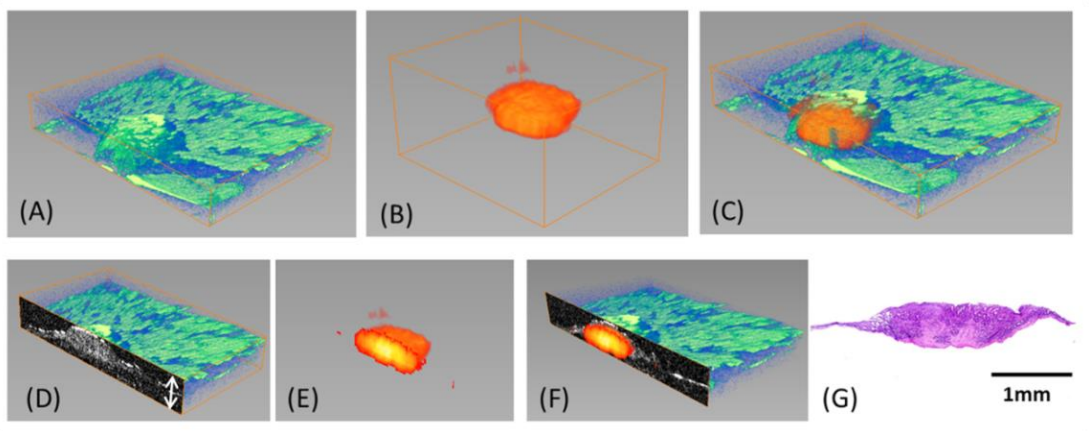

Figure 2. 3D OCT and FLOT images

(A) 3D OCT image (X×Y×Z=5×3×0.5 mm^3). (B) 3D FLOT image (X×Y×Z=3.8×3.3×2 mm^3). (C) 3D OCT and FLOT fused image. (D) Cross-sectional OCT images. (E) Cross-sectional FLOT images. (F) 2D OCT and FLOT fused image. (G) Corresponding histology

These two 3D images agree well as shown in the fused 3D image (Fig. 2C). Fig. 2(D) and 2(E) show the corresponding cross-sectional OCT and FLOT images. Due to the scattering effect, OCT signals attenuate at deeper regions, while FLOT can provide

better depth information as shown in Fig. 2(F). Both data agree with the corresponding histology (Fig. 2G). These results clearly demonstrate the feasibility of OCT and FLOT for co-registered tissue morphology and molecular information, and the capability of FLOT to visualize the depth information of subsurface tumors.

6.3.1 Structural and Molecular Biomarkers

From Fig. 3(A), the colon tumor shows enhanced light attenuation compared to normal regions. The red arrow indicates the landmark we can use to co-register tissue scattering coefficient (μ_s) map with the top-down view of FLOT 3D image shown in Fig. 3(C). Our findings are consistent with previous animal study [168] and clinical observations of reduced OCT scattered light in adenomatous polyps of the human colon [238]. Another observation is the heterogeneity in the tumor region [239] as shown in Fig. 3(A). Fig. 3(C) shows the top-down view of FLOT 3D image using fluorescent contrast agent. Colon adenomas show enhanced fluorescence compared to normal regions. Depth distribution of the contrast agent can be seen in Fig. 2(E). Fig. 3(D) shows fused scattering coefficient and fluorescence image based on the landmark indicated by the red arrow. These parameters will indicate the level of molecular activities, size, and depth of invasion of the tumor.

6.3.2 Parameters for tumor size measurement

OCT/FLOT images provide the parameters to differentiate neoplastic lesions from normal tissues. We first applied these parameters to estimate the size of tumors to differentiate

different stages of neoplastic lesions. For OCT, since the scattering coefficient (μ_s) map (Fig. 3A) is heterogeneous, in order to find the optimal threshold value for tumor size

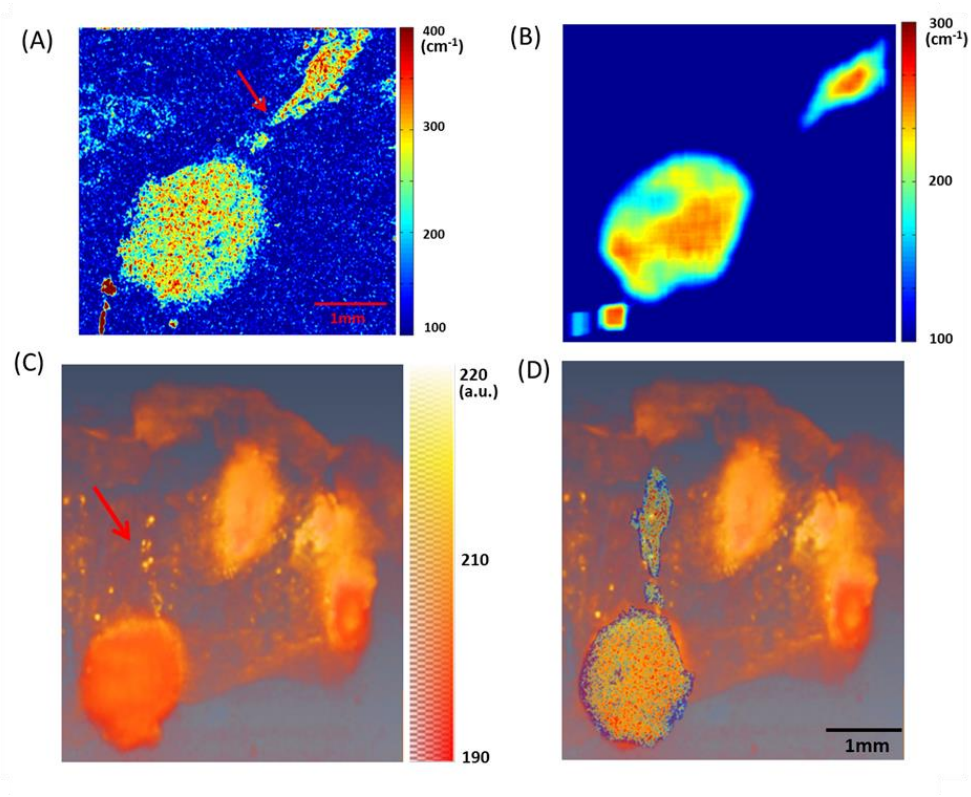

Figure 3. Structural and Molecular Biomarkers
(A)Tissue scattering coefficient (μ_s: cm^{-1}) image. (B) Tissue scattering coefficient (μ_s: cm^{-1}) image after sliding filtering. (C) Top view of FLOT 3D image using cathepsin B-sensitive fluorescent contrast agent. Relative enzyme activities are higher around tumor areas than the surrounding normal tissue. (D) Fused scattering coefficient and fluorescence image.

estimation, a sliding neighborhood operation with 100-by-100 sliding blocks was applied to the scattering coefficient (μ_s) map (1360×1240). The scattering coefficient (μ_s) map after sliding neighborhood operation is shown in Fig. 3(B). Then from the intensity profiles along both X and Y directions, the full-widths of the intersections with different threshold values were estimated as the tumor size (i.e., all the pixels with the same Y position were summed up when we calculate the intensity profile along X direction). The different threshold values were derived by the following equation: $(I_{max} - I_{min}) \times H\% + I_{min}$, where

I_{max} is the maxium value and I_{min} is minimum value or the background value on the each specific intensity profile. $H\%$ are the different percentages that we can use to calculate different threshold values and the values for $H\%$ are set 30%, 40%, 50%, 60% and 70% in this study. The tumor diameter was determined by averaging two dimensional measurements (X and Y). Finally the absolute value of error function (the absolute diameter or thickness difference) $E = \frac{\text{Measure}-\text{Histoloy}}{\text{Histology}}$ was used to judge the accuracy of the measurement for different threshold values. Tissue scattering coefficient (μ_s) maps were obtained on 12 samples from 6 different animals. The statistics of the 12 samples with different threshold values is shown in Fig. 4(A). 60% threshold provided the best result (E = 0.323±0.057). Tumor thickness was determined from OCT cross-sectional image as shown in Fig. 2(D) (indicated by the white double-head arrow). For FLOT, we used the same protocol to determine the optimal threshold in tumor sizes in XYZ dimensions. The tumor diameter was determined by averaging two dimensional measurements (X and Y) for different threshold values. Tumor thickness was determined from the tumor size in Z dimension for different threshold values. As shown in Fig. 4(B), 50% threshold gave the best measurement (E = 0.131±0.032) for tumor diameter but not the optimal measurement (E = 0.780±0.191) for tumor thickness, while 60% threshold provided a comparatively good estimation (E = 0.135±0.021) for tumor diameter but a markedly better measurement (E = 0.551±0.102) for tumor thickness estimation. Thus we chose 60% threshold for FLOT datasets. Using the optimal thresholds we chose, the sizes from measurements were then plotted together with histology data which served as the gold standard as shown in Fig. 5. FLOT provides a more accurate estimation in tumor diameter (E = 0.135±0.021) but relatively worse in thickness estimation (E = 0.551±0.102) due to the inverse reconstruction nature of FLOT. OCT gives a

better estimation in depth direction (E = 0.264±0.045) since there is colon serosa below tumor which scatters more light back than tumor tissue, and serves as the lower tumor boundary.

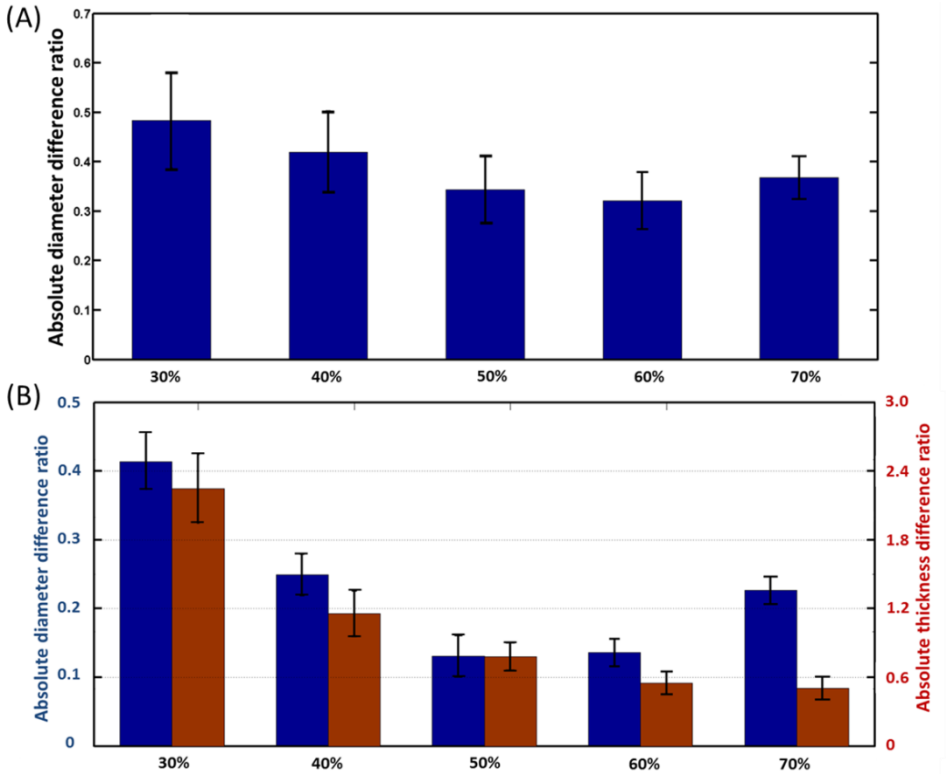

Figure 4. Threshold determination

(A) Average absolute diameter difference ratio for OCT with different threshold (n=12, from 6 different animals). (B) Average absolute diameter and thickness difference ratio for FLOT with different threshold (n=12, from 6 different animals).

While we can notice that OCT signals attenuate at deeper regions, the tumor thickness is mainly based on tissue surface height (with respect to a fixed reference position), and in our case, the tumor region is comparably thicker than the normal tissue. That may result in more accurate thickness estimation from OCT in this experiment, but for *in vivo* case, the accuracy of tumor thickness estimation may not be that precise. Even though FLOT's estimation is not ideal for tumor thickness, it is still able to estimate the depth within certain accuracy ranges(~50%), which can provide additional information compared to 2D fluorescence

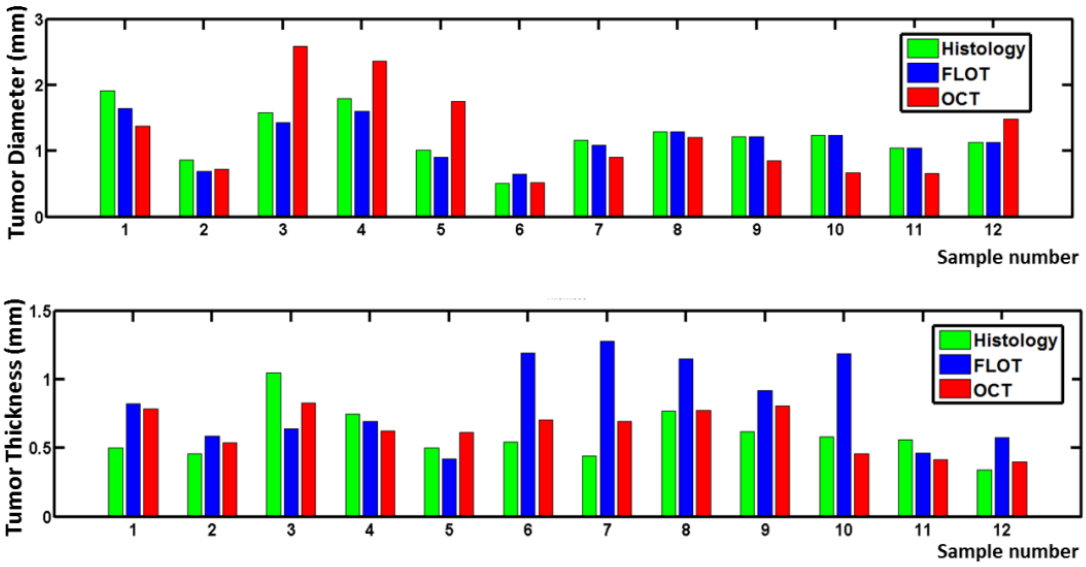

Figure 5. Diameter and thickness from FLOT and OCT compared to histology (n=12, from 6 different animals).

imaging method or simple white light examination. For diameter estimation, since we used tissue scattering coefficient (μ_s) to determine the size, both the anisotropy and heterogeneity of the tumor region may result in inaccurate (E = 0.323±0.057) measurement compared to the actual size of the tumor determined by histology. By taking advantage of the two imaging methods, there is a great potential to obtain tumor sizes in all dimensions in order to differentiate different stages of neoplastic lesions. We tried to perform the histology in the middle line of each tumor, so the diameter and thickness data should be able to reflect the dimensions of each tumor. However, using markers will definitely provide better correlation between two imaging methods and histology and more accurate results [240].

6.3.3 Parameters for tumor detection

To quantify the parameters mentioned above in differentiating colon tumor and tissues nearby tumor, tissue scattering coefficient (μ_s) and relative enzyme activity were determined by averaging the values of randomly picked 5×5 pixels region of interest (ROI) in tumor and

normal tissues near tumor on 17 samples from 6 different animals (the tumor area was determined using the optimal threshold derived in *Section 3.2*). There are in total 68 datasets (2 datasets were taken from each tumor region and 2 datasets were taken from each normal tissue near tumor.). As shown in the left part of Fig. 6, the tissue scattering coefficient (μ_s) of the tumor region is statistically larger than the control group ($P<0.001$). The relative enzyme activity of tumor region as shown in the right part of Fig. 6 is statistically larger than that of normal tissue as well ($P<0.001$). The tissue scattering coefficient (μ_s) is relatively lager than the values previously reported [116, 241]. This increase may originate from formalin fixation since it has been reported that formalin fixation can result in increasing scattering coefficient due to the cross-linking of proteins creating a more highly scattering media [242, 243].

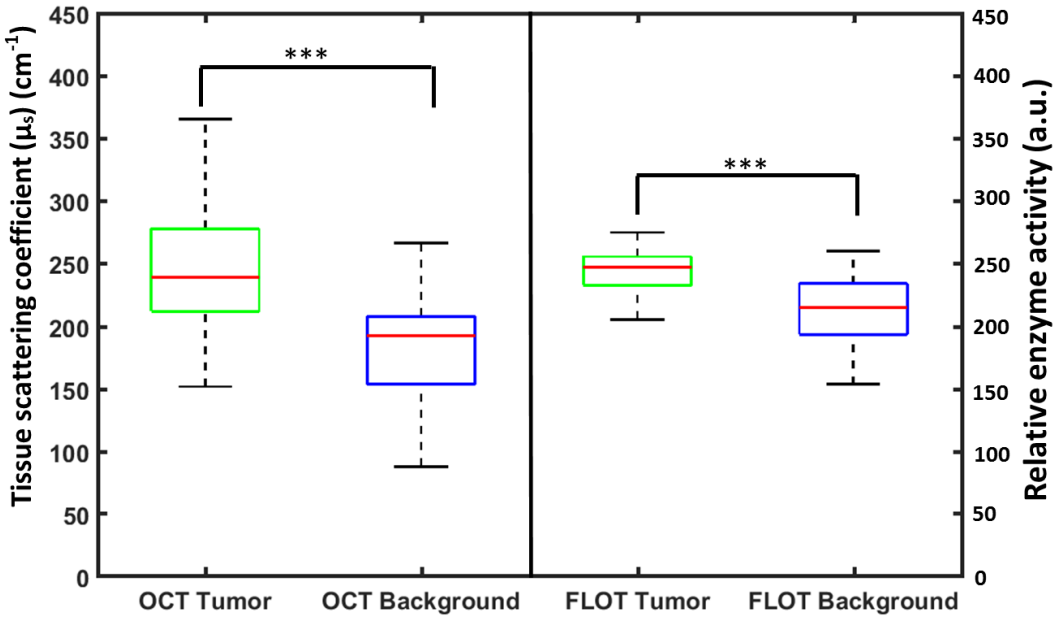

Figure 6. Parameters for tumor detection

Statistics of tissue scattering coefficient (μ_s) and Relative enzyme activities in tumor tissue and normal tissue near tumor. The tissue scattering coefficient (μ_s) of the group of tumor tissue (n=34, from 6 different animals) was statistically ($P<0.05$) bigger compared to control group (normal tissue near tumor : n=34, from 6 different animals). The relative enzyme activity in the group of tumor tissue was statistically ($P<0.05$) larger than control group.

6.3.4 Diagnostic accuracy of combined imaging modalities

The tissue scattering coefficient (μ_s) and relative enzyme activity were determined by averaging the values of randomly picked 5×5 pixels ROI in tumor and normal tissue near tumor on 17 samples from 6 different animals. There are in total 68 datasets (2 datasets were taken from each tumor region and 2 datasets were taken from each normal tissue near tumor). Relative enzyme activity and tissue scattering coefficient (μ_s) from the datasets are plotted in X and Y dimensions respectively as shown in Fig. 7(A). LDA found the best separation of the two groups (tumor and normal tissues near tumor) as shown in Fig. 7(A). Fig. 7(B) shows the ROC curves for diagnosis using tissue scattering coefficient only and relative enzyme activity only, and the corresponding optimal diagnostic sensitivity and specificity using the combined criteria. The optimal sensitivity (specificity) for scattering coefficient only is 76.47% (82.35%), relative enzyme activity only is 85.29% (70.59%), and combined criterion is 82.35% (82.35%). Combined criterion gives the optimal diagnosis (i.e., the shortest distance to ideal diagnosis 100% (100%)). Fluorescence molecular imaging can achieve high sensitivity in detecting early cancer, however, has limited specificity due to confounding factors such as inflammation. On the other hand, OCT is less sensitive to early neoplastic changes before significant structural alterations occur, but has high specificity to rule out the non-neoplastic regions. Combined together, fluorescence molecular imaging and OCT can provide complementary information for more accurate detection and characterization of early neoplasia.

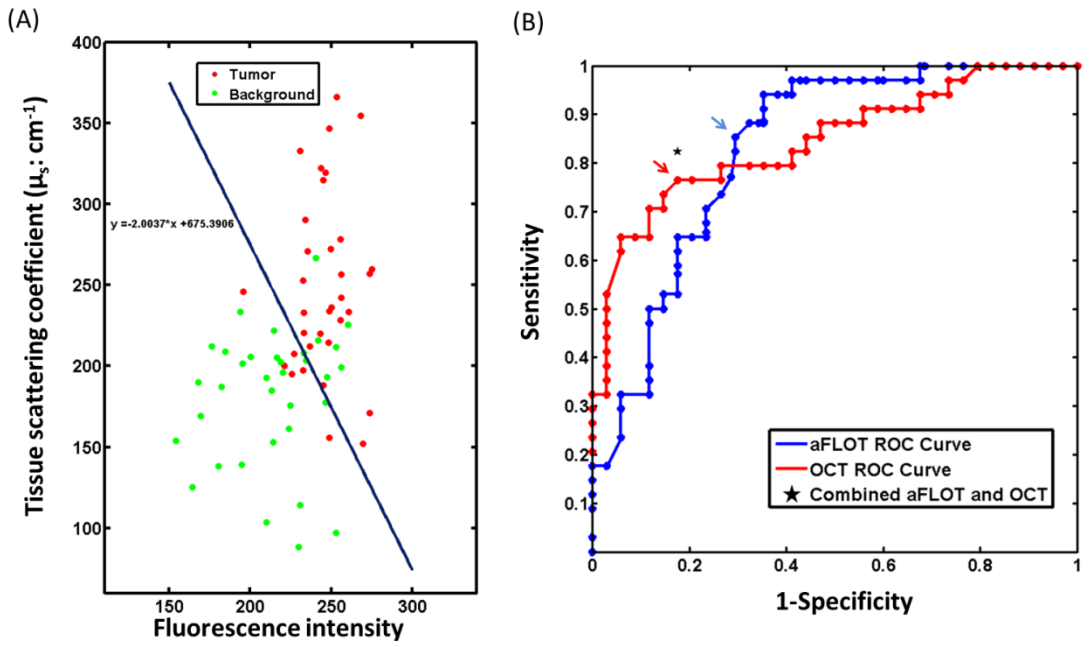

Figure 7. Diagnostic accuracy of combined imaging modalities

(A) LDA for classification of tumor tissue and normal tissue near tumor;(B) ROC curves for using tissue scattering coefficient only, relative enzyme activity only, and combined criteria. The arrows indicated the optimal threshold for OCT and FLOT. Combined criterion gives the optimal diagnosis (i.e., the closest distance to ideal diagnosis 100% (100%)).

To validate the combined criteria, another 68 datasets were collected from the 17 samples, as the validation data set, to determine the sensitivity and specificity of the criteria value in an independent study. With the diagnostic threshold of $y = -2.0037 \times x + 675.3906$ derived in Fig. 7(A), the sensitivity (specificity) for validation data was 88.23% (82.35%) compared to 79.41% (82.35%) for OCT only and 85.29% (73.52%) for FLOT only. We should notice that cathepsin B-sensitive contrast agent used in the paper may not be optimal for tumor cell targeting. FLOT is a general method and can work with other contrast agents. In the future, cyclic Arg-Gly-Asp (RGD) [244], folate receptor-α [245] and affinity peptide [246] can be considered to further improve the diagnostic accuracy.

6.4 Conclusion

We investigated a multi-modal optical imaging approach combining high-resolution OCT and depth-resolved high-sensitivity FLOT for structural and molecular imaging. Quantitative structural (scattering coefficient) and molecular (relative enzyme activity) parameters from OCT/FLOT images were derived for multi-parametric analysis. In the paper, we applied the single scattering model to estimate the extinction coefficient. The multi-scattering model included the effects of single scattering, multiple scattering, and the Gaussian beam propagation [236] and can present a more precise estimation about the tissue scattering coefficient while more difficult to fit. To classify the tissue types, the simpler single scattering model has been used to extract the slope of the logarithmic axial depth profile [168, 232-235]. In the future, we will investigate the multi-scattering model and get a more quantitative tissue scattering coefficient. To quantify the measurement error from FLOT, one glass capillary was filled with 1 μM Cy5.5 solution (Cyanine5.5 azide, Lumiprobe Corporation) and inserted into an agar phantom. The agar phantom was fabricated with 1.5-g agar powder, 2.5-mL 20% intralipid solution, and 49-mL PBS buffer. The fluorescence values from FLOT were randomly picked from 12 5 x 5 pixels sites of the capillary. In theory, the fluorescence values from different sites of the capillary should be the same. The fluorescence values are 228.2±0.6. The variance of the fluorescence values from FLOT is negligible. For OCT, the scattering map is attached. The tissue scattering coefficient (μ_s) are 169.9±3.5 /cm. The variance may come from the inhomogeneous distribution of the intralipid in the agar phantom.

This multi-modal imaging method has demonstrated the feasibility for more accurate diagnosis with 88.23% (82.35%) for sensitivity (specificity) which gives the optimal diagnosis compared to each individual imaging modality. This new multi-modal imaging technology is able to provide comprehensive structural and molecular parameters for better assessment of subsurface lesions. Therefore, such an imaging technology could detect subsurface cancers and pre-cancers to improve the diagnostic sensitivity, monitor the neoplastic progression underneath the surface, and assess the efficacy of ablative therapies. Integrated OCT and line-scan FLOT has been demonstrated through a dichroic mirror [94]. In the future, we will combine high-resolution OCT and depth-resolved high-sensitivity FLOT into one imaging system for more studies on different disease models, which can provide co-registered structural and molecular information of tissues simultaneously. The two imaging modalities could be further integrated into a functional endoscopy system using microelectromechanical system (MEMS), GRIN cylindrical lens (GRINTECH. Inc) and imaging fiber bundle [247]. Since Monte Carlo modeling and regularization term are applied in reconstructing FLOT images, it is time-consuming and cannot provide the reconstructed image in real time especially for a system with high source–detector density. But with the advent of the computer speed and new regularization methods introduced [248], the time needed for image reconstruction in FLOT could be alleviated dramatically.

Chapter 7: Real-time monitoring of microdistribution of antibody-photon absorber conjugates during photoimmunotherapy *in vivo**

7.1 Introduction

Photoimmunotherapy (PIT) is an emerging low side effect cancer therapy based on a targeted monoclonal antibody-photo absorber conjugate (APC) [mAb conjugated with a near-infrared (NIR) phthalocyanine dye (IR700)] that induces rapid cellular necrosis after exposure to NIR light [249]. IR700 is not only fluorescent, and thus can be used as an imaging agent, but it also is phototoxic, serving as an imaging theranostic. When exposed to intense levels of NIR light, the conjugate becomes lethal, but only to those cells to which it is bound [249]. NIR light exposure can lead to rapid, target-selective necrotic cell death *in vitro* and effective tumor shrinkage on animal models *in vivo* [249]. PIT induced highly selective cancer cell death, while leaving most of the tumor blood vessels unharmed, leading to an effect termed super enhanced permeability and retention (SUPR), which significantly improved the effectiveness of anticancer drugs [42]. However, very little is known about how deep tumor cells and vasculature respond while perivascular cancer cells are destroyed via PIT.

---

* Part of the contents in this chapter is reproduced from "Tang, Q. et al., Real-time monitoring of microdistribution of antibody-photon absorber conjugates during photoimmunotherapy in vivo, *Journal of Controlled Release*, 260(154-163), 28 August 2017." with permission.

Although single administration of the therapy was effective, tumor recurrences were observed in treated animals because of inhomogeneous mAb−IR700 distribution in the targeted tumor. The mAb−IR700 conjugate remains in the circulation system longer than nontargeting small molecule photosensitizers. Thus, the unbound mAb−IR700 can redistribute into the remnant target tumor after initial NIR light irradiation [250]. Fractionated administration of the mAb panitumumab−IR700 conjugate, followed by systematic, repeated NIR light irradiation to the tumor, was shown to be a highly effective tumor treatment because of the redistribution of antibody over time into the remnant tumor under the guidance of the IR700 fluorescence signal [250]. Real-time monitoring of theranostic agent distribution and its therapeutic effects, including cellular necrosis within the tumor microenvironment, will be critical for further understanding the PIT/SUPR mechanism and optimizing the effectiveness of treatment.

The current approach for monitoring APCs fluorescence, macroscopic fluorescence reflectance imaging, lacks the resolution and depth information to show mAb-IR700 distribution *in situ* [42]. Histological analysis reveals intratumor APC distribution is inhomogeneous. However, it is invasive and terminal. Real-time change of the microdistribution of APCs in different locations within the tumor after PIT has not been studied *in vivo*. Here, we investigated the microdistribution of APCs at different locations (e.g., tumor surface vs. deep tumor) during and after *in situ* and *in vivo* PIT using fluorescence laminar optical tomography (FLOT), a minimally invasive two-channel fluorescence fiber imaging system and a high resolution two-photon microscope (TPM) with a 1 mm microprism.

7.2 Materials and methods

7.2.1 Reagents

Water soluble, silica-phthalocyanine derivative, IRDye 700DX NHS ester was obtained from LI-COR Biosciences (Lincoln, NE, USA). Panitumumab, a fully humanized IgG_2 mAb directed against epidermal growth factor receptor (EGFR) was purchased from Amgen (Thousand Oaks, CA, USA). All other chemicals used were reagent grade.

7.2.2 Synthesis of IR700-conjugates

Conjugation of dyes with mAbs was performed according to previously used methods [249]. In brief, panitumumab (1.0 mg, 6.8 nmol) was incubated with IRDye 700DX NHS ester (66.8 μg, 34.2 nmol) in 0.1 M Na_2HPO_4 (pH 8.6) at room temperature for 1 h. The mixture was purified with a Sephadex G25 column (PD-10; GE Healthcare Life Sciences, Pittsburgh, PA, USA). The protein concentration was determined with the Coomassie Plus protein assay kit (Thermo Fisher Scientific, Waltham, MA, USA) by measuring the absorption at 595 nm with UV-Vis (8453 Value System; Agilent Technologies, Santa Clara, CA, USA). The concentration of IR700 was measured by absorption at 689 nm to confirm the number of fluorophore molecules per mAb. The synthesis was controlled so that an average of two IR700 molecules was bound to a single antibody. We abbreviate IR700 conjugated to panitumumab as pan-IR700. As a quality control for the conjugate, we performed sodium dodecyl sulfate-polyacrylamide gel electrophoresis (SDS-PAGE). Conjugate was separated by SDS-PAGE with a 4-20% gradient polyacrylamide gel (Life Technologies, Gaithersburg, MD, USA). A standard marker (Crystalgen Inc.,

Commack, NY, USA) was used as a protein molecular weight marker. After electrophoresis at 80 V for 2.5 h, the gel was imaged with a Pearl Imager (LI-COR Biosciences, Lincoln, Nebraska, USA) using a 700 nm fluorescence channel. We used diluted panitumumab as a control. The gel was stained with Colloidal Blue staining to determine the molecular weight of conjugate.

7.2.3 Cell culture

EGFR-expressing A431 (epidermoid carcinoma cells)-green fluorescent protein (GFP) cells stably expressing GFP were established by Dr Kobayashi's laboratory. Cells were grown in RPMI 1640 medium (Life Technologies, Gaithersburg, MD, USA) supplemented with 10% fetal bovine serum and 1% penicillin/streptomycin (Life Technologies) in tissue culture flasks in a humidified incubator at 37 °C at an atmosphere of 95% air and 5% carbon dioxide [41].

7.2.4 Animal and tumor models

All *in vivo* procedures were conducted in compliance with the *Guide for the Care and Use of Laboratory Animal Resources* (1996), US National Research Council, approved by the Institutional Animal Care and Use Committees (IACUCs) at the University of Maryland and NIH. Six-to-eight-week-old female homozygous athymic nude mice were purchased from Charles River (NCI-Frederick, Frederick, Maryland). Two million A431-GFP cells were subcutaneously injected in the right and left dorsum of each of the mice. Tumor volumes were based on caliper measurements and were calculated using the following formula: tumor volume = length × width^2 × 0.5.

Mice were monitored daily for their general health and tumor sizes. Tumors reaching approximately 100 mm^3 in volume were selected for study [41, 251].

7.2.5 Treatment regimens

We used pan-IR700 as the imaging and toxic agent for A431-GFP tumor bearing mice. Tumor bearing mice were randomized into 2 groups of at least 5 animals per group for each imaging experiment (e.g., two-channel fluorescence needle imaging, two-photon micro-prism imaging, and two-photon tumor surface imaging experiments are treated as three imaging experiments). 24 hours after i.v. injection of 100 μg of pan-IR700 via the tail vein, 50 J/cm^2 NIR light was administered at group 1 while group 2 (without NIR light) was used as a control.

7.2.6 Imaging

All mice were anesthetized with 2% isoflurane mixed in O_2 and were then immobilized using a customized stereotaxic frame. Body temperature was maintained at 37 °C with a heating blanket. A small incision was performed to remove the skin covering the tumor to allow for imaging. After imaging, the mice were euthanized and tumors were extracted. The tumors were fixed using formalin in place. *Ex vivo* fluorescence imaging and histology were performed for A431-GFP tumors and control tumors.

7.2.6.1 Fluorescence laminar optical tomography system

The FLOT system is similar to that reported previously [80, 167, 204]. Pigtailed 637-nm laser diodes was used as the light sources (LP637-SF70, Thorlabs Inc.) to illuminate the samples. The tumor was imaged by FLOT system during and 2 hours after NIR

light treatment every 10 minutes. Oregon green labeled dextran with 70000 MW was injected i.v. before NIR light administration to indicate the vascular distribution of the tumors.

7.2.6.2 Two-channel fluorescence needle system

Fig. 4A illustrates the schematic of the two-channel fluorescence imaging system. The system is equipped with a two-channel fiber bundle (FIGH-30-850N, Myriad Fiber Imaging Tech., Inc., Dudley, MA, USA). It provides two imaging fields of view (FOVs) of ~0.8 mm with 30,000 pixels each and relays the images from the tumor surface and deep tumor at the distal end of the fiber bundle back to the focal plane of the objective. The system utilizes a 637 nm laser diode as its light source, which is coupled with a single-mode fiber to shape its light beam. A diffuser is used to make the light more uniform. The light is collimated by an objective and goes through a dichroic mirror (650 nm, single-edge dichroic beamsplitter; DMLP650R; Thorlabs, Inc., Newton, NJ, USA). The light is then coupled to the two-channel fiber bundle system by an objective. A custom-built motorized 3D microstage facilitates accurate light coupling between the objective and the two-channel fiber bundle. The emitted fluorescent light is collected back through the fiber bundle, objective, dichroic mirror, a 665 nm longpass emission filter, and finally imaged on a charge coupled device (CCD) camera (PIXIS1024, Princeton Instruments, Trenton, NJ, USA). For tumor imaging, after aligning the two-channel fiber bundle to the objective, one channel of the fiber bundle probe was gently inserted into the tumor of the anesthetized mouse by slowly moving the animal stage up and using stereotaxic coordinates [173]. Special attention was paid to avoid damaging large blood vessels

during this procedure, and minor bleeding was cleared by flushing with saline solution [252]. The other channel of the imaging fiber bundle was placed at the surface of the tumor.

The NIR LED used for the PIT treatment in the experiments has a wavelength spectrum of 680-700 nm (Tech-LED, Marubeni America Corp., Santa Clara, CA, USA) and irradiates for ~20 minutes to deliver a dose of ~50 J/cm^2 light to the tumor [250, 253]. The LED spectrum overlaps the detection filter spectral range. To record the IR700 fluorescence signal change during and after PIT, the data acquisition protocol is as follows: one image was taken before turning on the LED, then, in the first 20 minutes, each image was taken after every 2 minutes of tumor LED exposure. After 20 minutes of LED exposure, the PIT treatment was completed and, in the next 70 minutes, one image was taken every 2 minutes to record the tumor's post-treatment changes. The control group received no LED exposure, but during 90 minutes (the same time that the exposed group was treated and observed) one image was taken every 2 minutes. The driver current was set at 100 mA for the laser diode and the exposure time was set at 1 s for the CCD camera during data acquisition.

7.2.6.3 The TPM system with a microprism

TPM, which allows the simultaneous absorption by each fluorophore molecule of two photons in a single quantum event, offers many advantages over conventional imaging techniques. It has become a powerful tool for studying biological function in living tissues [84-88]. Microprisms have been used with the TPM for *in vivo* multilayer cortical imaging in mice [254]. The lab-customized two-photon system utilized a Ti:sapphire laser (Mira 900-F, Coherent Inc., Santa Clara, CA, USA) operating at 790

nm wavelength and 120 fs pulse width. A 20X water immersion objective (Olympus Corporation of the Americas, Center Valley, PA, USA) was employed for focusing the excitation beam into tissue samples and to collect the two-photon excited fluorescence signals. A dichroic mirror (760 nm, single edge dichroic beamsplitter; T760LPXXR-UF3; Chroma Technology Corp, Bellows Falls, VT, USA) was applied to separate the excitation laser and fluorescence signals. The fluorescence signals were further separated into two channels by another 550 nm dichroic beamsplitter, followed by an emission filter (525±39 nm and 716±42 nm for the GFP signal in the green channel and the IR700 signal in the red channel, respectively) and a photomultiplier tube (PMT) (H7422P-40 for the green channel and H7422P-50 for the red channel, Hamamatsu Corporation, Bridgewater, NJ, USA).

For *in vivo* imaging of the tumor surface, the skin covering the tumor was removed and the tumor was exposed under the TPM objective lens. For *in vivo* imaging of deep tumor, a 1×1 mm^2 right-angled microprism (OptoSigma Corporation, Santa Ana, CA, USA) coated with anti-reflection coatings to minimize surface reflections was fully inserted into the mouse tumor. The prism surface was then cleaned with a hemostatic sponge and flushed with saline solution. A customized glass chamber window was placed on the prism to reduce artifacts from the animals' heartbeats and respirations, and to hold the water used to immerse the 20X objective lens (Fig. 6A). The FOV per frame is ~1×1 mm^2, which projected the images across different depths of the tumor's regions, from the tumor surface to deep tumor. We defined the area within 500 μm depth from the tumor surface as "tumor surface" (tumor_s) and the area beyond 500 μm depth from the tumor surface as "deep tumor"

(tumor_d). The 20X objective lens was finely tuned to focus at the plane based on GFP-expressing tumor cells adjacent to the vertical surface of the prism. The data acquisition protocol is the same as described in Section 7.2.6.2., except that GFP signal was also recorded.

7.2.6.4 Ex vivo fluorescence microscopy

To detect antigen-specific microdistribution in the tumor, fluorescence microscopy was performed. Tumor xenografts were excised from mice 24 h after injection of APC. Extracted tumors were frozen with optimal cutting temperature (OCT) compound (Sakura Finetek Japan Co., Ltd, Tokyo, Japan) and frozen sections (10 μm thick) were prepared. Fluorescence microscopy was performed using an Olympus BX61 (Olympus Corporation) with the following filters: excitation wavelength 460-490 nm and 590-650 nm, emission wavelength 510-550 nm and 665-740 nm for GFP and IR700 signal, respectively. Transmitted light differential interference contrast (DIC) images were also acquired.

7.2.6.5 Histopathologic evaluation

Tumor xenografts were excised from mice after experiments. Light microscopy with an Olympus BX61 (Olympus Corporation) was used to evaluate histological changes. Extracted tumors were placed in 10% formalin and serial 10 μm slice sections were fixed on glass slides with hematoxylin and eosin (H&E) staining.

7.2.7 Statistical analysis

No missing data are observed in this study. Descriptive statistics, such as mean and standard deviation, were calculated. A Student's t-test was used and statistical

analyses were carried out using MATLAB (The MathWorks Inc., Natick, MA, USA). Statistical significance is considered at $P = 0.05$.

7.3 Results

7.3.1 Characterization of antibody conjugated dye

As defined by SDS-PAGE, pan-IR700 and non-conjugated control panitumumab showed identical molecular weights, and fluorescence intensity was confirmed in the band of pan-IR700 (Fig. 4B).

7.3.2 In vivo *fluorescence imaging using FLOT system*

In the FLOT experiment, as illustrated in Fig. 1A, at 0 min, NIR irradiation was turned on and the IR700 fluorescence intensity dropped quickly at both tumor surface and deep tumor regions. After 20 min, the NIR light was turned off and the IR700 fluorescence intensity recovered quickly and achieved a bigger volume than the initial value (0 min), which can be explained by increased vascular permeability immediately after NIR-PIT. The change in fluorescence during and after PIT of the tumor was shown in Fig. 1B, a clear drop was shown at the first 20 minutes and then the intensity recovered after PIT treatment, while there was only a gradual decrease in controls (No PIT treatment).

Fig. 1C and Fig. D were the histograms of the pixel intensity before and 60 min after PIT treatment in the PIT-treated tumor and control tumor, we can notice that after PIT treatment, there were more pixels in the center. Since before treatment, most of the pixels either had very low values (no APCs) or high fluorescence values (near blood vessels), while after PIT treatment the APCs can penetrate to more areas and

distributed more homogeneously. Tumor before PIT shows a significant larger standard deviation (SD) than that of tumor 80 min after PIT.

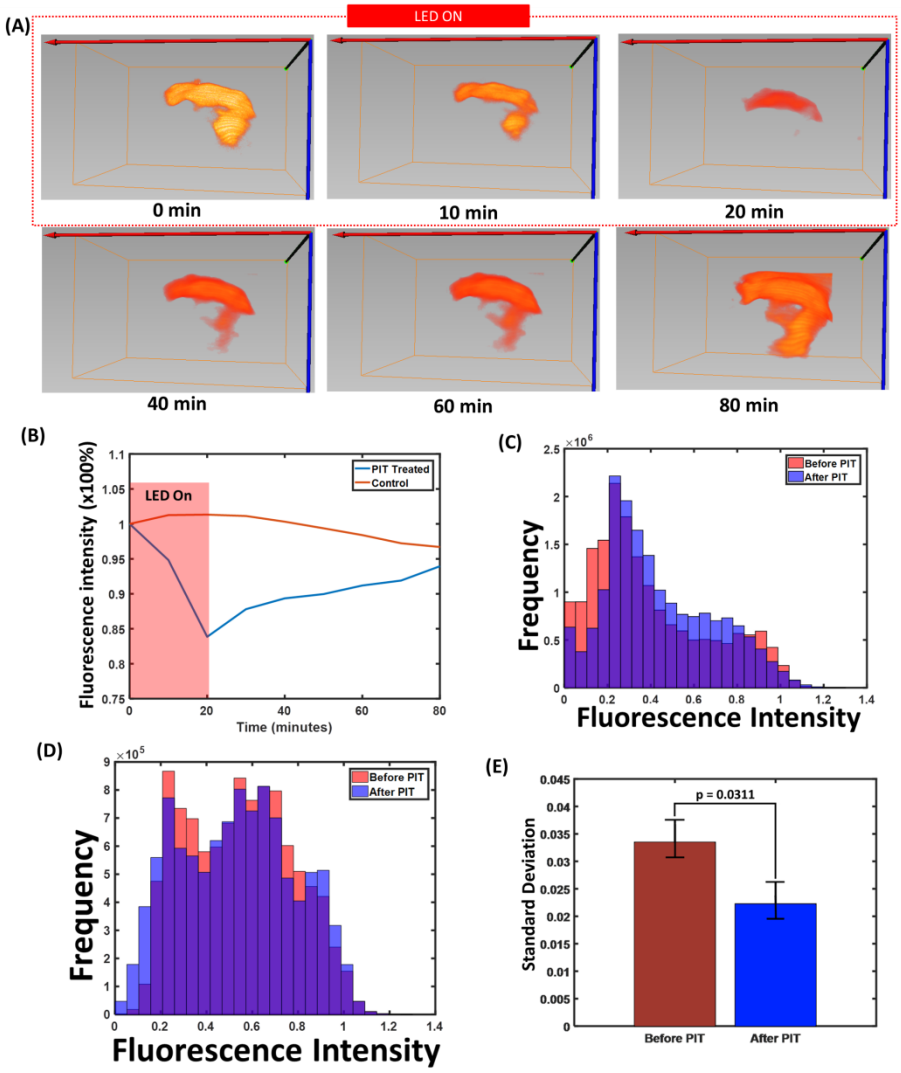

Figure 1. Recording from FLOT system

(A) 3D FLOT images of the micro-distribution of pan-700IR in tumor at different time points during and after PIT Treatment (X×Y×Z=3.7×3.4×2 mm3). (B) Representative normalized average IR700 fluorescence intensity of the tumor during and after PIT treatment. (C) Histograms of the pixel intensity before and 80 min after PIT in the tumor. (D) Histograms of the pixel intensity before and 80 min later in the control tumor (No PIT treatment). (E) Standard deviations (SDs) of the histograms of tumor before and 80 min after PIT treatment. Tumor before PIT shows a significant larger SD than that of tumor 80 min after PIT.

The IR700 fluorescence intensity was further averaged and normalized to the initial level (0 min) in the entire region of interest (ROI) from the tumor surface and deep tumor. The normalized IR700 fluorescence intensity clearly showed a greater drop in the tumor surface and a higher recovery in deep tumor (Fig. 2).

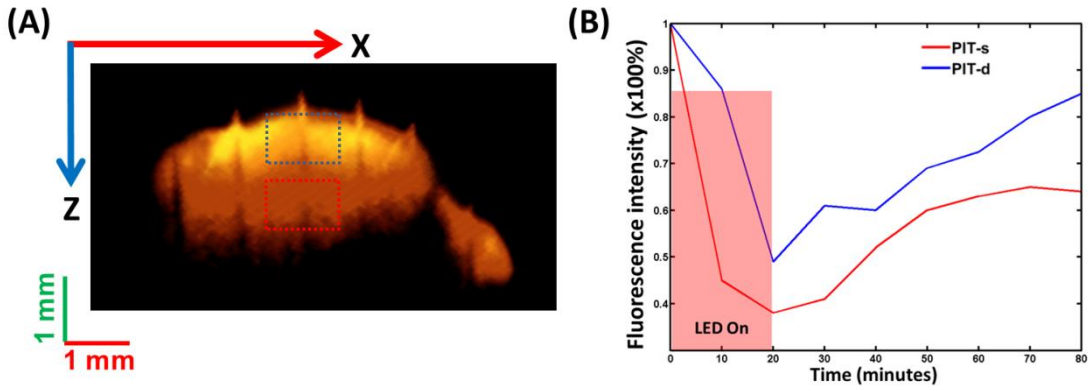

Figure 2. Recording from cross-sectional FLOT image

(A) Cross section of the 3D FLOT reconstructed of pan-700IR (Orange-red) distribution. Dashed blue and red squares indicate tumor surface and deep tumor respectively. (B)Representative normalized average IR700 fluorescence intensity of tumor surface and deep tumor during and after PIT treatment.

7.3.3 Calibration of the two-channel fluorescence needle system

The two-channel fluorescence needle system was initially used to image the 5 ug/mL IR700 PBS solution, which would be expected to have a homogeneous fluorescence distribution. The IR700 PBS solution's intensity profile can serve as a weight matrix to compensate for inhomogeneity from the fiber bundle and the imaging system (Fig. 3A). After compensation with the weight matrix, obtained above, fluorescence signals were plotted as a function of IR700 PBS concentration, and showed a good linear response with R^2=0.9393 (Fig. 3B). Fluorescence signals from the CCD were further plotted as a function of different IR700 concentrations in mouse blood, showing an excellent linear response with R^2=0.9959 (Fig. 3C and D). Before PIT, the two-channel fluorescence needle system was also used to measure the fluorescence intensity from the tumor surface, deep tumor, and normal tissues in the anesthetized mice (Fig. 4C). The tumors' surface showed a significantly higher IR700 fluorescence intensity value than that of the deep tumor (Fig. 4D). Tumors (average of tumor surface and deep tumor) showed a significantly higher IR700 fluorescence

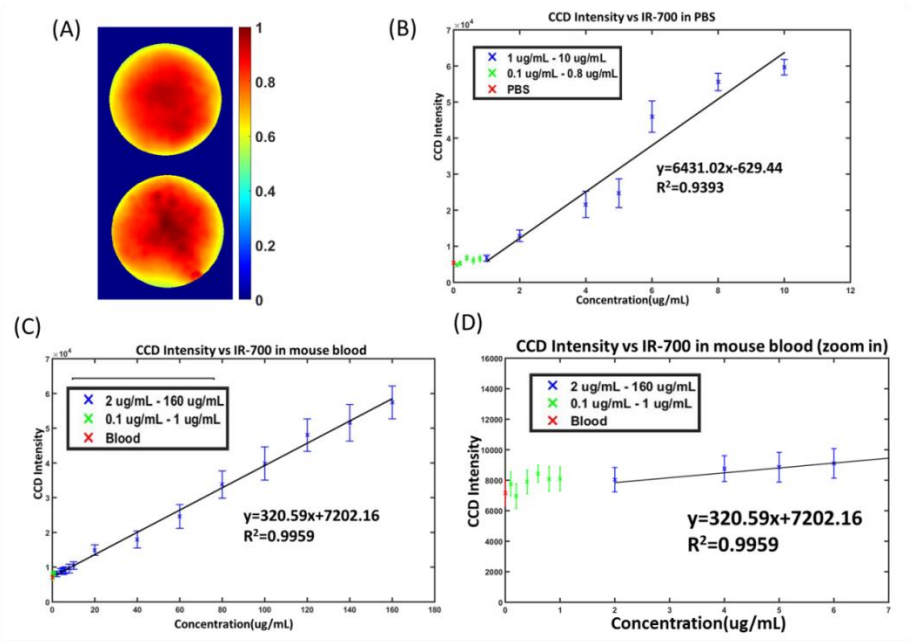

Figure 3. Image compensation and calibration

(A) Fluorescence distribution of two-channel system in IR700 PBS solution before calibration. (B) Relationship between fluorescence intensity and IR700 concentration in PBS (n=5). (C) Relationship between fluorescence intensity and IR700 concentration in mouse blood (n=5). (D) Zoomed relationship between fluorescence intensity and IR700 concentration in mouse blood.

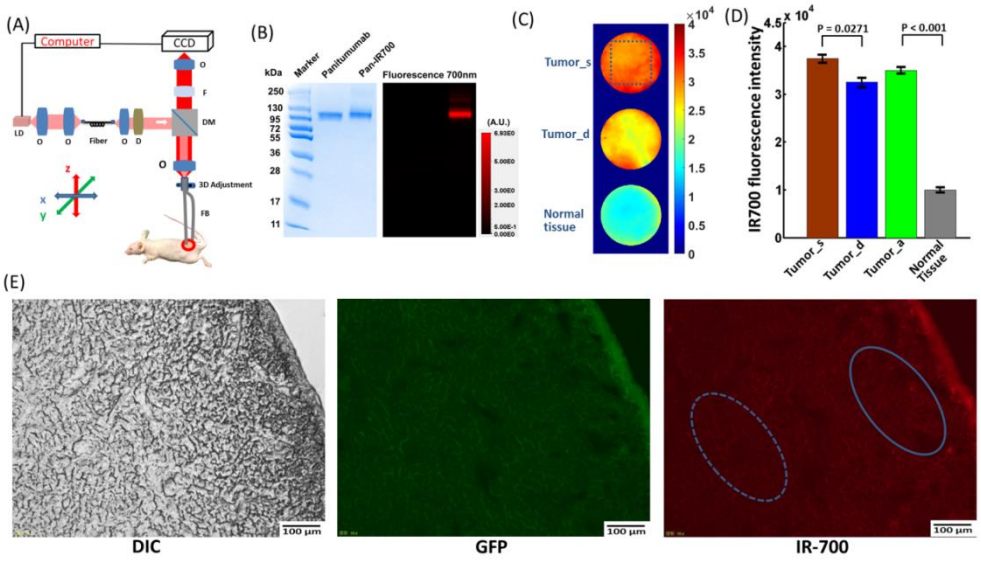

Figure 4. Two-channel needle system and fluorescence intensity

(A) Schematic of the two-channel needle system. O: objective lens; D: diffuser; F: filter; DM: dichroic mirror; FB: fiber bundle; LD: laser diode. (B) SDS-PAGE data of the pan-IR700 and non-conjugated control panitumumab. (C) Fiber bundle image of the tumor surface (Tumor_s), deep tumor (Tumor_d), and normal tissue before PIT. (D) IR700 fluorescence intensity value for the tumor surface, deep tumor, tumor average (Tumor_a), and normal tissue. The tumors' surface had a significantly higher fluorescence intensity value than that of the deep tumor ($p=0.0271$, n=5). Tumors showed significantly higher fluorescence intensity values than those of normal tissue ($p<0.001$, n=5). (E) Fluorescence microscopy of A431-GFP tumor. DIC image (left), GFP fluorescence (middle) and IR-700 fluorescence microscopic images (right) of A431-GFP tumors. The GFP fluorescence signal is relatively homogeneous, while the IR700 fluorescence intensity is higher in the tumor surface.

intensity value than that of normal tissue (Fig. 4D). Fig. 3E illustrates *ex vivo* GFP and IR700 fluorescence intensity. *Ex vivo* fluorescence microscopy confirmed a relatively homogeneous GFP fluorescence signal across the tumor surface and deep tumor, while IR700 fluorescence intensity is higher in the tumor surface (Fig. 4E).

7.3.4 In vivo *fluorescence imaging using the two-channel fluorescence needle system*

At 0 min, NIR irradiation was turned on and the IR700 fluorescence intensity dropped quickly both at the tumor surface and in deep tumor regions, with larger decreases at

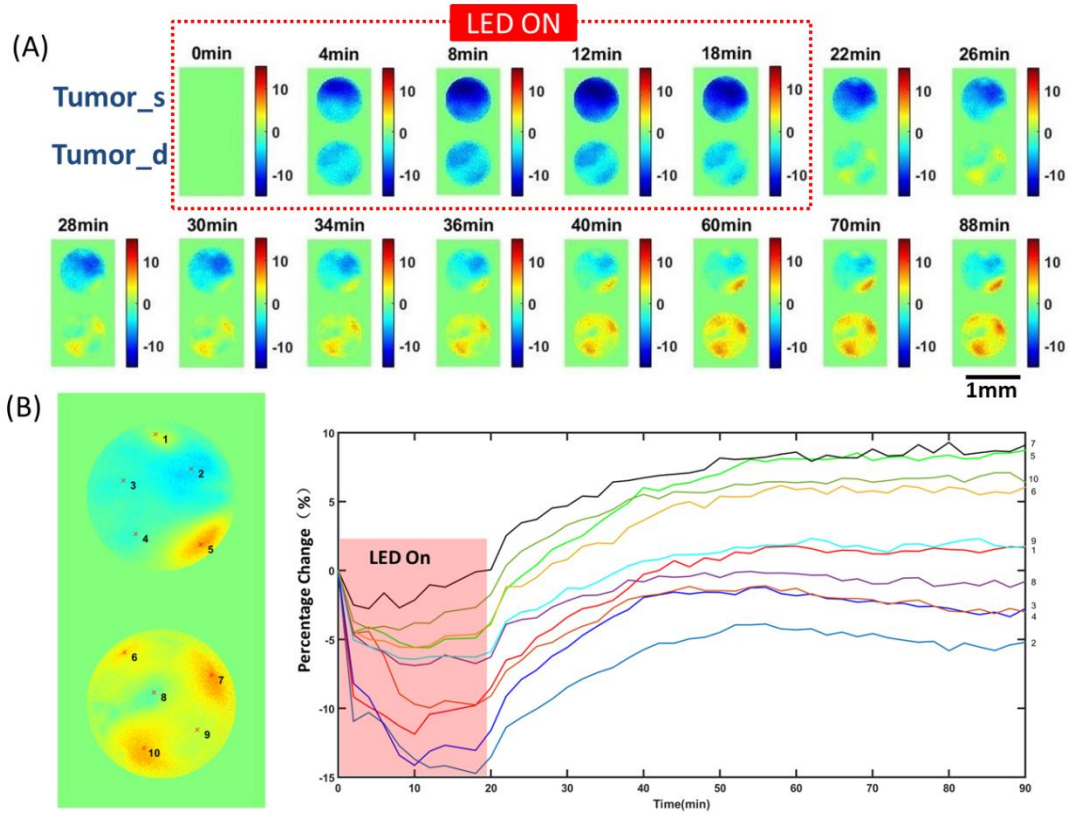

Figure 5. Recording from two-channel needle system

(A) Changes in fluorescence [ΔF/F (%), ordinate] of the tumor surface and deep tumor during and after PIT treatment imaged by the two-channel needle system. (B) Changes in fluorescence (ΔF/F (%), ordinate) of tumor surface and deep tumor during and after PIT treatment. The fluorescence signal was calculated from the positions (centered by the red marks in the left images with 5 × 5 pixels size) numbered accordingly.

the tumor surface. After 20 min, the NIR light was turned off and the IR700 fluorescence intensity recovered quickly to initial (0 min) levels. Some regions even increased to values higher than the initial levels, especially in the deep tumor (Fig. 5A). Different small regions (5 × 5 pixels) from both tumor surface and deep tumor were selected to show the changes in fluorescence during and after PIT, which can indicate the heterogeneity of the recovery in IR700 fluorescence intensity (Fig. 5B). Control experiments were performed on mice that did not receive NIR light exposure. There was only a small IR700 fluorescence intensity decrease throughout the measurement period, which may result from dye photobleaching without any fluorescence recovery (Fig. 6A).

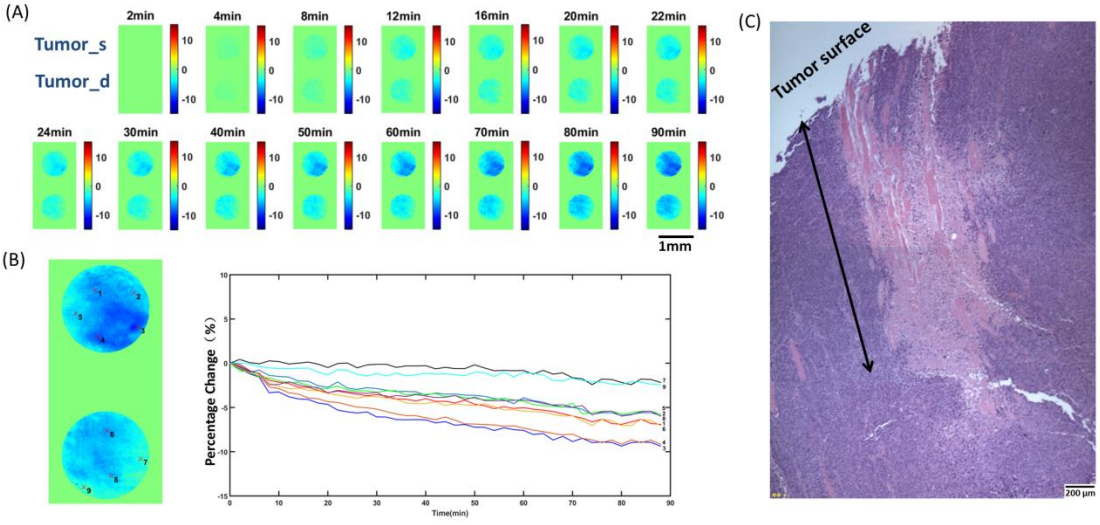

Figure 6. Two-channel needle recording from control mice

(A) Changes in fluorescence (ΔF/F (%), ordinate) of tumor surface and deep tumor in control mouse imaged by the two-channel needle system. (B) Changes in fluorescence (ΔF/F (%), ordinate) of tumor surface and deep tumor in control mouse. Fluorescence signal was calculated from the positions (centered by the red marks in the left images with 5 × 5 pixels size) numbered accordingly. (C) Histological specimens of A431 tumors from the control group. No obvious cell necrosis was observed in either tumor surface or the deep tumor. The double-arrow line indicates the imaging fiber bundle track ~1.6 mm below the surface.

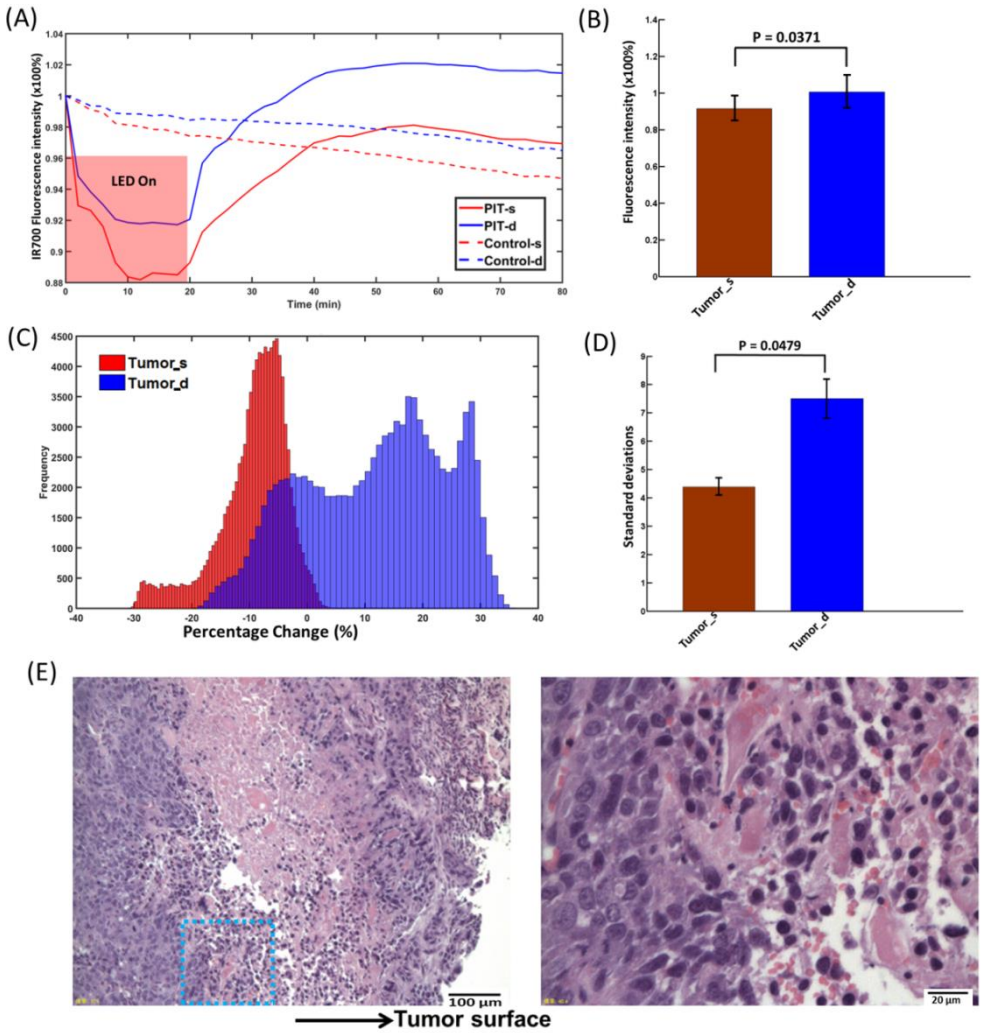

Figure 7. Normalized average fluorescence intensity changes

(A) Representative normalized average fluorescence intensity of tumor surface and deep tumor during and after PIT treatment compared with control. (B) IR700 fluorescence recovery value of the tumor surface and deep tumor. Deep tumors showed a significantly higher fluorescence recovery intensity value than that of the tumor surface ($p=0.0371$, $n=10$). (C) Histograms of the recovery value of the tumor surface and deep tumor. (D) Standard deviations (SDs) of the recovery value of tumor surface and deep tumor. Deep tumor shows a significant larger SD than that of tumor surface ($p=0.0479$, $n=6$). (E) Histological specimens of A431 tumors from the PIT-treated group. There is more cell necrosis in the tumor surface compared to the deep tumor. The image on the right side is the zoomed-in image from the blue square in the left image.

The IR700 fluorescence intensity was further averaged and normalized to the initial level (0 min) in the entire region of interest (ROI) from the tumor surface and deep tumor. The normalized IR700 fluorescence intensity clearly showed a greater

drop in the tumor surface and a higher recovery in deep tumor, while there was only a gradual decrease in controls (Fig. 7A). Recovery of IR700 fluorescence intensity in the deep tumors was significantly higher than that of the tumor surface and higher than the initial values for deep tumors (Fig. 7B). We also plotted histograms of the recovery values of tumor surface and deep tumor after PIT at 90 min. Deep tumors showed a multimodal shape and significantly greater standard deviations (SD) of the means (Fig. 7C and D).

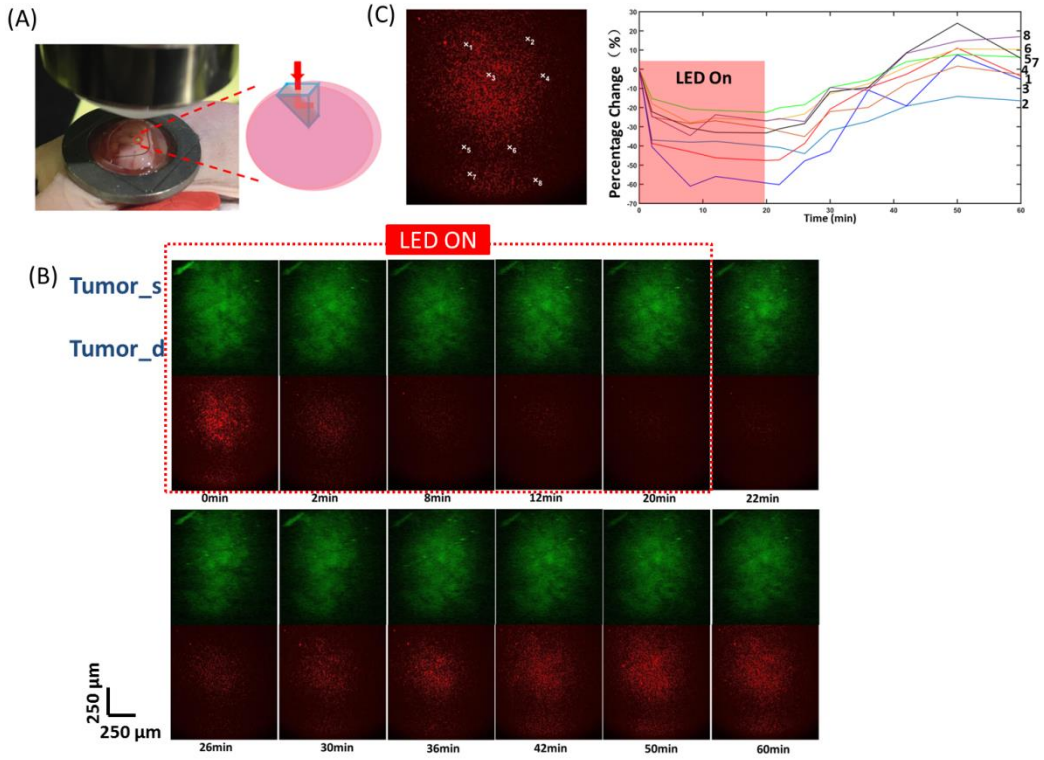

Figure 8. Recording from TPM microprism system

(A) Microprism placement in tumor for TPM imaging. (B) Tumor surface and deep tumor during and after PIT treatment imaged by TPM system.(C) Changes in fluorescence [ΔF/F (%), ordinate] of the tumor surface and deep tumor during and after PIT treatment. The fluorescence signal was calculated from the positions (centered by the white marks in the left images with 10 × 10 pixels size) numbered accordingly.

With H&E staining, the imaging fiber bundle track from the two-channel system showed an ~1.6 mm deep insertion into the deep tumor (Fig. 6A). There is more cell

necrosis in the tumor surface compared to the deep tumor (Fig. 7E). In the control tumor, there is no obvious cell necrosis observed in either the tumor surface or the deep tumor (Fig. 6C).

7.3.5 In vivo *fluorescence imaging using the TPM with microprism*

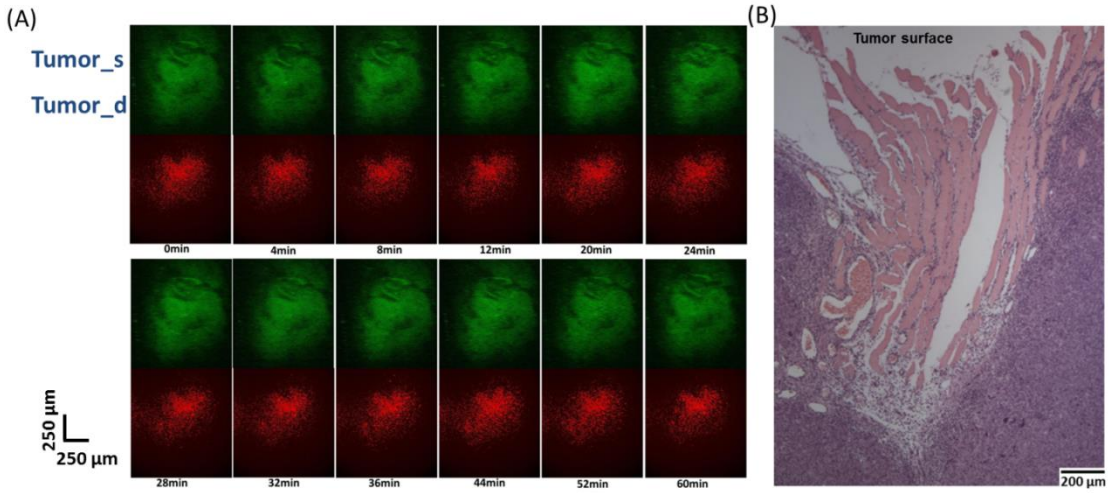

Figure 9. TPM microprism recording from control mice

(A) Tumor surface and deep tumor imaged by TPM with micro-prism system in control tumor. (B) Histological specimens of A431 tumors from the control group. No obvious cell necrosis was observed in either tumor surface or the deep tumor. The micro-prism track can be clearly seen ~1.4-1.7 mm below the surface.

To verify the results obtained from the two-channel fluorescence needle system, a microprism was gently placed inside the tumor to record the images across different depths of tumor regions from the tumor surface to the deep tumor (Fig. 8A). In the first 20 min with NIR irradiation, IR700 fluorescence intensity showed a significant drop in both tumor surface and deep tumor. Similar to the phenomenon observed before, after the NIR light was turned off, the IR700 fluorescence intensity began to recover (Fig. 8B). GFP fluorescence intensity only decreased with no recovery observed. Changes in IR700 fluorescence from randomly selected areas showed a

greater drop in the tumor surface compared to deep tumor and higher recovery in deep tumor (Fig. 8C). There were no significant changes in IR700 fluorescence and GFP fluorescence in the control mice (Fig. 9A).

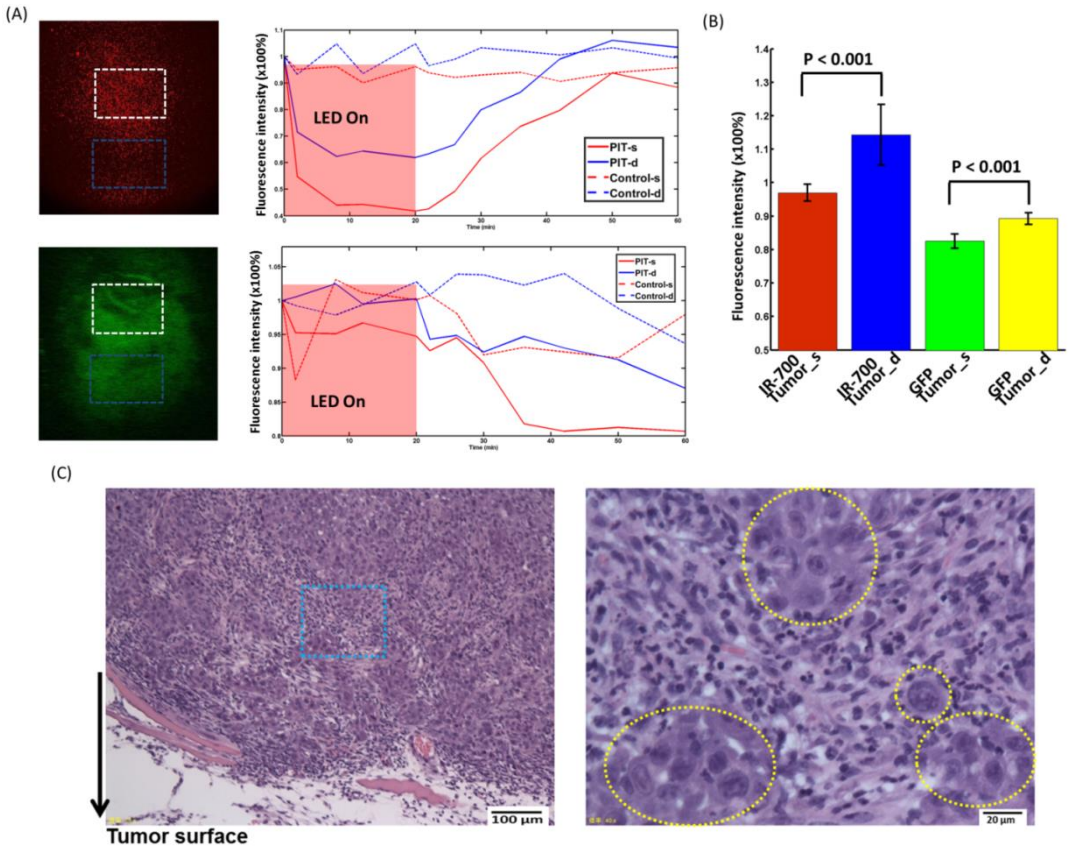

Figure 10. Normalized average fluorescence intensity changes from TPM microprism

(A) Representative normalized average IR700 fluorescence intensity (upper) and GFP intensity (lower) of tumor surface and deep tumor during and after PIT treatment compared with control mouse. (B) Left: IR700 fluorescence recovery value of tumor surface and deep tumor. Deep tumor showed significantly higher fluorescence recovery intensity value than that of the tumor surface (n=5). Right: GFP intensity of tumor surface and deep tumor. The tumor surface showed a significantly larger GFP fluorescence decrease than that of the deep tumor (n=5). (C) Histological specimens of A431 tumors from the PIT-treated group. The image on the right side is the zoomed-in image from the blue square in the left image. The yellow dashed circles indicate undamaged cells. Overall, there was less damage compared to the two-channel fiber bundle results.

In Fig. 10A, the normalized IR700 fluorescence intensity averaged from the white and blue squares showed a greater drop in the tumor surface and greater recovery in deep tumor, while there is no obvious change in controls. The recovery of

IR700 fluorescence intensity in deep tumor is significantly higher than that of the tumor surface and more than 10% higher than the initial value of deep tumor (Fig. 10B). The normalized GFP fluorescence intensity showed a larger drop in the tumor region (both tumor surface and deep tumor) treated with PIT compared to the decrease in controls (lower image and chart in Fig. 10A). The decrease of GFP fluorescence intensity in the tumor surface is significantly greater than that of the deep tumor (Fig. 10B).

In H&E stained sections, more necrotic cells were seen in the tumor surface than in the deep tumor (Fig. 10C) and there are cells remaining undamaged (yellow dashed area in Fig. 10C). There is overall less damage compared to the two-channel fiber bundle results. In the control tumor, no obvious cell necrosis was observed in either tumor surface or the deep tumor. The micro-prism track can be clearly seen ~1.4-1.7 mm below the surface (Fig. 9B).

7.3.6 In vivo *fluorescence imaging of the tumor surface using TPM*

After removing the skin covering the tumor, the nearly intact tumor was placed under the two-photon objective lens for imaging. The ROIs were chosen based on both GFP and IR700 fluorescence signals. Blood vessels and capillaries were included. Before NIR LED irradiation, most of the IR700 clusters were well separated and surrounded the blood vessels (Fig. 11A). Within minutes of turning on the LED, the IR700 fluorescence showed an obvious decrease, with the blood vessels indistinct at 12 min (Fig. 11A). The GFP images also became darker, although the blood vessels can still be clearly distinguished (Fig. 11A). After 20 min of NIR irradiation, the IR700 fluorescence showed quick recovery surrounding the blood vessels with much

higher fluorescence intensity and density (Fig. 11A). There were no significant changes in IR700 and GFP fluorescence in the control mice (Fig. 12A).

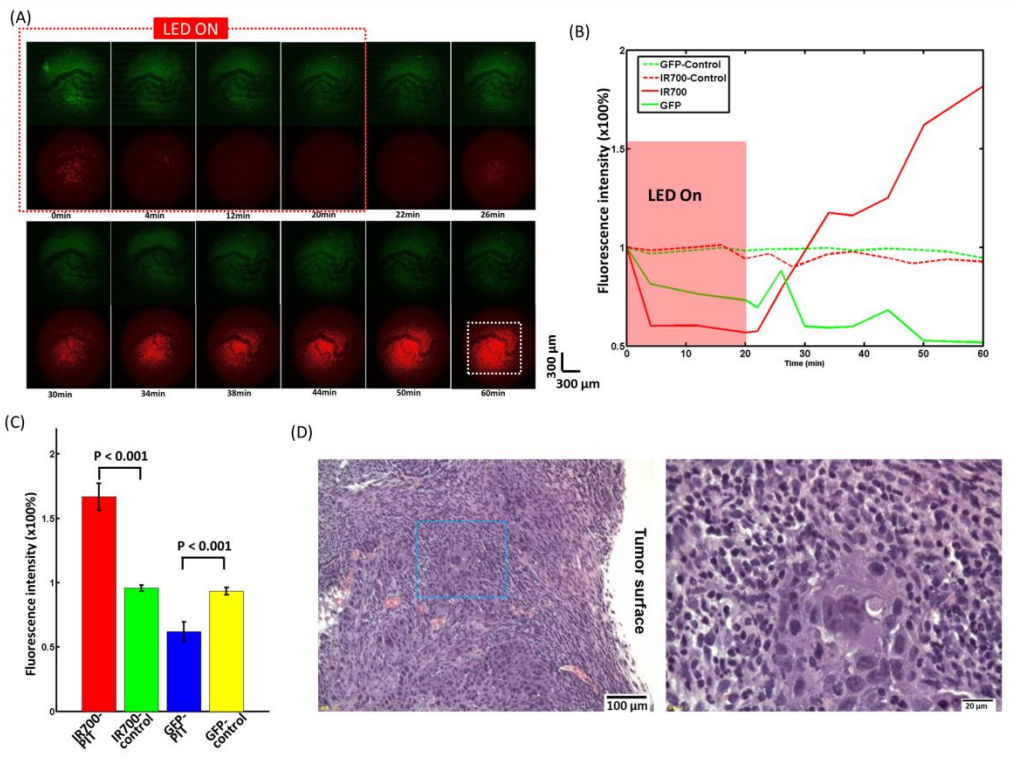

Figure 11. Recording from TPM system

(A) The tumor surface during and after PIT treatment imaged by the TPM system. (B) The average normalized tumor surface IR700 and GFP fluorescence intensity during and after PIT treatment compared with control mice without PIT treatment. The fluorescence signal was calculated from the dashed white square in Fig. 9(A) at 60 min. (C) IR700 fluorescence recovery value of PIT-treated tumors and control tumors without PIT. Tumors with PIT showed a significantly higher IR700 fluorescence intensity value and a lower GFP fluorescence intensity value than in the control tumor (n=5). (D) Histological specimens of A431 tumors from the PIT-treated group. The image on the right side is the zoomed-in image from the blue square in the left image. There is overall less cell damage compared to the two-channel fiber bundle results.

The normalized IR700 fluorescence intensity averaged from the white square in Fig. 11A showed a large drop (~40%) in the tumor surface and high recovery (~160%) after PIT, while there was no clear trend in the controls (Fig. 11B). The recovery of IR700 fluorescence intensity in the tumor surface was significantly higher than that of control tumors and ~1.6-fold greater than initial values (Fig. 11C). The

decrease of GFP fluorescence intensity in the tumor surface was significantly greater than that of the control tumors (Fig. 11C) and also greater than that of the tumor surface viewed using microprism (Fig. 10B).

In sections stained with H&E, there are more necrotic cells seen in the tumor surface than in the deep tumor (Fig. 11D) and there is also overall less cell damage compared to the two-channel fiber bundle results. In the control tumor, no obvious cell necrosis was observed in either tumor surface or the deep tumor (Fig. 12B).

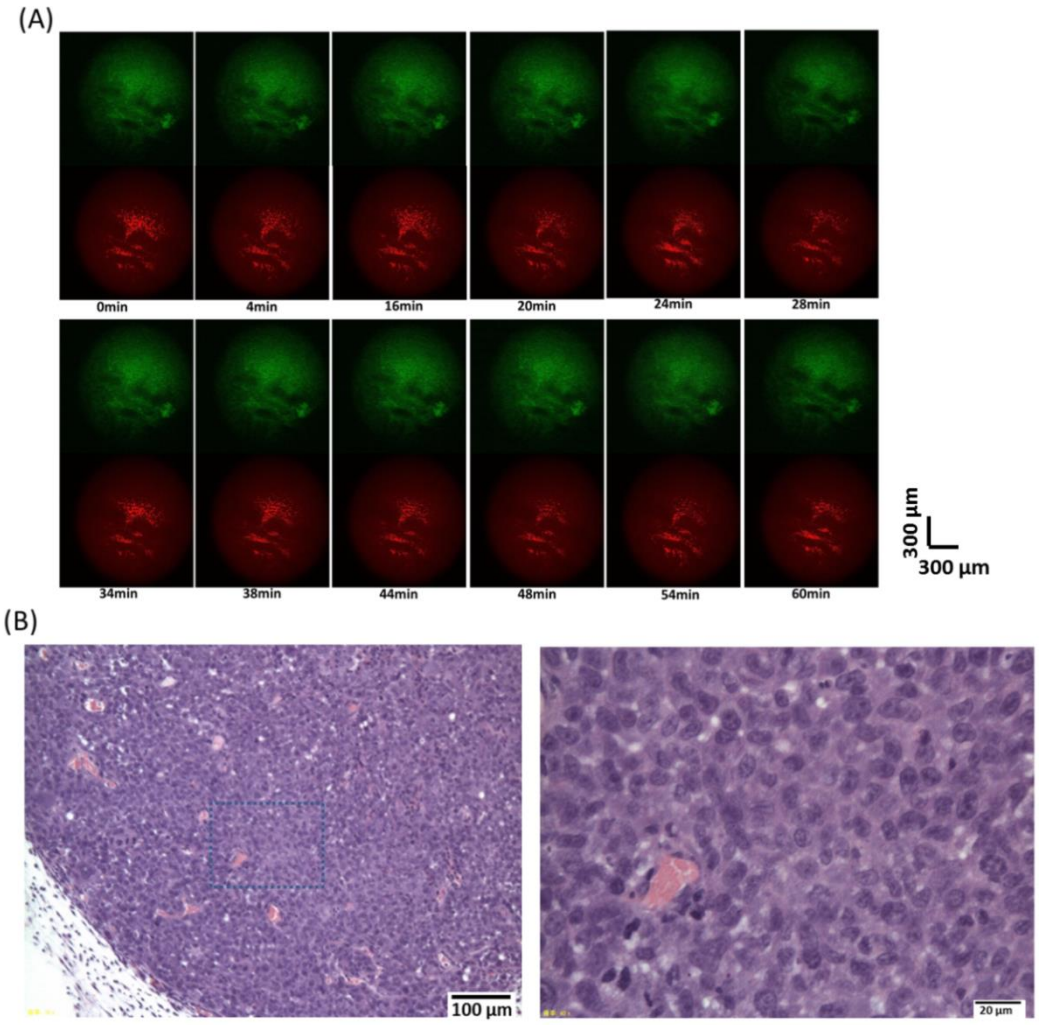

Figure 12. TPM recording from control mice

(A) Tumor surface imaged by TPM system in control mice. (B) Histological specimens of A431 tumors from the control group. No obvious cell necrosis was observed in either tumor surface or the deep tumor. The image on the right side is the zoomed-in image from the blue square in the left image.

7.4 Discussion

One major goal of intravenous cancer therapies is delivery of the therapeutic material in sufficient concentration to all parts of the tumor [41]. Targeted cancer therapies offer the promise of more-effective tumor control with fewer side effects than conventional cancer therapies. PIT is a cell-specific cancer therapy with minimal side effects, which is based on an armed antibody conjugate that induces rapid cellular necrosis after exposure to NIR light [251]. From the pharmacokinetics point of view, antibody conjugation with photosensitizer, IR700, minimally alters the pharmacokinetics of the antibody due to the small size and hydrophilic nature of the IR700 dye. As a result, these APCs show highly targeted accumulation in the tumor and specific binding to target cells with minimal distribution in normal tissue and minimal binding to non-target expressing cells [249, 255-258]. PIT has been reported to induce highly selective cancer cell death, while leaving most of the tumor blood vessels, the means of delivery of the drug to the tumor, unharmed, leading to an effect termed super enhanced permeability and retention (SUPR), which significantly improves the efficacy of the anticancer drug [42]. Although targeted cell death can be examined *in vitro*, it is challenging to observe immediate changes *in vivo* since changes in tumor size take 3–4 days to become visible [253, 259]. Real-time monitoring of PIT effects could be important, as it can ascertain whether a PIT session has been effective or whether additional cycles of therapy are needed [249, 253]. Optical coherence tomography has been used to monitor hemodynamic changes in tumor vessels during PIT in real time [251], and fluorescence lifetime imaging has been used to monitor *in vivo* acute necrotic cancer cell death after NIR PIT [253]. In this paper, we directly

investigated the microdistribution of APCs at different locations (e.g., tumor surface vs. deep tumor) during and after PIT *in situ* and *in vivo* using a minimally invasive two-channel fluorescence fiber imaging system and high resolution TPM with a microprism.

This study employed GFP fluorescence as a surrogate for cell death and IR700 fluorescence as a surrogate for APCs accumulation. In all experiments using FLOT, the two-channel fluorescence needle system or TPM (with or without a microprism), there is a greater decrease in IR700 fluorescence in the tumor surface than in the deep tumor. This is likely due to both the limited penetration of the initial APCs injection and the decreased penetration of NIR as tumor depth increases. Thus, only limited damage to deeper parts of the tumor was observed in comparison to the damage seen in the tumor surface. GFP fluorescence decreased more in the tumor surface than it did in the deep tumor, as was observed in the TPM experiment. This indicates that there is less cell necrosis in the deeper parts of the tumor. The histological results after PIT confirm that there are more necrotic cells in the tumor surface induced by PIT. An interesting observation is that after 20 min of PIT treatment, the IR700 fluorescence recovers very quickly and the relative recovery in the deep tumor regions is greater than that of the tumor surface, and even reaches beyond the initial value in the deep tumor. As reported previously, compared to non-targeting small molecule photosensitizers, mAb−IR700 conjugate stays in the blood circulation longer, which allows unbound mAb−IR700 to redistribute into the remnant target tumor after NIR light irradiation [250]. The increased IR700 fluorescence in the deep tumor in our experiment can be explained by improved intratumoral distribution of

circulating APCs due to enhanced permeability and retention [42]. While we also noticed that the initial IR700 fluorescence in the deep tumor was lower than that of the tumor surface due to limited APCs penetration, fewer APCs were needed to recover or exceed the initial fluorescence value for the deep tumor. Lower recovery in the tumor surface probably also result from cell death in the tumor surface regions. In the control groups, IR700 fluorescence also decreased 5% due to photobleaching from the laser diode or two-photon laser during the long data acquisition period, which can serve as the real reference for fluorescence recovery. The limited quantity of mAb−IR700 conjugate in the circulatory system and limited time of monitoring post-PIT may all contribute the APCs recovery results. However, the increase of APCs in deep tumors provides some clues about the SUPR effect. We suspect that the IR700 fluorescence recovery heterogeneity can reveal the structural heterogeneity of different regions of the tumor, but this will require further study. Histograms of the recovery value of the tumor surface and deep tumor after PIT were plotted, and the deep tumor showed a multimodal shape and a significantly larger separation (SD) [260], which may indicate the deep tumor has a more heterogeneous structure than the surface tumor.

Although the fiber bundle and microprism are minimally invasive to tissue [252, 254, 261], there is still the possibility that their insertion could damage the blood vessels and affect circulation in the tumor. We further investigated the intact tumor under the two-photon objective lens. The recovery of IR700 fluorescence intensity in the tumor surface is significantly higher than that of control tumors and ~1.6-fold higher than its initial values. The decrease of GFP fluorescence intensity in the tumor surface is also

significantly greater than that of the control tumors and of the tumor surface viewed with a microprism. The 1.6-fold recovery may be clear evidence that after NIR irradiation, SUPR enables a significant increase in the quantity of APCs within the tumor. We can expect higher recovery using a fiber bundle and microprism if no damage has been introduced. Although we tried to administer 50 J/cm^2 NIR light to the tumor for each experiment, because of space limitations, the LED could not be arranged close enough to the tumor, especially for the TPM, which uses a bulky objective with a short working distance (2 mm). This blocked much of the NIR light, which can explain why there is overall less cell damage in the TPM experiments compared to the two-channel fiber bundle results, as seen in H&E stained samples. In future, with cell-cycle responsible fluorescent protein labelled tumor cells [262-264], it may be possible to simultaneously monitor cell death and APCs microdistribution in real time in living mice.

7.5 Conclusion

We investigated the microdistribution of APCs at different locations (e.g., tumor surface vs. deep tumor) during and after PIT *in situ* and *in vivo* using a minimally invasive two-channel fluorescence fiber imaging system and a high resolution TPM with and without a microprism. The distribution of APCs was improved after PIT treatment with greater increase and greater heterogeneous recovery in the deep tumor regions. These novel imaging methods are critical for further understanding of the PIT/SUPR mechanism and optimizing the effectiveness of treatment by monitoring theranostic agent distribution and its therapeutic effects, including cellular necrosis, within the tumor microenvironment *in vivo* and in real time.

Chapter 8: Conclusion and Future directions

In Chapter 1, we presented the backgrounds and motivations for different projects in this dissertation and the goal and objective for each chapter was also discussed. In Chapter 2, the history, basic principal and instrumentation of LOT/FLOT were covered and reviewed.

In Chapter 3, we presented the HDR-FLOT method to increase both the dynamic range and penetration depth to alleviate the intrinsic problem of FLOT. The method is easy to implement and can add confidence to the FLOT results with more information. To be more specific, with more than a 20% depth increase compared to conventional FLOT in a mouse brain *in vivo*, we may be able to image the entire six layers in the mouse cortex with HDR-FLOT compared to four layers.

In Chapter 4, by combining VSDi and time-resolved FLOT, we detected the 3D neural activities by deflection of a single whisker of the mouse brain *in vivo*. Localization of neural activities or functional brain mapping, is one of the fundamental tasks for many generations of neuroscientists within the last hundred years. The time-resolved FLOT we presented enables examination of spatiotemporal patterns of neuronal activities in the brain non-invasively and is easy to apply to other neural systems. We think this can provide the neuroscientists a new imaging tool to investigate the neural dynamics and signal propagating in the neocortex.

In Chapter 5, we utilized FLOT system to investigate the cell distribution, visualize the 3D migration process of cells, and evaluate the bone mineralization process within bone tissue engineering scaffolds *in situ*. The results show that FLOT system can represents a promising novel imaging platform to non-destructively

quantify the depth-resolved information of cell-scaffold interactions *in situ* and hold a promise to investigate more scientific topics in tissue engineering. Also it is time to save several people from tedious sample histology slicing and related work burdens.

In Chapter 6, we have investigated the feasibility of a novel multi-modal optical imaging approach including high-resolution optical coherence tomography (OCT) and high-sensitivity fluorescence laminar optical tomography (FLOT) for structural and molecular imaging. The study lays the foundation for further integrating the multi-modal imaging method into an endoscope setup and move the multi-modal imaging method a step forward to clinical translation. Followed by preventive therapy, the new diagnostic tools may lead to significant improvement in patient survival and quality of life.

The work in Chapter 7 is important, as these novel imaging methods are critical for further understanding of the PIT mechanism and optimizing the effectiveness of treatment by monitoring the distribution of a theranostic agent and its therapeutic effects, including cellular necrosis, within the tumor microenvironment *in vivo* and in real time [265]. These novel imaging methods are also applicable for monitoring other cancer treatment methods. The work is expected to contribute significantly to the understanding of the mechanisms of theranostic agents, as well as other tumor-targeted drug delivery systems. After three decades of research in nanomedicine, it is time for harvesting past efforts to produce clinically useful formulations through mechanistic understanding of how nanocarriers work [265].

8.1 Bessel-beam-based fluorescence laminar optical tomography

Fluorescence laminar optical tomography (FLOT) can achieve a resolution of 100-200 μm with 2-3 mm penetration depth and we have applied FLOT to visualize neural activities in mouse brains in vivo in Chapter 4, to image fluorescence-labeled cells in tissue engineering in Chapter 5, and to quantify depth-resolved distribution of fluorescence-labeled tumor in Chapter 6 and 7. In Chapter 3, we present HDR-FLOT to increase FLOT penetration depth and improving the ability to image fluorescent samples with a large concentration difference for FLOT.

However, one problem for FLOT system is spatial resolution at different depth (shown in Chapter 4). Since current FLOT are based on Gauss beam and Gauss beam waist increases rapidly out of its focus, resolution may become worse when the light source goes deeper into turbid sample. To overcome this problem, Bessel beam with featuring of an exceptional depth-of-focus and self-reconstructing properties may be a solution.

Bessel beam can be generated by an axicon. We have compared the current Gauss beam and Bessel beam profile generated by an axicon with 0.1^0 physical angle in the air. The results are shown in Fig. 1. We can see that Bessel beam waist doesn't change when it propogates, with ~5 μm full-width-half-maximum. However, Gauss beam waist becomes much wider when it propagates. While we can notice the Gauss beam has a better performance under 500 μm, which also depends on the focusing lens we used to generate the Gauss beam. We can imagine the Bessel beam-based

FLOT can be very powerful for lower scattering sample (e.g. In tissue engineering) where a deeper penetrating depth is needed.

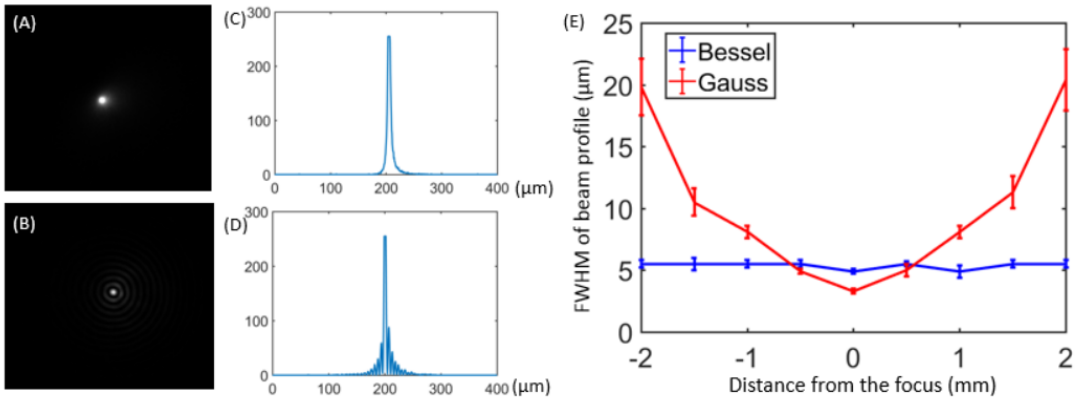

Figure 1. Gauss and Bessel beam profile and axial resolution.
(A)(B) Beam profile of Gauss and Bessel beam at 1mm away from Gauss beam's focal plane.(C)(D) Axial intensity distribution of Gauss and Bessel beam at 1mm away from Gauss beam' focal plane. (E) Analysis of beam resolution of Gauss and Bessel beam from -2 mm to 2 mm to Gauss beam's focal plane.

8.2 3D Mesoscopic Imaging of Neural Activities in Sensory and Motor Cortex

In Chapter 4, we applied FLOT to record 3D neural activities evoked in the whisker system of mice by deflection of a single whisker *in vivo*. As we all know, rodents use their whiskers to locate and identify objects. Conversely, whisker movements are guided by sensory feedback [266]. The primary somatosensory (S1) and primary motor (M1) cortices are reciprocally connected, and their interaction has long been hypothesized to contribute to coordinated motor output. However, very little is known about the nature and synaptic properties of the S1 input to M1 [267]. Neuroanatomical tracing experiments, optogenetic stimulation methods and electrophysiological studies using a sensorimotor slice have shown that neurons in S1 strongly target neurons in L2/3 and L5 of M1, while with a distinct band between L5

and L2/3 containing neurons that were not labeled [266, 267]. We can apply FLOT system combined with voltage-sensitive dye imaging (VSDi) to study 3D neural activities evoked in the barrel and motor cortex, following deflection of a single whisker.

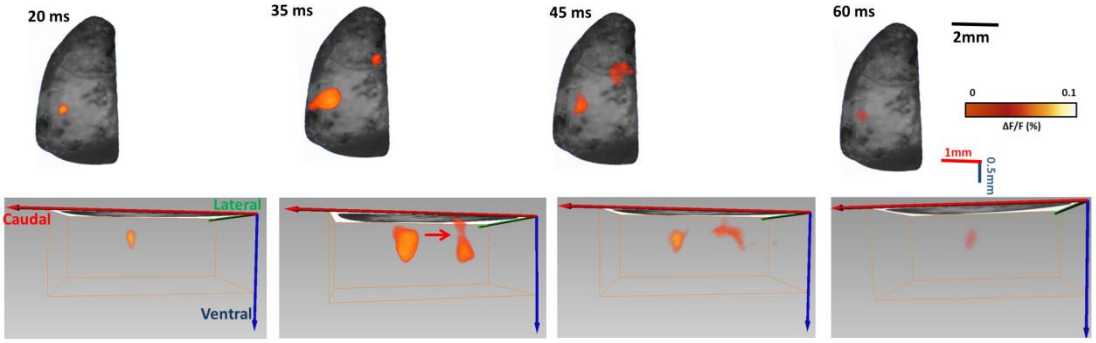

Figure 2. 3D FLOT recording of neural activities in sensory and motor Cortex
Upper row shows change in fluorescence (ΔF/F(%), ordinate) in response to C2 whisker stimulation in brain. Lower row shows corresponding 3D Voltage-sensitive dye fluorescence changes in brain. Time period after stimulation is indicated at the left side of each image.

Changes in fluorescence were calculated as ΔF/F (%) in the recording area. Fig. 2 shows the 2D and 3D images of neural responses responding to C2 whisker in the contralateral brain. The responses appeared first about 20 ms after stimulation in sensory cortex and then transmitted to motor cortex. After 60 ms the fluorescence signals disappear gradually. Imaging the voltage-dependent fluorescence changes of neocortex stained with RH1691 using a fast CCD allows the visualization of the ensemble membrane potential dynamics of the supragranular layers at millisecond temporal resolution and subcolumnar spatial resolution as shown in upper column of Fig.3, while only two-dimensional information can be revealed. Using our FLOT system, the 3D spatiotemporal dynamics of cortical activities can be reconstructed with milliseconds temporal resolution and ~100 μm spatial resolution as shown in lower column of Fig. 3. The ability to resolve 3D spatiotemporal dynamics is of

importance when considering the functional connections between barrel cortex and vibrissal motor cortex. At 35 ms from the 3D image we can notice the neural responses below M1 showed a structure with a weak connection between the two strong responses representing different layers in the M1 which can provide us a clue about the strength of S1 input as a function of cortical layer.

8.3 Develop endoscopic FLOT/OCT system for *in vivo* simultaneous structural and molecular imaging.

In chapter 6, we have investigated the feasibility of a novel multi-modal optical imaging approach including high-resolution optical coherence tomography (OCT) and high-sensitivity fluorescence laminar optical tomography (FLOT) for structural and molecular imaging. The C57BL/6J-Apc^{Min}/J mice were imaged using OCT and FLOT, and the correlated histopathological diagnosis was obtained. Quantitative structural (scattering coefficient) and molecular (relative enzyme activity) parameters were obtained from OCT and FLOT images for multi-parametric analysis. This multi-modal imaging method has demonstrated the feasibility for more accurate diagnosis with 88.23% (82.35%) for sensitivity (specificity) compared to either modality alone. We can consider further integrate the multi-modal imaging method into an endoscope setup and perform the biomedical validation in the pre-clinical animal studies, which will definitely move the multi-modal imaging method a step forward to clinical translation.

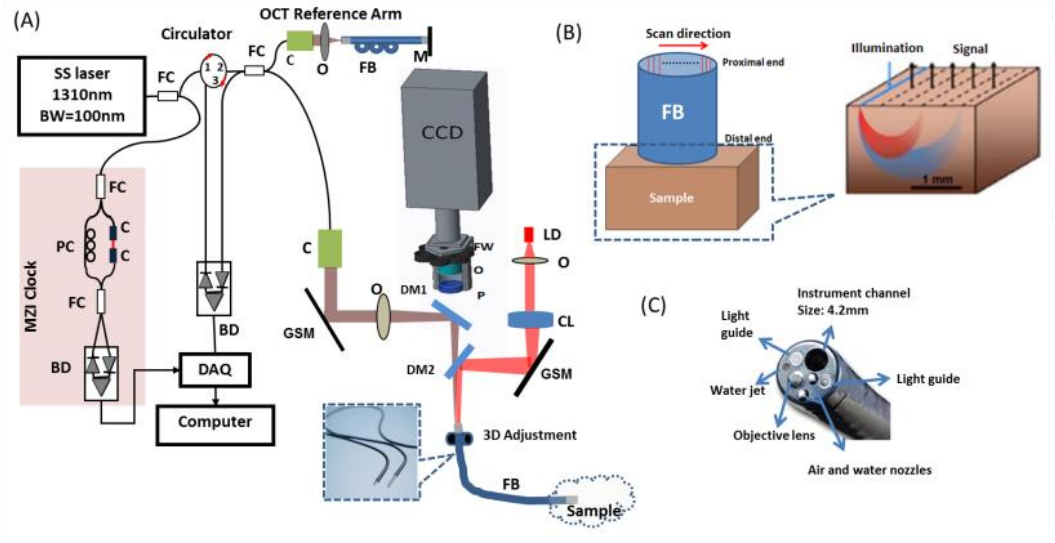

Figure 3. Endoscopic FLOT/OCT system

(A) Schematic of the endoscopic OCT/FLOT imaging system. (B) Schematic of the scanning protocol for FLOT system using fiber bundle. (C) Distal end of the commercial colonoscope. FC: fiber coupler; PC: polarization controller; C: collimator, BD: balanced detector, MZI: Mach-Zehnder interferometer (frequency clocks), DAQ: data acquisition board, M: mirror, GSM: galvonometer scanning mirror, O: objective lens, LD: laser diode, P: polarizer, S: shutter, I: iris, CL: cylindrical lens, W: filter wheel, FB: fiber bundle. Inset shows the flexible fiber bundle.

In order to image the internal colon tissue, a more flexible configuration for the FLOT/OCT system needs to be implemented to integrate with the current colonoscope. OCT can be interfaced with fiber-optic catheters and endoscopes to image inside the body [45, 64-66, 238, 268, 269]. A fiber-optic-bundle-based OCT probe method has been presented with transverse and axial resolution of approximately 12 and 10 µm, respectively [247, 270, 271]. Acquisition of LOT data through a fiber optic bundle has also been developed and demonstrated previously [96]. Fiber bundles are flexible (inset in Fig. 3(A)), coherent image guides used for transmitting optical images from one end to the other [247]. We can develop the instrumentation for the multi-modality imaging platform based on imaging fiber bundle as shown in Fig. 3.

The OCT system and FLOT system will be incorporated through the dichroic mirrors. In this system, the scanning mechanism will be placed at the proximal fiber-bundle entrance (Fig. 3B). The bundle, made up of several thousand cores, preserves the spatial relationship between the entrance and the output of the bundle (distal end) and further to the sample. Therefore, one- or two directional scanning can be readily performed on the proximal bundle surface to create 2D or 3D images. The same fiber bundle is employed in the reference arm of OCT to minimize the dispersion mismatch. Because of this fiber-bundle design, the scanning mechanism can be placed proximally and no moving parts or driving current are needed within the endoscope. This design is extremely compact, solid, and reliable and could be modified for required sizes to perform 3D endoscopic imaging in a range of clinical settings. The fiber bundle we proposed will have a diameter <3 mm, thus the catheter-based imaging device will be easily put inside the instrument channel of the standard colonoscope (Fig. 3C). The integration of both subsystems can be achieved by spatial co-registration using the same imaging probe and temporal synchronization controlled by the same computer. If successful, this will develop a new non-invasive biomedical imaging tool for the early cancer detection. After the development and validation in pre-clinical animal studies, this project has high potential to be translated into clinical studies. It is expected to have a major impact on detection, diagnosis, and characterization of GI cancers, as well as a wide range of epithelial cancers.

8.4 3D FLOT/OCT for Imaging Micro-distribution of APCs during PIT *in vivo*

In Chapter 7, we applied OCT, a minimally invasive two-channel fluorescence fiber imaging system and two-photon microscopy combined with a microprism to monitor mAb-IR700 distribution and therapeutic effects during Photoimmunotherapy (PIT) at different intratumor locations (e.g., tumor surface vs. deep tumor) *in situ* and in real time simultaneously, which enabled evaluation of the therapeutic effects *in vivo* and treatment regimens.

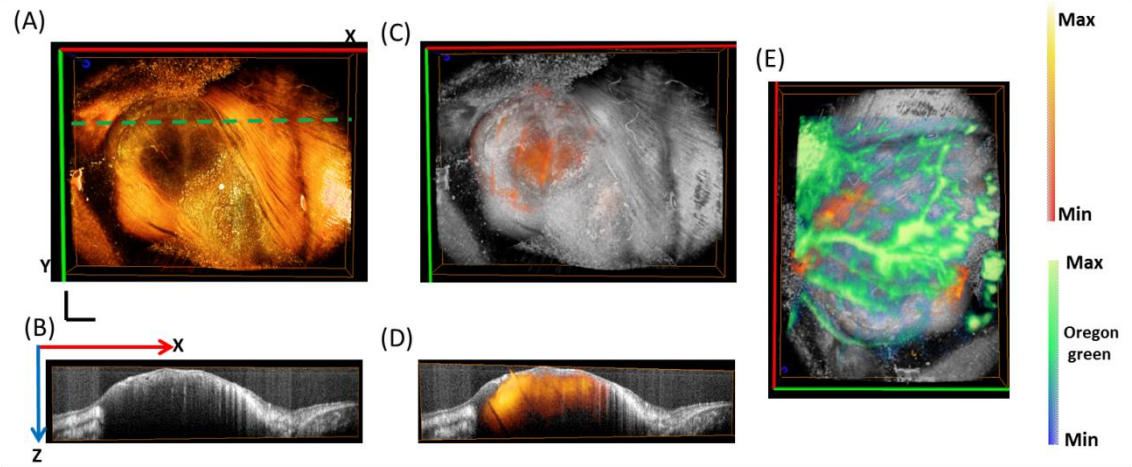

Figure 4. OCT/FLOT imaging of tumors.
(A) Using microstructural contrast, tumor tissue (transplanted epidermoid carcinoma on mice) can be differentiated from surrounding host subcutaneous and muscle tissues. (B) Cross-sectional OCT images from the green dashed line in Fig .4 (A). The image shows the contrast at different tissue depths (shown in the vertical direction) versus distance along the green dashed line (shown in the horizontal direction). Disease progression — from normal tissue to adenoma— can be monitored through hallmark modifications, such as the loss of tissue stratifications. (C) Fused OCT/FLOT image. (D) Cross-sectional fused OCT/FLOT image. (E) Fused OCT/FLOT image with blood vessel on the tumor surface. Scale bar 1 mm.

As mentioned in Chapter 6, OCT is an attractive diagnostic imaging modality. It can provide cross-sectional images of tissue that are analogous to histopathology.

The imaging depth of OCT is approximately 2–3 mm. This depth is shallow when compared to other clinical imaging techniques; however, the image resolution of OCT is 10–100 times greater than conventional ultrasound, MRI, or CT. In addition, the imaging depth of OCT is comparable to that typically sampled by excisional biopsy and is sufficient to evaluate most early neoplastic changes in epithelial cancers as shown in Fig. 4 with the OCT system in our lab. OCT can be interfaced with fiber-optic catheters and endoscopes to image inside the body [45, 64-66]. Endoscopic OCT has been demonstrated in the human GI tract [67-70] to detect Barrett's esophagus (BE) [71, 72], dysplasia [73, 74], and colon cancer [238, 268, 269]. We will further apply OCT combined with FLOT to monitor tumor microstructure, mAb-IR700 distribution and therapeutic effects during Photoimmunotherapy (PIT) as shown in Fig.4(C-D). Moreover, Oregon green labeled dextran with 70000 MW will be injected i.v. before NIR light administration to indicate the vascular distribution of the tumors as shown in Fig. 4(E), thus provide a multi-parameters analysis about the change of the tumor microenvironment during and after PIT. These novel imaging methods are critical for further understanding of the PIT/SUPR mechanism and optimizing the effectiveness of treatment by monitoring theranostic agent distribution and its therapeutic effects, including cellular necrosis, within the tumor microenvironment *in vivo* and in real time.

Bibliography

1. Muto, A., Ohkura, M., Abe, G., Nakai, J. & Kawakami, K. Real-time visualization of neuronal activity during perception. *Curr Biol* **23**, 307-11.
2. Lenkov, D.N., Volnova, A.B., Pope, A.R. & Tsytsarev, V. Advantages and limitations of brain imaging methods in the research of absence epilepsy in humans and animal models. *J Neurosci Methods* **212**, 195-202.
3. Hillman, E.M. Optical brain imaging in vivo: techniques and applications from animal to man. *J Biomed Opt* **12**, 051402 (2007).
4. Sato, K. et al. Intraoperative intrinsic optical imaging of neuronal activity from subdivisions of the human primary somatosensory cortex. *Cereb Cortex* **12**, 269-80 (2002).
5. Tsytsarev, V., Bernardelli, C. & Maslov, K.I. Living Brain Optical Imaging: Technology, Methods and Applications. *J Neurosci Neuroeng* **1**, 180-192 (2012).
6. Li, B., Zhou, F.Y., Luo, Q.M. & Li, P.C. Altered resting-state functional connectivity after cortical spreading depression in mice. *Neuroimage* **63**, 1171-1177 (2012).
7. Dunn, A.K. et al. Simultaneous imaging of total cerebral hemoglobin concentration, oxygenation, and blood flow during functional activation. *Opt Lett* **28**, 28-30 (2003).
8. Tian, F., Alexandrakis, G. & Liu, H. Optimization of probe geometry for diffuse optical brain imaging based on measurement density and distribution. *Appl Opt* **48**, 2496-504 (2009).
9. White, B.R. & Culver, J.P. Phase-encoded retinotopy as an evaluation of diffuse optical neuroimaging. *Neuroimage* **49**, 568-77 (2010).
10. Zhou, C. et al. Diffuse optical monitoring of cerebral hemodynamics in piglet with traumatic brain injury. *J Cereb Blood Flow Metab* **29**, S33-S34 (2009).
11. Chen, Y. et al. Optical coherence tomography (OCT) reveals depth-resolved dynamics during functional brain activation. *J Neurosci Methods* **178**, 162-73 (2009).
12. Srinivasan, V.J., Radhakrishnan, H., Jiang, J.Y., Barry, S. & Cable, A.E. Optical coherence microscopy for deep tissue imaging of the cerebral cortex with intrinsic contrast. *Opt Express* **20**, 2220-39 (2012).
13. Qin, J., Shi, L., Dziennis, S., Reif, R. & Wang, R.K. Fast synchronized dual-wavelength laser speckle imaging system for monitoring hemodynamic changes in a stroke mouse model. *Opt Lett* **37**, 4005-7 (2012).
14. Wang, H. et al. Reconstructing micrometer-scale fiber pathways in the brain: multi-contrast optical coherence tomography based tractography. *Neuroimage* **58**, 984-92 (2011).
15. Yu, L., Nguyen, E., Liu, G., Choi, B. & Chen, Z. Spectral Doppler optical coherence tomography imaging of localized ischemic stroke in a mouse model. *J Biomed Opt* **15**, 066006 (2010).

16. Wang, X. et al. Noninvasive laser-induced photoacoustic tomography for structural and functional in vivo imaging of the brain. *Nat Biotechnol* **21**, 803-6 (2003).
17. McCaslin, A.F., Chen, B.R., Radosevich, A.J., Cauli, B. & Hillman, E.M. In vivo 3D morphology of astrocyte-vasculature interactions in the somatosensory cortex: implications for neurovascular coupling. *J Cereb Blood Flow Metab* **31**, 795-806 (2011).
18. Sakadzic, S. et al. Two-photon high-resolution measurement of partial pressure of oxygen in cerebral vasculature and tissue. *Nat Methods* **7**, 755-9 (2010).
19. Tang, Q. et al. Review of mesoscopic optical tomography for depth-resolved imaging of hemodynamic changes and neural activities. *Neurophotonics* **4**, 011009-011009 (2016).
20. Hillman, E.M.C. & Burgess, S.A. Sub-millimeter resolution 3D optical imaging of living tissue using laminar optical tomography. *Laser & Photonics Reviews* **3**, 159-179 (2009).
21. Jung, J.C., Mehta, A.D., Aksay, E., Stepnoski, R. & Schnitzer, M.J. In vivo mammalian brain imaging using one- and two-photon fluorescence microendoscopy. *J Neurophysiol* **92**, 3121-33 (2004).
22. Liu, Y., Lim, J. & Teoh, S.-H. Review: development of clinically relevant scaffolds for vascularised bone tissue engineering. *Biotechnology advances* **31**, 688-705 (2013).
23. Ball, O., Nguyen, B.-N.B., Placone, J.K. & Fisher, J.P. 3D Printed Vascular Networks Enhance Viability in High-Volume Perfusion Bioreactor. *Annals of Biomedical Engineering* **44**, 3435-3445 (2016).
24. Tan, W. et al. Structural and functional optical imaging of three-dimensional engineered tissue development. *Tissue Engineering* **10**, 1747-1756 (2004).
25. Tan, W., Vinegoni, C., Norman, J.J., Desai, T.A. & Boppart, S.A. Imaging cellular responses to mechanical stimuli within three-dimensional tissue constructs. *Microscopy Research And Technique* **70**, 361-371 (2007).
26. So, P.T.C., Kim, H. & Kochevar, I.E. Two-photon deep tissue ex vivo imaging of mouse dermal and subcutaneous structures. *Optics Express* **3**, 339-350 (1998).
27. Fleischer, D.E. et al. Endoscopic radiofrequency ablation for Barrett's esophagus: 5-year outcomes from a prospective multicenter trial. *Endoscopy* **42**, 781-789 (2010).
28. Dar, M.S., Goldblum, J.R., Rice, T.W. & Falk, G.W. Can extent of high grade dysplasia in Barrett's oesophagus predict the presence of adenocarcinoma at oesophagectomy? *Gut* **52**, 486-489 (2003).
29. Shaheen, N.J. et al. Biopsy depth after radiofrequency ablation of dysplastic Barrett's esophagus. *Gastrointestinal endoscopy* **72**, 490-496. e1 (2010).
30. Mashimo, H. Subsquamous intestinal metaplasia after ablation of Barrett's esophagus: frequency and importance. *Current opinion in gastroenterology* **29**, 454-459 (2013).

31. Zhou, C. et al. Characterization of buried glands before and after radiofrequency ablation by using 3-dimensional optical coherence tomography (with videos). *Gastrointestinal endoscopy* **76**, 32-40 (2012).
32. Shaheen, N.J. et al. Radiofrequency ablation in Barrett's esophagus with dysplasia. *New England Journal of Medicine* **360**, 2277-2288 (2009).
33. Tsai, T.-H. et al. Structural markers observed with endoscopic 3-dimensional optical coherence tomography correlating with Barrett's esophagus radiofrequency ablation treatment response (with videos). *Gastrointestinal endoscopy* **76**, 1104-1112 (2012).
34. Vaccaro, B.J. et al. Detection of intestinal metaplasia after successful eradication of Barrett's esophagus with radiofrequency ablation. *Digestive diseases and sciences* **56**, 1996-2000 (2011).
35. Pouw, R.E. et al. Properties of the neosquamous epithelium after radiofrequency ablation of Barrett's esophagus containing neoplasia. *The American journal of gastroenterology* **104**, 1366-1373 (2009).
36. Ragunath, K. et al. Endoscopic ablation of dysplastic Barrett's oesophagus comparing argon plasma coagulation and photodynamic therapy: a randomized prospective trial assessing efficacy and cost-effectiveness. *Scand J Gastroenterol* **40**, 750-8 (2005).
37. Mino-Kenudson, M. et al. Buried dysplasia and early adenocarcinoma arising in barrett esophagus after porfimer-photodynamic therapy. *Am J Surg Pathol* **31**, 403-9 (2007).
38. Gray, N.A., Odze, R.D. & Spechler, S.J. Buried metaplasia after endoscopic ablation of Barrett's esophagus: a systematic review. *The American journal of gastroenterology* **106**, 1899-1908 (2011).
39. Basavappa, M., Weinberg, A., Huang, Q. & Mashimo, H. Markers suggest reduced malignant potential of subsquamous intestinal metaplasia compared with Barrett's esophagus. *Diseases of the Esophagus* **27**, 262-266 (2014).
40. Tang, Q. et al. Depth-resolved imaging of colon tumor using optical coherence tomography and fluorescence laminar optical tomography. *Biomedical Optics Express* **7**, 5218-5232 (2016).
41. Nagaya, T. et al. Improved micro-distribution of antibody-photon absorber conjugates after initial near infrared photoimmunotherapy (NIR-PIT). *Journal of Controlled Release* **232**, 1-8 (2016).
42. Sano, K., Nakajima, T., Choyke, P.L. & Kobayashi, H. Markedly enhanced permeability and retention effects induced by photo-immunotherapy of tumors. *ACS Nano* **7**, 717-24 (2013).
43. Huang, D. et al. Optical coherence tomography. *Science* **254**, 1178-81 (1991).
44. Fujimoto, J.G. et al. Optical Biopsy And Imaging Using Optical Coherence Tomography. *Nature Medicine* **1**, 970-972 (1995).
45. Tearney, G.J. et al. In vivo endoscopic optical biopsy with optical coherence tomography. *Science* **276**, 2037-2039 (1997).
46. Bouma, B.E., Yun, S.H., Vakoc, B.J., Suter, M.J. & Tearney, G.J. Fourier-domain optical coherence tomography: recent advances toward clinical utility. *Current Opinion In Biotechnology* **20**, 111-118 (2009).

47. Huang, D. et al. Optical coherence tomography. *Science* **254**, 1178-1181 (1991).
48. Bouma, B.E. & Tearney, G.J. Clinical imaging with optical coherence tomography. *Academic Radiology* **9**, 942-53 (2002).
49. Li, X.D. et al. Optical coherence tomography: Advanced technology for the endoscopic imaging of Barrett's esophagus. *Endoscopy* **32**, 921-930 (2000).
50. Wang, R.K. Optical Microangiography: A Label Free 3D Imaging Technology to Visualize and Quantify Blood Circulations within Tissue Beds in vivo. *IEEE J Sel Top Quantum Electron* **16**, 545-554 (2010).
51. Chen, Z., Milner, T.E., Dave, D. & Nelson, J.S. Optical Doppler tomographic imaging of fluid flow velocity in highly scattering media. *Optics Letters* **22**, 64-6 (1997).
52. Choma, M.A., Sarunic, M.V., Yang, C.H. & Izatt, J.A. Sensitivity advantage of swept source and Fourier domain optical coherence tomography. *Optics Express* **11**, 2183-2189 (2003).
53. de Boer, J.F. et al. Improved signal-to-noise ratio in spectral-domain compared with time-domain optical coherence tomography. *Optics Letters* **28**, 2067-2069 (2003).
54. Leitgeb, R., Hitzenberger, C.K. & Fercher, A.F. Performance of Fourier domain vs. time domain optical coherence tomography. *Optics Express* **11**, 889-894 (2003).
55. Chen, Z.P. et al. Noninvasive imaging of in vivo blood flow velocity using optical Doppler tomography. *Optics Letters* **22**, 1119-1121 (1997).
56. Izatt, J.A., Kulkami, M.D., Yazdanfar, S., Barton, J.K. & Welch, A.J. In vivo bidirectional color Doppler flow imaging of picoliter blood volumes using optical coherence tomograghy. *Optics Letters* **22**, 1439-1441 (1997).
57. Zhao, Y.H. et al. Doppler standard deviation imaging for clinical monitoring of in vivo human skin blood flow. *Optics Letters* **25**, 1358-1360 (2000).
58. Choi, W. et al. Choriocapillaris and choroidal microvasculature imaging with ultrahigh speed OCT angiography. *PLoS One* **8**, e81499 (2013).
59. Drexler, W. et al. Optical coherence tomography today: speed, contrast, and multimodality. *J Biomed Opt* **19**, 071412 (2014).
60. Mariampillai, A. et al. Speckle variance detection of microvasculature using swept-source optical coherence tomography. *Optics Letters* **33**, 1530-1532 (2008).
61. Ding, Z., Liang, C.-P. & Chen, Y. Technology developments and biomedical applications of polarization-sensitive optical coherence tomography. *Frontiers of Optoelectronics*, 1-13 (2015).
62. Al-Qaisi, M.K. & Akkin, T. Swept-source polarization-sensitive optical coherence tomography based on polarization-maintaining fiber. *Opt Express* **18**, 3392-403 (2010).
63. Jiao, S. & Wang, L.V. Two-dimensional depth-resolved Mueller matrix of biological tissue measured with double-beam polarization-sensitive optical coherence tomography. *Opt Lett* **27**, 101-3 (2002).
64. Liang, C.P. et al. A forward-imaging needle-type OCT probe for image guided stereotactic procedures. *Opt Express* **19**, 26283-94 (2011).

65. Xi, J. et al. Diffractive catheter for ultrahigh-resolution spectral-domain volumetric OCT imaging. *Opt Lett* **39**, 2016-9 (2014).
66. Sharma, G.K. et al. Long-Range Optical Coherence Tomography of the Neonatal Upper Airway for Early Diagnosis of Intubation-related Subglottic Injury. *American Journal Of Respiratory And Critical Care Medicine* **192**, 1504-1513 (2015).
67. Chen, Y. et al. Ultrahigh resolution optical coherence tomography of Barrett's esophagus: preliminary descriptive clinical study correlating images with histology. *Endoscopy* **39**, 599-605 (2007).
68. Sergeev, A.M. et al. In vivo endoscopic OCT imaging of precancer and cancer states of human mucosa. *Optics Express* **1**, 432-440 (1997).
69. Bouma, B.E., Tearney, G.J., Compton, C.C. & Nishioka, N.S. High-resolution imaging of the human esophagus and stomach in vivo using optical coherence tomography. *Gastrointestinal Endoscopy* **51**, 467-474 (2000).
70. Gora, M.J. et al. Tethered capsule endomicroscopy enables less invasive imaging of gastrointestinal tract microstructure. *Nat Med* **19**, 238-40 (2013).
71. Poneros, J.M. et al. Diagnosis of specialized intestinal metaplasia by optical coherence tomography. *Gastroenterology* **120**, 7-12 (2001).
72. Liang, K. et al. Ultrahigh speed en face OCT capsule for endoscopic imaging. *Biomed Opt Express* **6**, 1146-63 (2015).
73. Isenberg, G. et al. Accuracy of endoscopic optical coherence tomography in the detection of dysplasia in Barrett's esophagus: a prospective, double-blinded study. *Gastrointestinal Endoscopy* **62**, 825-831 (2005).
74. Evans, J.A. et al. Optical coherence tomography to identify intramucosal carcinoma and high-grade dysplasia in Barrett's esophagus. *Clinical Gastroenterology And Hepatology* **4**, 38-43 (2006).
75. Zhang, F., Wang, L.P., Boyden, E.S. & Deisseroth, K. Channelrhodopsin-2 and optical control of excitable cells. *Nat Methods* **3**, 785-92 (2006).
76. Tsytsarev, V., Pope, D., Pumbo, E., Yablonskii, A. & Hofmann, M. Study of the cortical representation of whisker directional deflection using voltage-sensitive dye optical imaging. *Neuroimage* **53**, 233-8.
77. Grinvald, A. & Hildesheim, R. VSDI: a new era in functional imaging of cortical dynamics. *Nat Rev Neurosci* **5**, 874-85 (2004).
78. Loew, L.M., Scully, S., Simpson, L. & Waggoner, A.S. Evidence for a charge-shift electrochromic mechanism in a probe of membrane potential. *Nature* **281**, 497-9 (1979).
79. Tasaki, I., Watanabe, A., Sandlin, R. & Carnay, L. Changes in fluorescence, turbidity, and birefringence associated with nerve excitation. *Proc Natl Acad Sci U S A* **61**, 883-8 (1968).
80. Tang, Q. et al. In Vivo Mesoscopic Voltage-Sensitive Dye Imaging of Brain Activation. *Sci Rep* **6**, 25269 (2016).
81. Santi, P.A. Light sheet fluorescence microscopy a review. *Journal of Histochemistry & Cytochemistry* **59**, 129-138 (2011).
82. Power, R.M. & Huisken, J. A guide to light-sheet fluorescence microscopy for multiscale imaging. *Nature Methods* **14**, 360-373 (2017).

83. Mickoleit, M. et al. High-resolution reconstruction of the beating zebrafish heart. *Nature methods* **11**, 919-922 (2014).
84. Denk, W., Strickler, J.H. & Webb, W.W. Two-photon laser scanning fluorescence microscopy. *Science* **248**, 73-6 (1990).
85. Zhou, Y.P., Bifano, T. & Lin, C. Adaptive optics two photon scanning laser fluorescence microscopy. *Mems Adaptive Optics V* **7931** (2011).
86. Helmchen, F. & Denk, W. Deep tissue two-photon microscopy. *Nature methods* **2**, 932-940 (2005).
87. Horton, N.G. et al. In vivo three-photon microscopy of subcortical structures within an intact mouse brain. *Nature Photonics* **7**, 205-209 (2013).
88. Kobat, D., Horton, N.G. & Xu, C. In vivo two-photon microscopy to 1.6-mm depth in mouse cortex. *J Biomed Opt* **16**, 106014 (2011).
89. (!!! INVALID CITATION !!!).
90. Dunn, A. & Boas, D. Transport-based image reconstruction in turbid media with small source-detector separations. *Optics Letters* **25**, 1777-1779 (2000).
91. Hillman, E.M.C., Boas, D.A., Dale, A.M. & Dunn, A.K. Laminar optical tomography: demonstration of millimeter-scale depth-resolved imaging in turbid media. *Optics Letters* **29**, 1650-1652 (2004).
92. Yuan, B.H. et al. A system for high-resolution depth-resolved optical imaging of fluorescence and absorption contrast. *Review Of Scientific Instruments* **80** (2009).
93. Hillman, E.M.C., Bernus, O., Pease, E., Bouchard, M.B. & Pertsov, A. Depth-resolved optical imaging of transmural electrical propagation in perfused heart. *Optics Express* **15**, 17827-17841 (2007).
94. Yuan, S., Li, Q., Jiang, J., Cable, A. & Chen, Y. Three-dimensional coregistered optical coherence tomography and line-scanning fluorescence laminar optical tomography. *Optics Letters* **34**, 1615-1617 (2009).
95. Hillman, E.M.C. et al. Depth-resolved optical imaging and microscopy of vascular compartment dynamics during somatosensory stimulation. *Neuroimage* **35**, 89-104 (2007).
96. Burgess, S.A., Ratner, D., Chen, B.R. & Hillman, E.M. Fiber-optic and articulating arm implementations of laminar optical tomography for clinical applications. *Biomed Opt Express* **1**, 780-790 (2010).
97. Bjorn, S., Ntziachristos, V. & Schulz, R. Mesoscopic Epifluorescence Tomography: Reconstruction of superficial and deep fluorescence in highly-scattering media. *Optics Express* **18**, 8422-8429 (2010).
98. Zhao, L.L., Lee, V.K., Yoo, S.S., Dai, G.H. & Intes, X. The integration of 3-D cell printing and mesoscopic fluorescence molecular tomography of vascular constructs within thick hydrogel scaffolds. *Biomaterials* **33**, 5325-5332 (2012).
99. Ozturk, M.S., Lee, V.K., Zhao, L.L., Dai, G.H. & Intes, X. Mesoscopic fluorescence molecular tomography of reporter genes in bioprinted thick tissue. *Journal Of Biomedical Optics* **18** (2013).
100. Ozturk, M.S., Rohrbach, D., Sunar, U. & Intes, X. Mesoscopic Fluorescence Tomography of a Photosensitizer (HPPH) 3D Biodistribution in Skin Cancer. *Academic Radiology* **21**, 271-280 (2014).

101. Bjorn, S., Englmeier, K.H., Ntziachristos, V. & Schulz, R. Reconstruction of fluorescence distribution hidden in biological tissue using mesoscopic epifluorescence tomography. *Journal Of Biomedical Optics* **16** (2011).
102. Chen, Y. et al. Integrated Optical Coherence Tomography (OCT) and Fluorescence Laminar Optical Tomography (FLOT). *Ieee Journal Of Selected Topics In Quantum Electronics* **16**, 755-766 (2010).
103. Ozturk, M.S. et al. Mesoscopic Fluorescence Molecular Tomography for Evaluating Engineered Tissues. *Annals Of Biomedical Engineering* **44**, 667-679 (2016).
104. Prevedel, R. et al. Simultaneous whole-animal 3D imaging of neuronal activity using light-field microscopy. *Nature methods* **11**, 727-730 (2014).
105. Levoy, M., Zhang, Z. & McDowall, I. Recording and controlling the 4D light field in a microscope using microlens arrays. *Journal of microscopy* **235**, 144-162 (2009).
106. Levoy, M., Ng, R., Adams, A., Footer, M. & Horowitz, M. Light field microscopy. *ACM Transactions on Graphics (TOG)* **25**, 924-934 (2006).
107. Wang, Z.G., Durand, D.B., Schoenberg, M. & Pan, Y.T. Fluorescence guided optical coherence tomography for the diagnosis of early bladder cancer in a rat model. *Journal Of Urology* **174**, 2376-2381 (2005).
108. Hillman, E.M., Bernus, O., Pease, E., Bouchard, M.B. & Pertsov, A. Depth-resolved optical imaging of transmural electrical propagation in perfused heart. *Opt Express* **15**, 17827-41 (2007).
109. Yuan, B. et al. A system for high-resolution depth-resolved optical imaging of fluorescence and absorption contrast. *Rev Sci Instrum* **80**, 043706 (2009).
110. Venugopal, V. & Intes, X. Recent Advances in Optical Mammography. *Current Medical Imaging Reviews* **8**, 244-259 (2012).
111. Chen, Y. et al. Integrated Optical Coherence Tomography (OCT) and Fluorescence Laminar Optical Tomography (FLOT). *IEEE J. Selected Topics in Quantum Electronics* **16**, 755-766 (2010).
112. Chen, C.W. & Chen, Y. Optimization of Design Parameters for Fluorescence Laminar Optical Tomography. *Journal of Innovative Optical Health Sciences* **4**, 309-323 (2011).
113. Cuccia, D.J., Bevilacqua, F., Durkin, A.J., Ayers, F.R. & Tromberg, B.J. Quantitation and mapping of tissue optical properties using modulated imaging. *Journal Of Biomedical Optics* **14** (2009).
114. Cuccia, D.J., Bevilacqua, F., Durkin, A.J. & Tromberg, B.J. Modulated imaging: quantitative analysis and tomography of turbid media in the spatial-frequency domain. *Optics Letters* **30**, 1354-1356 (2005).
115. Gioux, S. et al. Three-dimensional surface profile intensity correction for spatially modulated imaging. *Journal Of Biomedical Optics* **14** (2009).
116. Jacques, S.L. Optical properties of biological tissues: a review. *Phys Med Biol* **58**, R37-61 (2013).
117. Hillman, E.M.C. et al. Calibration techniques and datatype extraction for time-resolved optical tomography. *Review Of Scientific Instruments* **71**, 3415-3427 (2000).

118. Arridge, S.R. & Schotland, J.C. Optical tomography: forward and inverse problems. *Inverse Problems* **25** (2009).
119. Arridge, S.R. & Schweiger, M. Image reconstruction in optical tomography. *Philosophical Transactions Of the Royal Society B-Biological Sciences* **352**, 717-726 (1997).
120. Klose, A.D. & Hielscher, A.H. Iterative reconstruction scheme for optical tomography based on the equation of radiative transfer. *Medical Physics* **26**, 1698-1707 (1999).
121. Kienle, A. & Patterson, M.S. Improved solutions of the steady-state and the time-resolved diffusion equations for reflectance from a semi-infinite turbid medium. *Journal Of the Optical Society Of America a-Optics Image Science And Vision* **14**, 246-254 (1997).
122. Haskell, R.C., Svaasand, L.O., Tsay, T.T., Feng, T.C. & Mcadams, M.S. Boundary-Conditions for the Diffusion Equation In Radiative-Transfer. *Journal Of the Optical Society Of America a-Optics Image Science And Vision* **11**, 2727-2741 (1994).
123. Iranmahboob, A.K. & Hillman, E.M. in Biomedical Optics BSuE34 (Optical Society of America, St. Petersburg, Florida, 2008).
124. Yoo, K.M., Liu, F. & Alfano, R.R. When Does the Diffusion-Approximation Fail To Describe Photon Transport In Random-Media. *Physical Review Letters* **64**, 2647-2650 (1990).
125. YUAN, B. RADIATIVE TRANSPORT IN THE DELTA-P1 APPROXIMATION FOR LAMINAR OPTICAL TOMOGRAPHY. *Journal of Innovative Optical Health Sciences* **02**, 149-163 (2009).
126. Vitkin, E. et al. Photon diffusion near the point-of-entry in anisotropically scattering turbid media. *Nat Commun* **2**, 587 (2011).
127. Wilson, B.C. & Adam, G. A Monte-Carlo Model for the Absorption And Flux Distributions Of Light In Tissue. *Medical Physics* **10**, 824-830 (1983).
128. Wang, L., Jacques, S.L. & Zheng, L. MCML--Monte Carlo modeling of light transport in multi-layered tissues. *Comput Methods Programs Biomed* **47**, 131-46 (1995).
129. Boas, D., Culver, J., Stott, J. & Dunn, A. Three dimensional Monte Carlo code for photon migration through complex heterogeneous media including the adult human head. *Optics express* **10**, 159-170 (2002).
130. Zhu, C.G. & Liu, Q. Review of Monte Carlo modeling of light transport in tissues. *Journal Of Biomedical Optics* **18** (2013).
131. Flock, S.T., Patterson, M.S., Wilson, B.C. & Wyman, D.R. Monte Carlo modeling of light propagation in highly scattering tissues. I. Model predictions and comparison with diffusion theory. *IEEE Transactions on Biomedical Engineering* **36**, 1162-1168 (1989).
132. Graaff, R. et al. Condensed Monte Carlo simulations for the description of light transport. *Appl Opt* **32**, 426-34 (1993).
133. Hayakawa, C.K. et al. Perturbation Monte Carlo methods to solve inverse photon migration problems in heterogeneous tissues. *Optics Letters* **26**, 1335-1337 (2001).

134. Wang, L.H. & Jacques, S.L. Hybrid Model Of Monte-Carlo Simulation And Diffusion-Theory for Light Reflectance by Turbid Media. *Journal Of the Optical Society Of America a-Optics Image Science And Vision* **10**, 1746-1752 (1993).
135. Liu, Q. & Ramanujam, N. Sequential estimation of optical properties of a two-layered epithelial tissue model from depth-resolved ultraviolet-visible diffuse reflectance spectra. *Applied Optics* **45**, 4776-4790 (2006).
136. Alerstam, E., Svensson, T. & Andersson-Engels, S. Parallel computing with graphics processing units for high-speed Monte Carlo simulation of photon migration. *Journal of biomedical optics* **13**, 060504-060504-3 (2008).
137. Fang, Q.Q. & Boas, D.A. Monte Carlo Simulation of Photon Migration in 3D Turbid Media Accelerated by Graphics Processing Units. *Optics Express* **17**, 20178-20190 (2009).
138. Chen, J. & Intes, X. Comparison of Monte Carlo methods for fluorescence molecular tomography-computational efficiency. *Medical Physics* **38**, 5788-5798 (2011).
139. Gardner, A.R., Hayakawa, C.K. & Venugopalan, V. Coupled forward-adjoint Monte Carlo simulation of spatial-angular light fields to determine optical sensitivity in turbid media. *Journal Of Biomedical Optics* **19** (2014).
140. Hillman, E.M. et al. in BiOS 2001 The International Symposium on Biomedical Optics 327-338 (International Society for Optics and Photonics, 2001).
141. Yang, F. et al. High-resolution mesoscopic fluorescence molecular tomography based on compressive sensing. *IEEE Transactions on Biomedical Engineering* **62**, 248-255 (2015).
142. Pogue, B.W., McBride, T.O., Osterberg, U.L. & Paulsen, K.D. Comparison of imaging geometries for diffuse optical tomography of tissue. *Optics Express* **4**, 270-286 (1999).
143. Zhu, W. et al. Iterative total least-squares image reconstruction algorithm for optical tomography by the conjugate gradient method. *JOSA A* **14**, 799-807 (1997).
144. Intes, X., Ntziachristos, V., Culver, J.P., Yodh, A. & Chance, B. Projection access order in algebraic reconstruction technique for diffuse optical tomography. *Physics in medicine and biology* **47**, N1 (2001).
145. Pogue, B.W., McBride, T.O., Prewitt, J., Österberg, U.L. & Paulsen, K.D. Spatially variant regularization improves diffuse optical tomography. *Applied optics* **38**, 2950-2961 (1999).
146. Endoh, R., Fujii, M. & Nakayama, K. Depth-adaptive regularized reconstruction for reflection diffuse optical tomography. *Optical review* **15**, 51-56 (2008).
147. Intes, X. et al. In vivo continuous-wave optical breast imaging enhanced with Indocyanine Green. *Medical physics* **30**, 1039-1047 (2003).
148. Friedland, R.P. & Iadecola, C. Roy And Sherrington (1890) - a Centennial Reexamination Of on the Regulation Of the Blood-Supply Of the Brain. *Neurology* **41**, 10-14 (1991).

149. Fox, P.T. & Raichle, M.E. Focal Physiological Uncoupling Of Cerebral Blood-Flow And Oxidative-Metabolism during Somatosensory Stimulation In Human-Subjects. *Proceedings Of the National Academy Of Sciences Of the United States Of America* **83**, 1140-1144 (1986).
150. Woolsey, T.A. et al. Neuronal units linked to microvascular modules in cerebral cortex: Response elements for imaging the brain. *Cerebral Cortex* **6**, 647-660 (1996).
151. Li, N., van Zijl, P., Thakor, N. & Pelled, G. Study of the Spatial Correlation Between Neuronal Activity and BOLD fMRI Responses Evoked by Sensory and Channelrhodopsin-2 Stimulation in the Rat Somatosensory Cortex. *Journal Of Molecular Neuroscience* **53**, 553-561 (2014).
152. Vazquez, A.L., Fukuda, M., Crowley, J.C. & Kim, S.G. Neural and Hemodynamic Responses Elicited by Forelimb- and Photo-stimulation in Channelrhodopsin-2 Mice: Insights into the Hemodynamic Point Spread Function. *Cerebral Cortex* **24**, 2908-2919 (2014).
153. Iordanova, B., Vazquez, A.L., Poplawsky, A.J., Fukuda, M. & Kim, S.G. Neural and hemodynamic responses to optogenetic and sensory stimulation in the rat somatosensory cortex. *J Cereb Blood Flow Metab* **35**, 922-32 (2015).
154. Salinet, A.S., Haunton, V.J., Panerai, R.B. & Robinson, T.G. A systematic review of cerebral hemodynamic responses to neural activation following stroke. *J Neurol* **260**, 2715-21 (2013).
155. Devor, A. et al. Coupling of total hemoglobin concentration, oxygenation, and neural activity in rat somatosensory cortex. *Neuron* **39**, 353-9 (2003).
156. Sheth, S.A. et al. Linear and nonlinear relationships between neuronal activity, oxygen metabolism, and hemodynamic responses. *Neuron* **42**, 347-355 (2004).
157. Kotlikoff, M.I. Genetically encoded Ca2+ indicators: using genetics and molecular design to understand complex physiology. *Journal Of Physiology-London* **578**, 55-67 (2007).
158. Tanbakuchi, A.A., Rouse, A.R. & Gmitro, A.F. Monte Carlo characterization of parallelized fluorescence confocal systems imaging in turbid media. *Journal of biomedical optics* **14**, 044024-044024-16 (2009).
159. Muldoon, T.J., Burgess, S.A., Chen, B.R., Ratner, D. & Hillman, E.M.C. Analysis of skin lesions using laminar optical tomography. *Biomedical Optics Express* **3**, 1701-1712 (2012).
160. Boyde, A. Stereoscopic Images In Confocal (Tandem Scanning) Microscopy. *Science* **230**, 1270-1272 (1985).
161. Robertson, M.A., Borman, S. & Stevenson, R.L. Estimation-theoretic approach to dynamic range enhancement using multiple exposures. *Journal of Electronic Imaging* **12**, 219-228 (2003).
162. Madden, B.C. Extended intensity range imaging. (1993).
163. Debevec, P.E. & Malik, J. in ACM SIGGRAPH 2008 classes 31 (ACM, 2008).
164. Lian, L. et al. High-dynamic-range fluorescence molecular tomography for imaging of fluorescent targets with large concentration differences. *Optics Express* **24**, 19920-19933 (2016).

165. Fei, P. et al. High dynamic range optical projection tomography (HDR-OPT). *Optics Express* **20**, 8824-8836 (2012).
166. Vinegoni, C. et al. Real-time high dynamic range laser scanning microscopy. *Nature communications* **7** (2016).
167. Chen, C.-W., Yeatts, A.B., Coates, E.E., Fisher, J.P. & Chen, Y. in Biomedical Optics and 3-D Imaging BTu4A.5 (Optical Society of America, Miami, Florida, 2012).
168. Yuan, S. et al. Co-registered optical coherence tomography and fluorescence molecular imaging for simultaneous morphological and molecular imaging. *Phys Med Biol* **55**, 191-206 (2010).
169. Tang, Q., Liang, C.-P., Wu, K., Sandler, A. & Chen, Y. Real-time epidural anesthesia guidance using optical coherence tomography needle probe. *Quantitative Imaging in Medicine and Surgery* **5**, 118-124 (2014).
170. Wang, L.H. & Jacques, S.L. Use Of a Laser-Beam with an Oblique Angle Of Incidence To Measure the Reduced Scattering Coefficient Of a Turbid Medium. *Applied Optics* **34**, 2362-2366 (1995).
171. Johns, M., Giller, C.A., German, D.C. & Liu, H.L. Determination of reduced scattering coefficient of biological tissue from a needle-like probe. *Optics Express* **13**, 4828-4842 (2005).
172. Sandell, J.L. & Zhu, T.C. A review of in-vivo optical properties of human tissues and its impact on PDT. *Journal Of Biophotonics* **4**, 773-787 (2011).
173. Tang, Q. et al. In Vivo Voltage-Sensitive Dye Imaging of Subcortical Brain Function. *Sci Rep* **5**, 17325 (2015).
174. Tsytsarev, V., Premachandra, K., Takeshita, D. & Bahar, S. Imaging cortical electrical stimulation in vivo: fast intrinsic optical signal versus voltage-sensitive dyes. *Opt Lett* **33**, 1032-4 (2008).
175. Tsytsarev, V., Pope, D., Pumbo, E., Yablonskii, A. & Hofmann, M. Study of the cortical representation of whisker directional deflection using voltage-sensitive dye optical imaging. *Neuroimage* **53**, 233-8 (2010).
176. Huisken, J., Swoger, J., Del Bene, F., Wittbrodt, J. & Stelzer, E.H.K. Optical sectioning deep inside live embryos by selective plane illumination microscopy. *Science* **305**, 1007-1009 (2004).
177. Culver, J.P., Ntziachristos, V., Holboke, M.J. & Yodh, A.G. Optimization of optode arrangements for diffuse optical tomography: A singular-value analysis. *Optics Letters* **26**, 701-703 (2001).
178. Hansen, P.C. & O'Leary, D.P. The use of the L-curve in the regularization of discrete ill-posed problems. *SIAM Journal on Scientific Computing* **14**, 1487-1503 (1993).
179. Ouakli, N., Guevara, E., Dubeau, S., Beaumont, E. & Lesage, F. Laminar optical tomography of the hemodynamic response in the lumbar spinal cord of rats. *Optics Express* **18**, 10068-10077 (2010).
180. Erzurumlu, R.S. & Gaspar, P. Development and critical period plasticity of the barrel cortex. *Eur J Neurosci* **35**, 1540-53 (2012).
181. Erzurumlu, R.S., Murakami, Y. & Rijli, F.M. Mapping the face in the somatosensory brainstem. *Nat Rev Neurosci* **11**, 252-63.

182. Chen-Bee, C.H., Zhou, Y., Jacobs, N.S., Lim, B. & Frostig, R.D. Whisker array functional representation in rat barrel cortex: transcendence of one-to-one topography and its underlying mechanism. *Front Neural Circuits* **6**, 93 (2012).
183. Lustig, B.R., Friedman, R.M., Winberry, J.E., Ebner, F.F. & Roe, A.W. Voltage-sensitive dye imaging reveals shifting spatiotemporal spread of whisker-induced activity in rat barrel cortex. *J Neurophysiol* **109**, 2382-92 (2013).
184. Tsytsarev, V., Pope, D., Pumbo, E., Yablonskii, A. & Hofmann, M. Study of the cortical representation of whisker directional deflection using voltage-sensitive dye optical imaging. *Neuroimage* **53**, 233-238 (2010).
185. Grewe, B.F., Langer, D., Kasper, H., Kampa, B.M. & Helmchen, F. High-speed in vivo calcium imaging reveals neuronal network activity with near-millisecond precision. *Nat Methods* **7**, 399-405 (2010).
186. Liao, L.D. et al. Neurovascular coupling: in vivo optical techniques for functional brain imaging. *Biomed Eng Online* **12**, 38 (2013).
187. Mirabella, G., Battiston, S. & Diamond, M.E. Integration of multiple-whisker inputs in rat somatosensory cortex. *Cereb Cortex* **11**, 164-70 (2001).
188. Bjorn, S., Englmeier, K.H., Ntziachristos, V. & Schulz, R. Reconstruction of fluorescence distribution hidden in biological tissue using mesoscopic epifluorescence tomography. *J Biomed Opt* **16**, 046005 (2011).
189. Bjorn, S., Ntziachristos, V. & Schulz, R. Mesoscopic epifluorescence tomography: reconstruction of superficial and deep fluorescence in highly-scattering media. *Opt Express* **18**, 8422-9 (2010).
190. Yuan, S., Li, Q., Jiang, J., Cable, A. & Chen, Y. Three-dimensional coregistered optical coherence tomography and line-scanning fluorescence laminar optical tomography. *Opt Lett* **34**, 1615-7 (2009).
191. Lo, F.S., Akkentli, F., Tsytsarev, V. & Erzurumlu, R.S. Functional significance of cortical NMDA receptors in somatosensory information processing. *J Neurophysiol* **110**, 2627-36 (2013).
192. Wang, L. & Jacques, S.L. Use of a laser beam with an oblique angle of incidence to measure the reduced scattering coefficient of a turbid medium. *Appl Opt* **34**, 2362-6 (1995).
193. Watanabe, H. et al. In vivo layer visualization of rat olfactory bulb by a swept source optical coherence tomography and its confirmation through electrocoagulation and anatomy. *Biomedical Optics Express* **2**, 2279-2287 (2011).
194. Stoney, S.D., Jr., Thompson, W.D. & Asanuma, H. Excitation of pyramidal tract cells by intracortical microstimulation: effective extent of stimulating current. *J Neurophysiol* **31**, 659-69 (1968).
195. Feldmeyer, D. Excitatory neuronal connectivity in the barrel cortex. *Front Neuroanat* **6**, 24 (2012).
196. Ferezou, I., Bolea, S. & Petersen, C.C. Visualizing the cortical representation of whisker touch: voltage-sensitive dye imaging in freely moving mice. *Neuron* **50**, 617-29 (2006).

197. Lippert, M.T., Takagaki, K., Xu, W., Huang, X. & Wu, J.Y. Methods for voltage-sensitive dye imaging of rat cortical activity with high signal-to-noise ratio. *J Neurophysiol* **98**, 502-12 (2007).
198. Reyes-Puerta, V., Sun, J.J., Kim, S., Kilb, W. & Luhmann, H.J. Laminar and Columnar Structure of Sensory-Evoked Multineuronal Spike Sequences in Adult Rat Barrel Cortex In Vivo. *Cereb Cortex* **25**, 2001-21 (2015).
199. Wu, J.Y., Xiaoying, H. & Chuan, Z. Propagating waves of activity in the neocortex: what they are, what they do. *Neuroscientist* **14**, 487-502 (2008).
200. Prechtl, J.C., Cohen, L.B., Pesaran, B., Mitra, P.P. & Kleinfeld, D. Visual stimuli induce waves of electrical activity in turtle cortex. *Proc Natl Acad Sci U S A* **94**, 7621-6 (1997).
201. Karageorgiou, V. & Kaplan, D. Porosity of 3D biomaterial scaffolds and osteogenesis. *Biomaterials* **26**, 5474-91 (2005).
202. Vroom, J.M. et al. Depth penetration and detection of pH gradients in biofilms by two-photon excitation microscopy. *Applied And Environmental Microbiology* **65**, 3502-3511 (1999).
203. Thevenot, P., Nair, A., Dey, J., Yang, J. & Tang, L.P. Method to Analyze Three-Dimensional Cell Distribution and Infiltration in Degradable Scaffolds. *Tissue Engineering Part C-Methods* **14**, 319-331 (2008).
204. Tang, Q. et al. High-dynamic-range fluorescence laminar optical tomography (HDR-FLOT). *Biomedical Optics Express* **8**, 2124-2137 (2017).
205. Kuo, C.-Y. et al. Development of a 3D Printed, Bioengineered Placenta Model to Evaluate the Role of Trophoblast Migration in Preeclampsia. *ACS Biomaterials Science & Engineering* **2**, 1817-1826 (2016).
206. Trachtenberg, J.E. et al. Open‐source three‐dimensional printing of biodegradable polymer scaffolds for tissue engineering. *Journal of Biomedical Materials Research Part A* **102**, 4326-4335 (2014).
207. Yeatts, A.B., Geibel, E.M., Fears, F.F. & Fisher, J.P. Human mesenchymal stem cell position within scaffolds influences cell fate during dynamic culture. *Biotechnology and Bioengineering* **109**, 2381-2391 (2012).
208. Nguyen, B.-N.B., Ko, H., Moriarty, R.A., Etheridge, J.M. & Fisher, J.P. Dynamic Bioreactor Culture of High Volume Engineered Bone Tissue. *Tissue Engineering Part A* **22**, 263-271 (2015).
209. Yeatts, A.B. & Fisher, J.P. Tubular perfusion system for the long-term dynamic culture of human mesenchymal stem cells. *Tissue Eng Part C Methods* **17**, 337-48 (2011).
210. Yeatts, A.B. et al. In vivo bone regeneration using tubular perfusion system bioreactor cultured nanofibrous scaffolds. *Tissue Engineering Part A* **20**, 139-146 (2013).
211. Zaheer, A. et al. In vivo near-infrared fluorescence imaging of osteoblastic activity. *Nat Biotech* **19**, 1148-1154 (2001).
212. Kirfel, G., Rigort, A., Borm, B. & Herzog, V. Cell migration: mechanisms of rear detachment and the formation of migration tracks. *Eur J Cell Biol* **83**, 717-24 (2004).
213. Herzmann, N., Salamon, A., Fiedler, T. & Peters, K. Analysis of migration rate and chemotaxis of human adipose-derived mesenchymal stem cells in

response to LPS and LTA in vitro. *Experimental cell research* **342**, 95-103 (2016).
214. Lee, D.H. et al. Chemotactic migration of human mesenchymal stem cells and MC3T3-E1 osteoblast-like cells induced by COS-7 cell line expressing rhBMP-7. *Tissue engineering* **12**, 1577-1586 (2006).
215. Murphy, C.M., Haugh, M.G. & O'Brien, F.J. The effect of mean pore size on cell attachment, proliferation and migration in collagen–glycosaminoglycan scaffolds for bone tissue engineering. *Biomaterials* **31**, 461-466 (2010).
216. De Cock, L.J. et al. Engineered 3D microporous gelatin scaffolds to study cell migration. *Chemical Communications* **48**, 3512-3514 (2012).
217. Sapozhnikova, V.V. et al. Capabilities of fluorescence spectroscopy using 5-ALA and optical coherence tomography for diagnosis of neoplastic processes in the uterine cervix and vulva. *Laser Physics* **15**, 1664-1673 (2005).
218. Kuranov, R.V. et al. Combined application of optical methods to increase the information content of optical coherent tomography in diagnostics of neoplastic processes. *Quantum Electronics* **32**, 993-998 (2002).
219. Pan, Y.T. et al. Enhancing early bladder cancer detection with fluorescence-guided endoscopic optical coherence tomography. *Optics Letters* **28**, 2485-2487 (2003).
220. Tumlinson, A.R. et al. Endoscope-tip interferometer for ultrahigh resolution frequency domain optical coherence tomography in mouse colon. *Optics Express* **14**, 1878-1887 (2006).
221. Tumlinson, A.R., Hariri, L.P., Utzinger, U. & Barton, J.K. Miniature endoscope for simultaneous optical coherence tomography and laser-induced fluorescence measurement. *Applied Optics* **43**, 113-121 (2004).
222. Hariri, L.P. et al. Endoscopic optical coherence tomography and laser-induced fluorescence spectroscopy in a murine colon cancer model. *Lasers In Surgery And Medicine* **38**, 305-313 (2006).
223. Lam, S. et al. In vivo optical coherence tomography imaging of preinvasive bronchial lesions. *Clinical Cancer Research* **14**, 2006-2011 (2008).
224. Yu, W.M., Sandoval, R.M. & Molitoris, B.A. Rapid determination of renal filtration function using an optical ratiometric imaging approach. *American Journal Of Physiology-Renal Physiology* **292**, F1873-F1880 (2007).
225. Centonze, V.E. & White, J.G. Multiphoton excitation provides optical sections from deeper within scattering specimens than confocal imaging. *Biophysical Journal* **75**, 2015-2024 (1998).
226. Ntziachristos, V., Tung, C.H., Bremer, C. & Weissleder, R. Fluorescence molecular tomography resolves protease activity in vivo. *Nat Med* **8**, 757-60 (2002).
227. Wasan, H.S., Novelli, M., Bee, J. & Bodmer, W.F. Dietary fat influences on polyp phenotype in multiple intestinal neoplasia mice. *Proceedings Of the National Academy Of Sciences Of the United States Of America* **94**, 3308-3313 (1997).
228. Bremer, C. et al. Optical imaging of spontaneous breast tumors using protease sensing 'Smart' optical probes. *Investigative Radiology* **40**, 321-327 (2005).

229. Marten, K. et al. Detection of dysplastic intestinal adenomas using enzyme-sensing molecular beacons in mice. *Gastroenterology* **122**, 406-414 (2002).
230. Ding, Z.Y., Liang, C.P., Tang, Q.G. & Chen, Y. Quantitative single-mode fiber based PS-OCT with single input polarization state using Mueller matrix. *Biomedical Optics Express* **6**, 1828-1843 (2015).
231. Ding, Z. et al. Imaging Spinal Structures With Polarization-Sensitive Optical Coherence Tomography. *IEEE Photonics Journal* **8**, 1-8 (2016).
232. Tsai, M.T. et al. Effective indicators for diagnosis of oral cancer using optical coherence tomography. *Optics Express* **16**, 15847-15862 (2008).
233. Tsai, M.T. et al. Delineation of an oral cancer lesion with swept-source optical coherence tomography. *Journal Of Biomedical Optics* **13** (2008).
234. Goldberg, B.D. et al. Automated algorithm for differentiation of human breast tissue using low coherence interferometry for fine needle aspiration biopsy guidance. *Journal Of Biomedical Optics* **13** (2008).
235. Mujat, M., Ferguson, R.D., Hammer, D.X., Gittins, C. & Iftimia, N. Automated algorithm for breast tissue differentiation in optical coherence tomography. *Journal Of Biomedical Optics* **14** (2009).
236. Levitz, D. et al. Determination of optical scattering properties of highly-scattering media in optical coherence tomography images. *Opt Express* **12**, 249-59 (2004).
237. Cheong, W.F., Prahl, S.A. & Welch, A.J. A Review Of the Optical-Properties Of Biological Tissues. *Ieee Journal Of Quantum Electronics* **26**, 2166-2185 (1990).
238. Pfau, P.R. et al. Criteria for the diagnosis of dysplasia by endoscopic optical coherence tomography. *Gastrointestinal Endoscopy* **58**, 196-202 (2003).
239. Burrell, R.A., McGranahan, N., Bartek, J. & Swanton, C. The causes and consequences of genetic heterogeneity in cancer evolution. *Nature* **501**, 338-45 (2013).
240. Swager, A. et al. Volumetric laser endomicroscopy in Barrett's esophagus: a feasibility study on histological correlation. *Diseases of the Esophagus* (2015).
241. Boas, D.A., Pitris, C. & Ramanujam, N. Handbook of biomedical optics (CRC press, 2011).
242. Wood, M., Vurgun, N., Wallenburg, M. & Vitkin, I. Effects of formalin fixation on tissue optical polarization properties. *Physics in medicine and biology* **56**, N115 (2011).
243. Hsiung, P.-L., Nambiar, P.R. & Fujimoto, J.G. Effect of tissue preservation on imaging using ultrahigh resolution optical coherence tomography. *Journal of biomedical optics* **10**, 064033-064033-9 (2005).
244. Chen, X. et al. Pegylated Arg-Gly-Asp peptide: 64Cu labeling and PET imaging of brain tumor αvβ3-integrin expression. *Journal of Nuclear Medicine* **45**, 1776-1783 (2004).
245. Van Dam, G.M. et al. Intraoperative tumor-specific fluorescence imaging in ovarian cancer by folate receptor-[alpha] targeting: first in-human results. *Nature medicine* **17**, 1315-1319 (2011).

246. Li, M. et al. Affinity peptide for targeted detection of dysplasia in Barrett's esophagus. *Gastroenterology* **139**, 1472-1480 (2010).
247. Xie, T., Mukai, D., Guo, S., Brenner, M. & Chen, Z. Fiber-optic-bundle-based optical coherence tomography. *Optics letters* **30**, 1803-1805 (2005).
248. Süzen, M., Giannoula, A. & Durduran, T. Compressed sensing in diffuse optical tomography. *Optics express* **18**, 23676-23690 (2010).
249. Mitsunaga, M. et al. Cancer cell-selective in vivo near infrared photoimmunotherapy targeting specific membrane molecules. *Nat Med* **17**, 1685-91 (2011).
250. Mitsunaga, M., Nakajima, T., Sano, K., Choyke, P.L. & Kobayashi, H. Near-infrared Theranostic Photoimmunotherapy (PIT): Repeated Exposure of Light Enhances the Effect of Immunoconjugate. *Bioconjugate Chemistry* **23**, 604-609 (2012).
251. Liang, C.-P. et al. Real-time monitoring of hemodynamic changes in tumor vessels during photoimmunotherapy using optical coherence tomography. *Journal of biomedical optics* **19**, 098004-098004 (2014).
252. Luo, Z., Volkow, N.D., Heintz, N., Pan, Y. & Du, C. Acute cocaine induces fast activation of D1 receptor and progressive deactivation of D2 receptor striatal neurons: in vivo optical microprobe [Ca2+]i imaging. *J Neurosci* **31**, 13180-90 (2011).
253. Nakajima, T., Sano, K., Mitsunaga, M., Choyke, P.L. & Kobayashi, H. Real-time monitoring of in vivo acute necrotic cancer cell death induced by near infrared photoimmunotherapy using fluorescence lifetime imaging. *Cancer research* **72**, 4622-4628 (2012).
254. Chia, T.H. & Levene, M.J. Microprisms for In Vivo Multilayer Cortical Imaging. *Journal Of Neurophysiology* **102**, 1310-1314 (2009).
255. Hanaoka, H. et al. Photoimmunotherapy of hepatocellular carcinoma-targeting Glypican-3 combined with nanosized albumin-bound paclitaxel. *Nanomedicine* **10**, 1139-1147 (2015).
256. Nagaya, T. et al. Near infrared photoimmunotherapy with avelumab, an anti-programmed death-ligand 1 (PD-L1) antibody. *Oncotarget* **8**, 8807 (2017).
257. Nagaya, T. et al. Near infrared photoimmunotherapy targeting EGFR positive triple negative breast cancer: optimizing the conjugate-light regimen. *PloS one* **10**, e0136829 (2015).
258. Nagaya, T. et al. Near infrared photoimmunotherapy of B-cell lymphoma. *Molecular Oncology* **10**, 1404-1414 (2016).
259. Mitsunaga, M. et al. Immediate in vivo target-specific cancer cell death after near infrared photoimmunotherapy. *BMC cancer* **12**, 1 (2012).
260. Xu, H.N. & Li, L.Z. Quantitative redox imaging biomarkers for studying tissue metabolic state and its heterogeneity. *Journal of Innovative Optical Health Sciences* **7**, 1430002 (2014).
261. Paukert, M. et al. Norepinephrine controls astroglial responsiveness to local circuit activity. *Neuron* **82**, 1263-70 (2014).
262. Yano, S. et al. Selective methioninase-induced trap of cancer cells in S/G2 phase visualized by FUCCI imaging confers chemosensitivity. *Oncotarget* **5**, 8729 (2014).

263. Yano, S. et al. Cancer cells mimic in vivo spatial-temporal cell-cycle phase distribution and chemosensitivity in 3-dimensional Gelfoam® histoculture but not 2-dimensional culture as visualized with real-time FUCCI imaging. *Cell Cycle* **14**, 808-819 (2015).
264. Yano, S. et al. Tumor-targeting Salmonella typhimurium A1-R decoys quiescent cancer cells to cycle as visualized by FUCCI imaging and become sensitive to chemotherapy. *Cell Cycle* **13**, 3958-3963 (2014).
265. Park, K. (Elsevier, 2017).
266. Mao, T.Y. et al. Long-Range Neuronal Circuits Underlying the Interaction between Sensory and Motor Cortex. *Neuron* **72**, 111-123 (2011).
267. Petrof, I., Viaene, A.N. & Sherman, S.M. Properties of the primary somatosensory cortex projection to the primary motor cortex in the mouse. *Journal Of Neurophysiology* **113**, 2400-2407 (2015).
268. Winkler, A.M., Rice, P.F., Drezek, R.A. & Barton, J.K. Quantitative tool for rapid disease mapping using optical coherence tomography images of azoxymethane-treated mouse colon. *Journal of biomedical optics* **15**, 041512-041512-10 (2010).
269. Jäckle, S. et al. In vivo endoscopic optical coherence tomography of the human gastrointestinal tract-toward optical biopsy. *Endoscopy* **32**, 743-749 (2000).
270. Ford, H.D. & Tatam, R.P. Characterization of optical fiber imaging bundles for swept-source optical coherence tomography. *Applied optics* **50**, 627-640 (2011).
271. Ford, H.D. & Tatam, R.P. Fibre imaging bundles for full-field optical coherence tomography. *Measurement Science and Technology* **18**, 2949 (2007).